Spectroscopy of Electronic States in Organic and Nano-Crystalline Materials Under High Pressure

by

J. Curtis Beimborn II

B.S. Western Carolina University

A thesis submitted to the
Faculty of the Graduate School of the
University of Colorado in partial fulfillment
of the requirements for the degree of
Doctor of Philosophy
Department of Chemistry
2020

Committee Members:
J. Mathias Weber
Niels Damrauer
Gordana Dukovic
Joel Eaves
Robert Parson
Heather Lewandowski

Beimborn II, J. Curtis (Ph.D., Chemistry, Department of Chemistry)

Spectroscopy of Electronic States in Organic and Nano-Crystalline Materials Under High Pressure

Thesis directed by Professor J. Mathias Weber

Abstract

Semiconductor nanocrystals and organic semiconductors have the potential to revolutionize optoelectronic devices. Both classes of materials have been used in photovoltaic and display technologies and are promising candidates to improve both of these sectors. From a physical chemistry point of view, they are also intriguing systems to study in order to gain insight into the fundamental physics of how light interacts with semiconducting materials. Knowledge of how their crystalline structure and electronic properties are coupled is important from both fundamental and application perspectives.

This thesis presents the work I have completed on the pressure-response of both inorganic semiconductor nanocrystals and organic semiconductors using multiple high-pressure generating apparatus. After a description of the experimental procedures, two chapters focus on the pressure-induced photoluminescence (PL) spectral shifts in perovskite nanocrystals. The PL spectra are used to probe changes in the optical band gap of the perovskites as a function of pressure. The differences between the behavior of the perovskites $CsPbBr_3$ and $CsPbI_3$ can be traced to differences in the crystal structure due to the ionic radii of iodide versus bromide. Studies on the size-dependent pressure-response of $CsPbBr_3$ nanocrystals show that the pressure-induced shift of spectral features may depend on the degree of quantum confinement in various sizes of nanocrystals.

The final chapter focuses on an organic semiconductor, rubrene. Rubrene is a material that possesses the ability to convert low energy photons into higher energy photons through a process called triplet-triplet annihilation (TTA) upconversion. Organic upconverting materials generally require a partner molecule which absorbs the lower energy light (sensitizer). The work in this thesis on rubrene shows that rubrene ions trapped in the crystal can act as the sensitizing species, therefore allowing upconversion without an added sensitizer. The TTA process happens through intermolecular coupling of neighboring molecules, so it should be sensitive to the crystalline structure. Our results show that the upconversion PL and intrinsic PL in rubrene are quenched by applied pressure, due to changes in the intermolecular coupling.

For Hannah

Acknowledgements

First and foremost, I want to acknowledge and thank my advisor, Professor J. Mathias Weber. While visiting my family here in Colorado during a spring break in undergrad, roughly two years before coming to graduate school at CU Boulder, Mathias was kind enough to take the time to show me around his labs as well as the rest of JILA. This experience solidified my desire to go to graduate school, and I could not be happier that I was able to complete my PhD in Mathias's group. Mathias is not only a brilliant scientist, but he is also an effective group manager. This is not something to be taken for granted, and I believe our group's productivity and good morale are direct results of Mathias's thoughtful management style. I am excited to continue my friendship and professional relationship with Mathias as I step into my new role as a professional research assistant here at JILA.

I have been very fortunate to work with a great group of people here in the Weber group. I consider everyone who has passed through JILA's doors during my time here not only as colleagues, but friends. Michael Thompson and "Xavier" Shuang Xu were here when I first joined the group and they were very helpful keeping my spirits up during the first few difficult years of graduate school. Wyatt Zagorec-Marks joined the group a few years after I did, and has made these last few years very fun. I really enjoyed working with Wyatt on our publication on rubrene and enjoyed skiing with him on the weekends even more. Our post-doc Leah Dodson and her husband Thinh have also become close friends of my wife and I, and I thank Leah for all of the career advice she has given over the years. I also would like to thank Madison and Rebecca for listening to me talk about my research and offer new ideas for me to think about. Kenny Wilson and Luke Walther were undergraduate researchers working with me on my perovskite projects and helped immensely, and for that, I cannot thank them enough. They are both excellent students and even better people and I cannot wait to see what they will do with their futures. Finally, none of the work done in the Weber group would be possible without our funding sources. My work was specifically funded by the National Science Foundation through the JILA AMO Physics Frontier Center and the Donors of the American Chemical Society Petroleum Research Fund.

Working in JILA is unlike anywhere else, and the credit for that goes to the JILA staff. As the first graduate student working on my project, a lot of it had to be built from the ground up and that would not have been possible without the expertise found in the JILA shops. Over my time here in JILA, nearly all the staff members have helped me in one way or another, but I must thank some of them individually for their support of my work. Dave Alchenberger and Mark Carter in the Keck metrology lab were always able to help me trouble shoot and solve technical problems related to material properties. Dave also trained me on many of the instruments I used to take data for this thesis, so I owe him many thanks. Hans Green, James Urich, Kyle Thatcher, Calvin Schwadron, Todd Asnicar, and Adam Elzey have all invested a lot of time in teaching me new techniques in the instrument shop and each of them were always there to bounce ideas off of while I was designing new instrumentation for my experiments. Finally, data cannot be processed or analyzed without working computers. For that reason, I would like to thank J.R. Raith keeping all the computers in my lab running smoothly and helping me trouble shoot issues when they arouse.

The Dukovic group here at the University of Colorado also deserves acknowledgement for their contributions to my work. Before I had access to any powder XRD instruments to analyze nanocrystal samples, Leah Hall and Pornthip Tongying in the Dukovic group generously took the time to collect that data for me at the National Renewable Energy Laboratory. Other members of the Dukovic group were great conversation partners on all things nanoscience, which helped me grow in my understanding of this field

I would also like to thank two of my undergraduate professors, Scott Huffman and David Evanoff. Their mentorship during those formative years helped me become the scientist I am today.

Next, I must acknowledge my family for always being there for me. I am grateful for my parents, James and Gynine Beimborn, I certainly could not have done this without them. They raised me to persevere through difficult times and instilled in me the interest in science from a young age. I would also like to thank my sister Korina for all the support she has given to me. My grandparents, Nonna, Grandpa, Omi, and Opi have given me much needed moral support throughout my graduate career.

Finally, and most importantly, I would like to thank my wife, Hannah. She has been an unwavering source of support and encouragement. She has been there for me through all the struggles, exhaustion, and late nights collecting data in the lab, while making sure I was keeping myself happy and healthy. She was able to do all of this while getting a Master's degree in Speech and Language Pathology, and later on, raising our daughter Iris as the best mom the world has ever seen. Hannah, I am so blessed to have you as my life-long best friend and partner.

Contents

Tables

Figures

Chapter 1 Introduction

1.1 Motivation and Scope

Almost every aspect of our modern society is influenced in one way or another by electronic devices, which rely on the unique properties of semiconductor materials to function. These unique properties are what allow us to surf the internet on our computers, they produce the bright colors on our cell phone screens, and, very importantly at this point in our history, they can harness the massive amounts of energy that the Earth receives every second from the Sun.

The specific properties of semiconductors that are center stage in this thesis are those governing how semiconductors absorb and emit light. In general, when light with sufficient energy impinges on a semiconductor, it can excite an electron across the band gap of the material, leaving behind a positively charged hole. There are many possible fates for the excited electron and hole, but there are two that are the most useful. First, the electron and hole can be separated and sent through a circuit to do work. This is the case for photovoltaics, and there is a massive amount of work being done to make this process as efficient as possible. Semiconductor materials with unique properties, some of which are discussed in detail in the following chapters, have the potential to improve solar cell efficiency. This work is paramount to slow the warming of our planet due to the release of greenhouse gases into our atmosphere from the burning of fossil fuels. The second fate of the electron and hole we are interested in is when they recombine, reemitting a photon in a process called photoluminescence. Studying the photoluminescence of materials has direct application in light emitting devices such as light emitting diodes. The only difference is that these devices use electric current to bring electrons into the conduction band, rather than exciting the electrons with light.

When the physical dimensions of semiconductor crystal are brought down to the nanometer scale, i.e. in a nanocrystal, the electron-hole pair can begin to experience quantum confinement. This happens when the diameter of the nanocrystal is nearly the same size, or smaller than the Bohr radius of the bound electron-hole pair, called an exciton. When this happens, the nanocrystals can be called "quantum dots" and begin to behave less like their bulk sized counterparts, and more like the hypothetical "particle in a box" taught in every introductory quantum mechanics course.[1] Instead of displaying band-like electronic structure like macroscopic solids, they have discrete energy states. The separation of these energy states is inversely proportional to the square of the quantum dot size. If the quantum dots are photoluminescent, their spectra blue-shift as the size decreases. Quantum dots are interesting to study from a fundamental perspective due to their unique quantum behavior, but also have important applications in the fields discussed above.

Organic semiconductors are class of semiconductor materials made from polymers or crystals where each site is occupied individual molecules. Within organic semiconductors, the acenes are exciting because many of them have the ability to undergo singlet fission and triplet-triplet annihilation upconversion. Singlet fission can create double the charge carriers for every photon absorbed than conventional materials.[2] If the efficiency of this process can be optimized, it could have a profound effect on photovoltaics, increasing the current that can be extracted from photovoltaic devices. Triplet-triplet annhilation upconversion can also improve photovoltaic technology, if sufficiently optimized, by absorbing low energy light that is currently wasted in solar cells and converting it into light with higher energies which the solar cell can make use of.

The unique properties of semiconductors come from the specific building blocks that they are made from, as well as the crystal structure that the material adopts. For instance, $CsPbI_3$ is a semiconductor material while in the perovskite crystal structure, but an insulator in its orthorhombic, non-perovskite phase.[3] This drastic change begs the question of how changes to the crystal structure affect the electronic properties. One can study this by varying the temperature of a material while probing the desired electronic characteristics, but this method adds or removes thermal energy, which may introduce effects unrelated to the crystal structure itself. Another method used is changing chemical constituents of the material, forcing a change to the crystal structure, but it is not immediately clear if any changes observed are due strictly to the modified crystal structure or to the different chemical identity. Application of high pressures in the GPa range is a clean way to modify the crystal structure, without introducing unwanted variables. This allows one to track changes to the electronic properties that are a direct result of changes to interatomic or, in the case of organic materials, intermolecular distances.

The organization of the rest of the thesis is as follows. In Chapter 2, I will describe how experiments were performed and what kind of instrumentation was used. Chapters 3 and 4 deal with the pressure response of perovskites, an exciting semiconducting material with applications in photovoltaics and display technology. Chapter 3 focuses on the photoluminescence pressure response of $CsPbI_3$ and $CsPbBr_3$ nanocrystals. In Chapter 4, the size dependence of the pressure response of $CsPbBr_3$ quantum dots is discussed. Finally, Chapter 5 lays out a mechanism for triplet-triplet annihilation upconversion in rubrene crystals sensitized by rubrene radical cations and anions that are trapped in the crystals and discusses pressure-induced changes in the efficiency of the upconversion process.

1.2 References

(1) Bawendi, M. G.; Steigerwald, M. L.; Brus, L. E. The Quantum Mechanics of Larger Semiconductor Clusters ("Quantum Dots"). *Annu. Rev. Phys. Chem.* **1990**, *41* (1), 477–496.

(2) Smith, M. B.; Michl, J. Singlet Fission. *Chem. Rev.* **2010**, *110* (11), 6891–6936.

(3) Lai, M.; Kong, Q.; Bischak, C. G.; Yu, Y.; Dou, L.; Eaton, S. W.; Ginsberg, N. S.; Yang, P. Structural, Optical, and Electrical Properties of Phase-Controlled Cesium Lead Iodide Nanowires. *Nano Res.* **2017**, *10*, 1107.

Chapter 2 Experimental Methods

2.1 Overview

In this chapter, the experimental procedures for the work done in the following chapters are explained in detail. We used various high-pressure generating techniques (sections 2.2 and 2.3) in order to study how changes to the crystal structure of different materials affect their electronic states. To probe these changes, we used photoluminescence and photoluminescence excitation spectroscopy. The instruments used as well as the preparation steps to characterize our samples are also described (sections 2.4 – 2.6).

2.2 Diamond Anvil Cell

To produce high pressures to study how the electronic properties of materials are coupled to the crystal structure, we use a diamond anvil cell. Our diamond anvil cell (DAC) setup is a gas membrane driven DAC (easyLab Diacell μScopeDAC RT(G), type Ia 16-sided diamond anvils, base diameter 2.5 mm, culet 0.50 mm, numerical aperture = 0.54) (Figure 2.1) which can produce pressures up to tens of GPa. A stainless-steel gasket (type 302 stainless steel, initial thickness 250 μm) is needed between the diamonds to form a sample compartment. Blank high-pressure gaskets must be pre-indented with the diamond anvil cell to a final thickness of 90 - 100 μm before drilling the sample compartment to ensure proper alignment. A mark was made of the gasket to indicate its orientation in the DAC. Pre-indentation was done by placing a blank gasket between the diamonds and closing the DAC. Then the three bolts that hold the DAC together were tightened until the appropriate thickness was reached (Figure 2.1c). To ensure an even indentation, the thickness of the DAC with the gasket installed was checked at locations a, b, and c shown in Figure

2.1c incrementally during the indentation procedure with a micrometer. Once the gaskets were pre-indented, the sample compartment needed to be drilled.

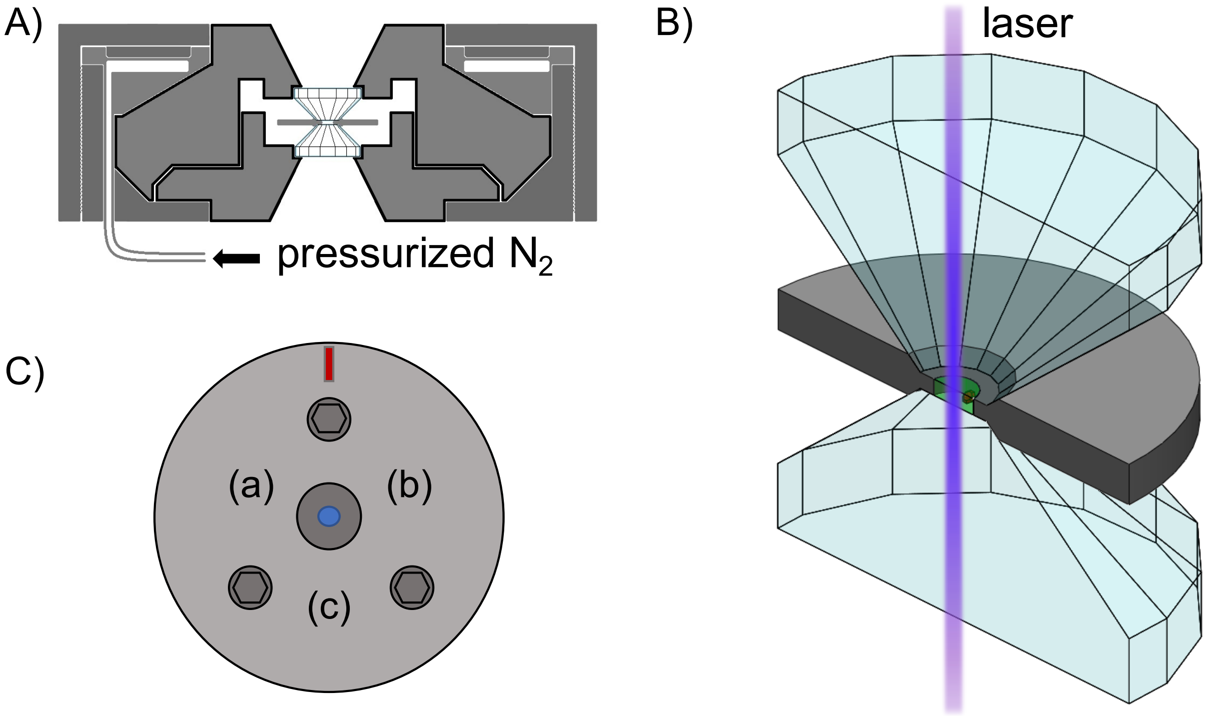

Figure 2.1: (A) cross section of the gas membrane driven diamond anvil cell. Pressurized N_2 is connected to the gas membrane through stainless-steel tubing. As the membrane expands, it applies pressure to the two diamonds. (B) 3D cross sectional rendering of the diamonds and the stainless-steel gasket. The sample compartment is illustrated here filled with a green liquid and a ruby grain for pressure measurement. The laser beam shows the optical access we have to the sample compartment. (C) Top view of the gas membrane driven diamond anvil cell (diamond top surface shown in blue at the center) showing the three bolts used to pre-indent the gaskets and the three positions where the indentation measurements were taken.

To drill the holes in the gaskets, we used a Nd:YAG laser (Innolas Spitlight 300) operating at 1064 nm with 5 ns pulse duration at a 20 Hz repetition rate and 3.5 W average power. The laser beam was routed to a 1 mm aperture and then a 50 mm focal length lens for focusing the beam onto the gasket. A 532 nm solid state diode pumped laser was aligned to be collinear with the 1064 nm pulsed beam to accurately position the gasket before drilling. Gaskets were mounted on a three-axis micrometer translation stage. The holes formed by laser drilling could be made with diameters of 80 μm to 150 μm, by translating the gasket along the propagation axis of the laser beam.

Before each experiment, a small ruby grain was added to the cell along with the sample and droplet of the high-pressure transducing medium. To measure the pressure during an experiment, the ruby R_1 photoluminescence peak was used as a pressure gauge. This has been documented in the literature and works by fitting the R_1 and R_2 lines with Lorentzian profiles (see Figure 2.2) and using equation 2.1 calculate the pressure.[1]

$$P = \frac{A}{B+C}\left(\exp\left\{\frac{B+C}{C}\left[1-\left(\frac{\lambda}{\lambda_0}\right)^{-C}\right]\right\}-1\right) \tag{2.1}$$

Where A, B, and C are empirical constants derived from fitting the experimental data. A is equal to 1820 GPa and B and C are unitless quantities equal to 14, and 7.3 respectively.[1] The ruby R_1 peak at ambient pressure is λ_0 and the peak position at elevated pressure is λ. This calibration scale is reported to have a maximum error of ±1% at the low pressures used here.[1] Error bars on our pressure measurements are ±70 MPa which we have estimated from differences in the R_1 and R_2

peak positions from one ruby crystal grain to another due to unique internal strains that exist in each grain.

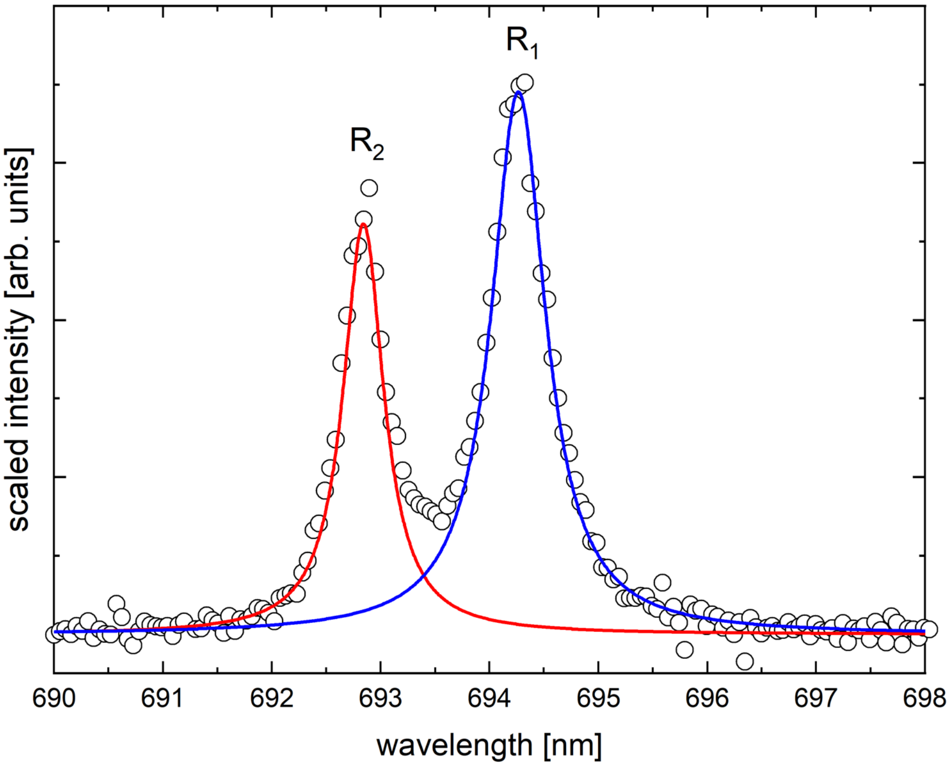

Figure 2.2: Ruby spectrum with Lorentzian fits of the R_1 and R_2 peaks for pressure determination.

During a pressure experiment, the samples were excited using a 406 nm continuous wave (CW) diode laser at intensities of ca. 0.1 W/cm^2 or with a CW 532 nm diode pumped solid state laser with intensities up to 100 W/cm^2. To ensure that the irradiation did not cause significant heating of the samples, the minimum excitation intensity was used to detect photoluminescence. DAC spectra were recorded using a Horiba Scientific XploRA Raman microscope (grating with 600 lines/mm, 0.3 nm resolution) or on a fiber coupled spectrometer setup using an Avantes AvaSpec 2048 fiber optic spectrometer (grating with 300 lines/mm, slit width 50 µm, 2048 pixel CCD detector array, 2.4 nm resolution). In this setup, the excitation light was focused on the DAC using an achromatic doublet pair (ThorLabs MAP1030100-A, f_1 = 30 mm, f_2 = 100 mm) and the

PL was collected on the other side of the DAC in a forward emission geometry with a second achromatic doublet pair (ThorLabs MAP1030100-A, f_1 = 30 mm, f_2 = 100 mm). The collected PL was focused onto a multimode optical fiber (Avantes 400 μm core) using the short focal length of the achromatic doublet pair.

On the Horiba Scientific XploRA Raman microscope, the ruby photoluminescence was measured using an 1800 lines/mm grating (0.1 nm resolution, slit width 50 μm, 1024 pixel CCD array). On the fiber optic spectrometer setup, the ruby spectra were recorded with an Avantes 2048 fiber coupled spectrometer (1800 lines/mm grating, 0.1 nm resolution, 2048 pixel CCD array).

PL peak positions were determined by fitting Lorentzians to the measured spectra. The error associated with this procedure was based on the statistical uncertainty of the fit. After increasing the pressure between spectra, the system was allowed to equilibrate for 20 minutes before taking the next data point. This is a needed step because the stainless-steel gasket deforms plastically rather than elastically, meaning that when pressure is increased on the diamonds, they slowly deform the metal until equilibrium is reached. We empirically determined that after 20 minutes there are negligible changes to the ruby R_1 peak position, and therefore pressure.

2.3 Hydraulic Pressure Generator

A second way to study the pressure response of materials is with a home-built apparatus that is a hydraulic pressure generating setup (Figure 2.3), modified from a design by Tekmen and co-workers. All components purchased from High Pressure Equipment Company (HIP, Erie, Pennsylvania).[2] A hydraulic pressure generator (HIP, 25-5.75-100) capable of producing pressures as high as 700 MPa pressurized a set of stainless steel tubes filled with ethanol as the pressure transmitting fluid. This is not nearly as high as the diamond anvil cell, but the pressure generator allows us to take small steps in pressure, so that we can map out a nearly continuous pressure response of our materials at these pressures. The pressure was determined using a mechanical high-pressure gauge (HIP, 6PG100).

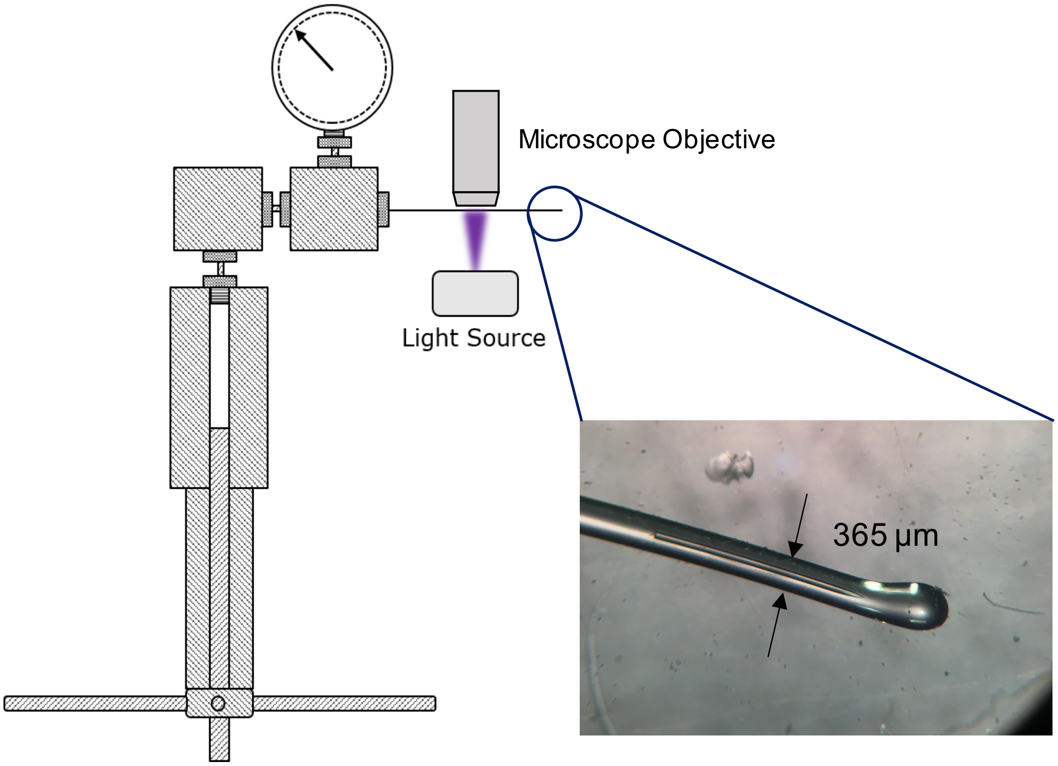

Figure 2.3: A simplified schematic of the hydraulic high-pressure generating apparatus. Inset shows a microscope image of the end of a capillary. The end has been fused closed, and there is a small air gap within the capillary between the sample fluid and the end.

Quartz capillaries with an outer diameter of 375 µm and inner diameter of 50 µm (Molex, TSU050375) were cut into 22 cm long pieces (Figure 2.4). The capillaries come from the manufacturer coated with an opaque polyimide film so in order to have optical access, a 5 cm length of polyimide coating was burned off using an oxygen/propane torch. The position of this window on the capillary corresponded to the section that would be underneath the microscope objective used for sampling PL radiation from the sample when the capillary was coupled to the high-pressure tubing (see description of the microscopy setup below). The end of the capillary furthest from the window was threaded through a modified pressure plug (HIP, 100-7XM4), into which a 400 μm hole had been drilled and epoxied (Armstrong A-12 Epoxy) into place (Figure 2.4). In order to cure the epoxy, the plugs with the capillaries in place were heated at 40° C for 3 hours. The pressure plug could then be coupled to the rest of the apparatus such that the end of the capillary was in contact with the ethanol in the pressure generating apparatus. After an experiment, the pressure plugs were removed from the spent capillaries by heating them to 270° C until the epoxy was burned away. The plugs were then polished in a lathe to ensure good contact to the epoxy for the next experiment.

Figure 2.4: (A) A high-pressure plug as purchased (HIP, 100-7XM4) (top) and the modified high-pressure plug (bottom). (B) The modified high-pressure plug with a capillary epoxied into it. (C) Capillary showing the full length with high-pressure plug and the window where the polyimide coating had been removed.

Samples in hexanes were drawn into the quartz capillaries using capillary action, while samples in paraffin oil had to be forced through the capillary using a syringe with a custom adapter to connect to the high-pressure plug. A small amount of clean paraffin was then drawn into one end of the capillary with the modified syringe adapter to act as a barrier between the sample and the ethanol in the high-pressure generating setup. After loading, the free end of the capillary was fused using an oxygen/propane torch. Fusing the ends of the capillaries must be done by passing the end of the capillary through the hottest part of the flame for the shortest amount of time possible. If it is in the flame too long, the hexanes or paraffin oil boil as the glass is fusing, causing a bubble to form in the capillary wall, significantly compromising its structural integrity.

Spectroscopy using this setup was done by exciting samples using a 532 nm diode pumped solid state laser with the confocal microscope or a 375 nm LED (Figure 2.3). Spectra were collected with the XploRA confocal microscope.

In the hydraulic setup described above, pressurization of glass or quartz capillaries may result in their destruction. If any gas bubbles are present in the pressure-generator or the steel tubing, this can result in explosive release of pressure when the capillary breaks, which represents a hazard to people and equipment. Personal protective equipment must be worn at all times, and polycarbonate shields installed around the apparatus to block any shards in the event of explosive failure of a capillary. To ensure there are no gas pockets in the apparatus, ethanol must be flushed through the whole system every time a new capillary is connected. This will push any air pockets out with the flushed ethanol.

2.4 Upconversion Photoluminescence Spectroscopy

To produce upconversion photoluminescence in rubrene samples for various experiments, we used the tunable near infrared (NIR) output of an optical parametric oscillator (OPO) pumped by a Nd:YAG laser. Two different OPO light sources were used depending on the region of the spectrum scanned. One was a BBO based OPO (GWU premiscan) pumped by the third harmonic of a Nd:YAG laser at 355 nm, the other a KTP based OPO (LaserVision), pumped at by the second harmonic of a Nd:YAG laser at 532 nm. The output pulse duration in either case was 5 ns with a repetition rate of 20 Hz and average power of 50 mW at the rubrene sample. The peak intensity per pulse was 1 MW/cm^2.

In all three experimental setups described in the following Sections, the OPO output beam was passed through a combination of a half-wave plate and polarizers (Figure 2.5-Figure 2.8) to optimize the UCPL signal. A fraction of the beam was picked off with a glass microscope slide

(~8% of the total power) to measure the relative power as a function of OPO frequency. The beam was then directed to the rubrene sample in one of the configurations described below.

2.4.1 Upconversion Photoluminescence Excitation Spectra

In order to measure where rubrene crystals absorb in the NIR, we used a technique similar in practice to photoluminescence excitation (PLE) spectroscopy[3] that we called upconversion photoluminescence excitation (UCPLE) spectroscopy. To measure a UCPLE spectrum, the output beam from the OPO setup described above was directed into a vacuum chamber and onto the rubrene sample. For measurements that were not done at elevated pressures, the rubrene sample was mounted on the outside of a quartz cuvette (labeled "L" in Figure 2.5), which could be filled with liquid nitrogen from the outside of the vacuum chamber for temperature dependent studies. The vacuum chamber prevented condensation forming on the rubrene when it was at low temperatures, and it also eliminated the possibility of photooxidation of rubrene.[4–6] The vacuum chamber was pumped to a base pressure ca. 10^{-2} mbarr with a mechanical pump and inline cold trap. We used a vacuum chamber in these experiments to determine the UCPLE spectra without introducing the possibility of photo-oxidation of the rubrene, and to avoid condensing water on the sample when measuring spectra at 77 K. The frequency of the OPO was tuned while the intensity of the UCPL was measured using a silicon photodiode with an interval of 1 cm^{-1}. The UCPL spectra were recorded by collecting the output voltage of the photodiode using an oscilloscope was fed to a computer using a LabView program and plotted as a function of OPO frequency.

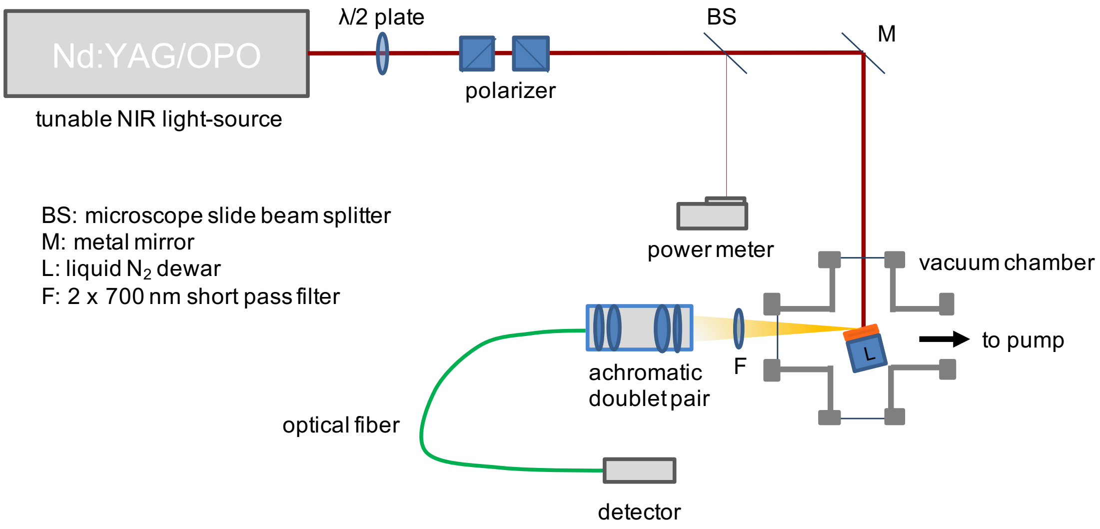

Figure 2.5: Upconversion photoluminescence excitation (UCPLE) spectroscopy setup.

The light incident onto the cuvette was set at an angle of ca. 20° to ensure that no stray reflections of laser light propagated to the detector. To maximize the UCPL signal, we took advantage of the waveguiding nature of the rubrene crystals and collected the UPCL that was emitted from the edges of the crystal, with the detection direction grazing the surface of the crystal mount. If there is self-absorption within the rubrene crystal, this will only introduce a constant offset across the entire UCPLE spectrum, as only the intensity of the UCPL is measured. The UCPL was sent through two 700 nm short pass filters (Thorlabs, FESH0700) to remove any stray NIR laser light. An achromatic doublet pair (ThorLabs MAP1030100-A, f_1 = 30 mm, f_2 = 100 mm) collected the UCPL using the longer focal length and focused it onto an optical fiber (Avantes 400 μm core) which was coupled to a biased silicon photodetector (ThorLabs DET36A2).

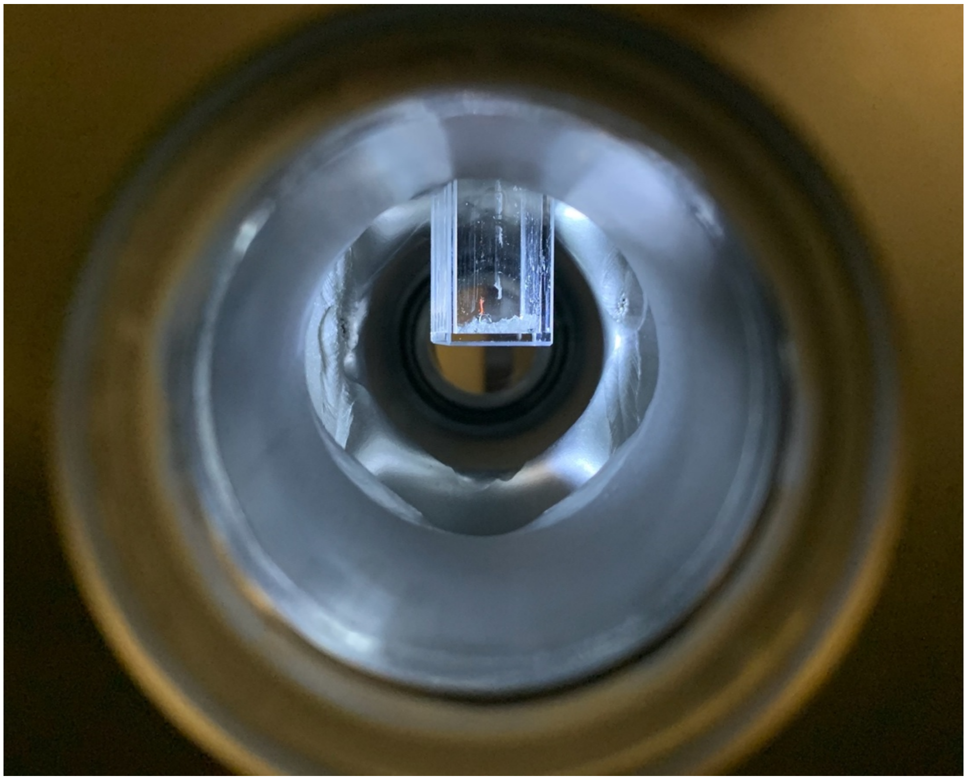

Figure 2.6: Image of the quartz cuvette in the vacuum chamber. The cuvette could be filled from the outside with liquid nitrogen to cool mounted rubrene crystals. The orange vertical line visible on the outside of the cuvette is a rubrene crystal.

2.4.2 Temperature Dependence of UCPL and PL

To measure the temperature dependence of the UCPL and PL, a K-type thermocouple was attached to the inside of the cuvette directly behind where the rubrene crystal was mounted (Figure 2.5). We measured the temperature dependence of the UCPL by exciting the rubrene crystal at each NIR absorption feature and the temperature dependence of the PL by exciting with 532 nm light (doubled ns pusled output of the Nd:YAG). To cool the rubrene crystal down to 77 K, the cuvette was filled with liquid N_2. Once the liquid N_2 evaporated, the temperature and UCPL or PL intensity were recorded every 10 seconds until the crystal had warmed up to room temperature

2.4.3 High-Pressure Upconversion Photoluminescence Excitation Spectra

To measure UCPLE spectra under high-pressure, we directed the OPO output beam into our DAC (Figure 2.7). We loaded the DAC with small rubrene crystal grains made from the physical vapor deposition, as well as rubrene powders purchased from Sigma Aldrich. The pressure transducing medium was paraffin oil. A small ruby crystal was included as well to act as a pressure guage. A half wave plate was used to optimize the UCPL signal. The UCPL was collected in a forward emission geometry due to the limited optical access to the sample inside the DAC. The two 700 nm short pass filters were able to block all laser light from reaching the detector, confirmed by using the setup without any rubrene in the DAC. UCPL signal was collected through an achromatic doublet pair (ThorLabs MAP1030100-A, f_1 = 30 mm, f_2 = 100 mm) and focused onto an optical fiber which was coupled to a biased silicon photodetector (ThorLabs DET36A2). The output of the OPO was scanned over the region of interest and the intensity of the UCPL was measured at each step with the silicon photodector using an oscilloscope which fed data to a computer through a LabView program.

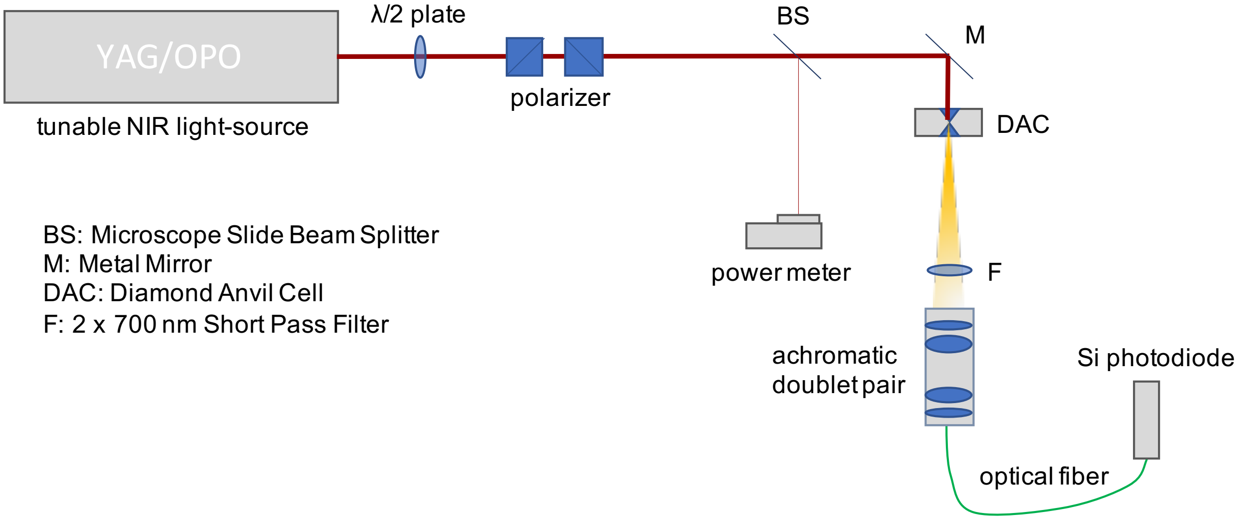

Figure 2.7: Setup for collecting UCPLE spectra under pressure in the DAC.

2.4.4 Pressure-Response of Photoluminescence and Upconversion Photoluminescence

To measure the pressure-response of the PL and the UCPL simultaneously, the experimental setup in Figure 2.7 was modified as follows. First, instead of measuring the intensity of the UCPL on a photodiode, the UCPL and PL light were sent through the optical fiber into a spectrometer (Figure 2.8). Unlike the experiments described above where only the intensity of the UCPL or PL were necessary, this enabled us to monitor the UCPL and PL spectra as a function of pressure. From these spectra, we could extract the integrated intensity as a function of pressure, as well as determine pressure-induced spectral shifts.

In order to measure PL of rubrene under pressure, a 406 nm laser diode was used for excitation. PL measurements were done in the forward emission geometry using a 450 nm long pass filter before the achromatic doublet pair to block any transmitted excitation light from reaching the spectrometer. To accommodate the addition of the diode laser in this geometry, the UCPL excitation and detection were done in a backward emission configuration with the use of a 780 nm high reflector to guide NIR light into the DAC, but to pass the UCPL light. Two 700 nm short pass filters were used before the achromatic doublet pair to ensure no NIR excitation light made it to the spectrometer. Finally, the power of the diode laser and the OPO were taken immediately before recording a spectrum (positioned at the dashed boxes in Figure 2.8) so that the integrated intensity of the spectra could be normalized to laser power.

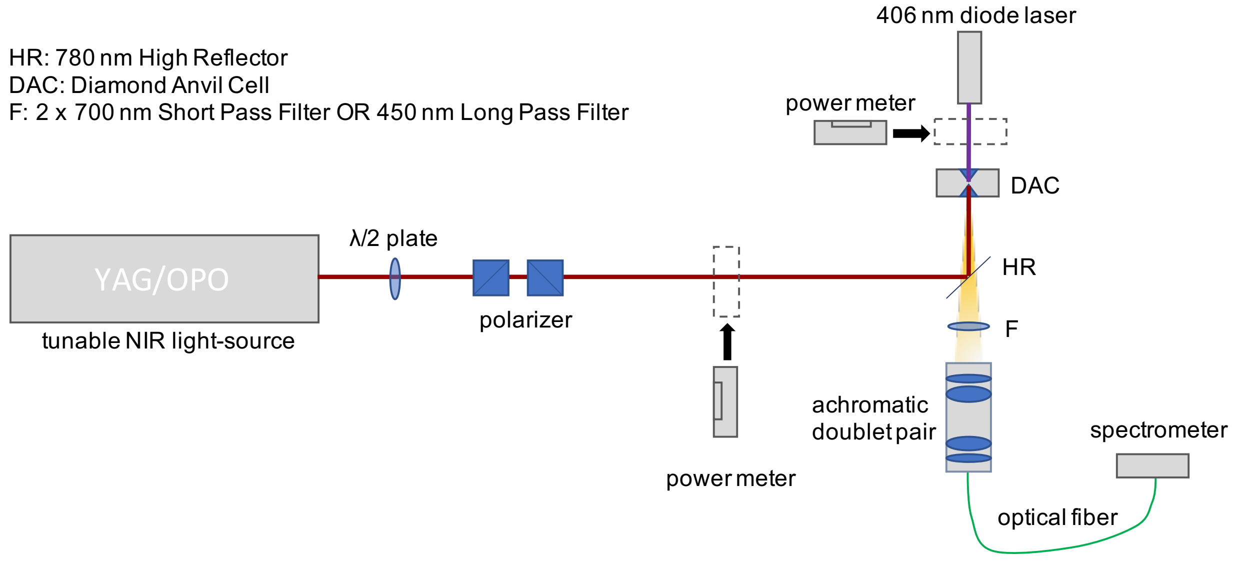

Figure 2.8: Setup for collection photoluminescence (406 nm excitation) and upconversion photoluminescence (NIR excitation) spectra under pressure.

2.5 Transmission Electron Microscopy

Transmission electron microscopy (TEM) images were acquired using a FEI Tecnai ST20 and a FEI Tecnai F20 with an accelerating voltage of 200 kV. TEM samples were prepared by drop casting perovskite NC in a hexanes solutions onto 300 mesh carbon film copper grids (Electron Microscopy Sciences) and allowing the hexanes to evaporate off, leaving only the nanocrystals suspended on the TEM grid. Illuminating the grid with a 375 nm LED reveals how much material was deposited onto the TEM grid. It must be even and not excessive, or the nanocrystals will stack, making acquiring useful images impossible.

2.6 Powder X-Ray Diffraction

Samples for powder x-ray diffraction measurements were prepared by drop casting NC solutions in hexanes onto a silicon low background holder (Bruker Si low background sample holder). Enough sample was deposited with a thin film of NC material was visible with the naked eye on the silicon. If there was excess 1-octadecene or other oily substance in the NC solution, a droplet of that liquid will form rather than a film. XRD can be done on this droplet, but the signal to noise is much worse than for the films. Diffraction patterns were measured with a Bruker D8 Advance using Cu Kα radiation (λ = 0.1540562 nm) with 4º soller slit pair and a 0.6º divergence slit. For NC samples, collection times were ~4,000 seconds to acquire good signal to noise ratios. The powder XRD pattern in section 3.3.1.1 was taken by Leah M. G. Hall on a Rigaku Dmax diffractometer using a Cu Kα radiation source (λ = 0.1540562 nm) with 0.02° 2θ.

2.7 References

(1) Holzapfel, W. B. Refinement of the Ruby Luminescence Pressure Scale. *J. Appl. Phys.* **2003**, *93*, 1813.

(2) Tekmen, M.; Müller, J. D. High-Pressure Cell for Fluorescence Fluctuation Spectroscopy. *Rev. Sci. Instrum.* **2004**, *75*, 5143.

(3) Norris, D. J.; Bawendi, M. G. Measurement and Assignment of the Size-Dependent Optical Spectrum in CdSe Quantum Dots. *Phys. Rev. B Condens. Matter Mater. Phys.* **1996**, *53*, 16338.

(4) Mitrofanov, O.; Kloc, C.; Siegrist, T.; Lang, D. V.; So, W. Y.; Ramirez, A. P. Role of Synthesis for Oxygen Defect Incorporation in Crystalline Rubrene. *Appl. Phys. Lett.* **2007**, *91* (21).

(5) Chen, Y.; Lee, B.; Fu, D.; Podzorov, V. The Origin of a 650 Nm Photoluminescence Band in Rubrene. *Adv. Mater.* **2011**, *23* (45), 5370–5375.

(6) Ly, J. T.; Lopez, S. A.; Lin, J. B.; Kim, J. J.; Lee, H.; Burnett, E. K.; Zhang, L.; Aspuru-Guzik, A.; Houk, K. N.; Briseno, A. L. Oxidation of Rubrene, and Implications for Device Stability. *J. Mater. Chem. C* **2018**, *6* (14), 3757–3761.

Chapter 3 Probing the Pressure-Response of Cesium Lead Halide Perovskite Nanocrystals with Photoluminescence Spectroscopy

This chapter has been adapted with permission from:

(a) Beimborn II, J. C.; Hall, L. M. G.; Tongying, P.; Dukovic, G.; Weber, J. M., "Pressure Response of Photoluminescence in Cesium Lead Iodide Perovskite Nanocrystals," *J. Phys. Chem. C*, 2018, 122, 20, 11024-11030. DOI: 10.1021/acs.jpcc.8b03280. Copyright 2018 American Chemical Society.

(b) Beimborn II, J. C.; Walther, L.; Wilson, K.; Weber, J. M., "Size-Dependent Pressure-Response of the Photoluminescence of $CsPbBr_3$ Nanocrystals," *J. Phys. Chem. Lett.,* 2020, 11, 5, 1975-1980. DOI: 10.1021/acs.jpclett.0c00174. Copyright 2020 American Chemical Society.

3.2 Introduction

Inorganic cesium lead halide perovskites have recently reemerged since their discovery over half a century ago,[1] as materials with not only promising applications, but fascinating fundamental properties. Following the pioneering work by Protesescu *et al.* on the synthesis of perovskite nanocrystals,[2] there has been an explosion of interest in the literature. Their composition-tunable, sharp absorption edges and narrow photoluminescence (PL) spectra make them excellent candidates to be used for next generation light emitting diode (LED) and photovoltaics (PV).[2–7] Out of the family of $CsPbX_3$ materials, $CsPbI_3$ nanocrystals, with their band gap at around 1.8 eV, show particular promise for applications in PV devices. For example, a solar cell using a $CsPbI_3$ nanocrystal film as the absorbing material can reach power conversion efficiencies greater than 14%.[8] Due to the easily achievable near unity quantum yield of $CsPbBr_3$ NCs,[9,10] they are being used to improve various optoelectronic devices such as nano-lasers,[11,12] photodetectors,[13,14] and using the generated charge carries for photocatalytic reduction of CO_2.[13,15–17]

Cesium lead halide perovskites belong to the family of ABX_3 perovskites. Here A is the monovalent cation Cs^+, B is the divalent metal cation Pb^{2+}, and X is a halide. The $CsPbX_3$ perovskite crystal structure is composed of a network of corner-sharing PbX_6 octahedra, with the Cs^+ cations occupying the cavities between the octahedra (Figure 3.1). The perovskite crystal structure is only stable for a window of ratios of the A, B, and X ionic radii. The Goldschmidt tolerance factor[18] is the most widely used predictor of perovskite stability, however, newer tolerance factors have been developed using more sophisticated computational tools.[19] Small changes in the size of the ionic radius of one ion can significantly affect the properties of the perovskite material.

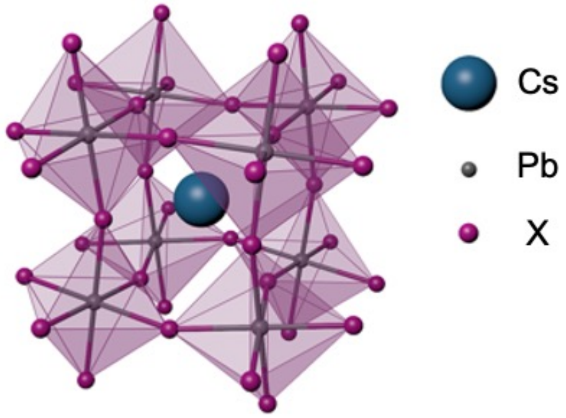

Figure 3.1: The γ-phase perovskite crystal structure, where X is either bromide or iodide anions. The γ-phase crystal structure differs from the α-phase by having Pb-X-Pb angles less than 180°.

$CsPbX_3$ halides are much softer than conventional semiconducting materials. $CsPbBr_3$ nanocrystals have a bulk modulus, a measure of the structural response of a material to pressure, of 16.9 GPa[20] and while the bulk modulus of $CsPbI_3$ has not been experimentally determined yet, calculations estimate it between 16 GPa and 19 GPa.[21] These bulk moduli values place $CsPbX_3$ perovskites between soft, molecular crystals, such as tetracene (ca. 9 GPa[22]), and harder semiconductor crystals such as CdSe (ca. 53 GPa).[23] Given the relatively soft nature of metal halide perovskites compared to other inorganic materials, it is of interest to explore how high pressure will affect the crystal structure, and to measure how these changes affect the optical gap of these materials. High pressure is a convenient way to modify the structure of a condensed phase sample without increasing thermal energy content by adding heat or changing the chemical composition of the material, facilitating exploration of thermodynamics and structure by changing a minimum number of variables.

In this chapter, I will present our results on the structural changes that occur in $CsPbI_3$ and $CsPbBr_3$ perovskite NCs. We used measurements of the optical gap of these materials at elevated pressures to understand how changes in the crystal structure affect the electronic properties. For this study, we focused on all inorganic perovskites rather than their organic/inorganic counter parts to avoid complications the organic A cation could introduce on the pressure dependent effects. The difference in the ionic radius of the halides is discussed as the major factor contributing to the different pressure-responses of the two materials. I will also compare the results of high-pressure experiments done on $CsPbX_3$ NCs prepared by two different synthetic procedures.

3.3 Nanocrystal Synthesis

To study the pressure-response of cesium lead halide perovskite NCs, we used various methods adapted from the existing literature to synthesize $CsPbI_3$ and $CsPbBr_3$ NCs.[10,24,25] Conventional hot-injection under inert atmosphere methods were used, which have precise control over the NC size and size distributions and are the standard for producing high quality samples.

We also employed a scalable tip-sonication synthetic method which can produce large amounts of sample, but with less control over the quality of the final product, to test whether the different synthesis procedures change any of the NC structural or electronic properties we can measure with high-pressure.

3.3.1 $CsPbI_3$ Nanocrystal Synthesis via Hot Injection

The $CsPbI_3$ NC synthesis was adapted from Wang *et al.*[24] A PbI_2 solution was prepared by adding 0.18 mmol of PbI_2 (Aldrich, 99%), 5.0 mL of 1-octadecene (ODE) (Aldrich, technical grade, 90%), 0.5 mL of diisooctylphosphinic acid (DA) (Aldrich, technical grade, ~90%), and 0.5 mL of purified oleylamine (OA) to a round 25 mL bottom flask. The flask was evacuated at 120 °C for one hour with vigorous stirring to remove any dissolved water in the solvents.

In a second round-bottom flask, a Cs-DA solution was prepared by adding 0.30 mmol Cs_2CO_3 (Aldrich, ReagentPlus, 99%), 5.0 mL of ODE, 0.5 mL of DA, and 0.5 mL of purified OA. This mixture was kept at 120 °C under vacuum with vigorous stirring until all the Cs_2CO_3 had dissolved and was then brought to 100 °C under dry nitrogen.

The PbI_2 solution was then brought to 140 °C under dry nitrogen. Next, 0.4 mL of the Cs_2CO_3 solution were injected into the PbI_2 solution with vigorous stirring. Then, due to the extremely fast nature of this reaction, it must be quenched immediately. This was done by transferring to a room temperature water bath as quickly as possible, which was within 5 seconds. The resulting solution was washed by adding excess *tert*-butanol to precipitate the nanocrystals from the reaction mixture. This mixture was centrifuged at 6600 g, and the pellet was resuspended in anhydrous hexanes (Aldrich, ≥ 99%) and stored at -21 °C.

3.3.1.1 $CsPbI_3$ Nanocrystal Characterization

To characterize our synthesized $CsPbI_3$ samples, we used photoluminescence (PL) spectroscopy, UV-vis absorption spectroscopy, transmission electron microscopy, and powder X-ray diffraction. As can be seen in Figure 3.2 the nanocrystals have narrow PL spectra with full width at half-maximum (FWHM) of 30 nm and sharp band edge absorption.

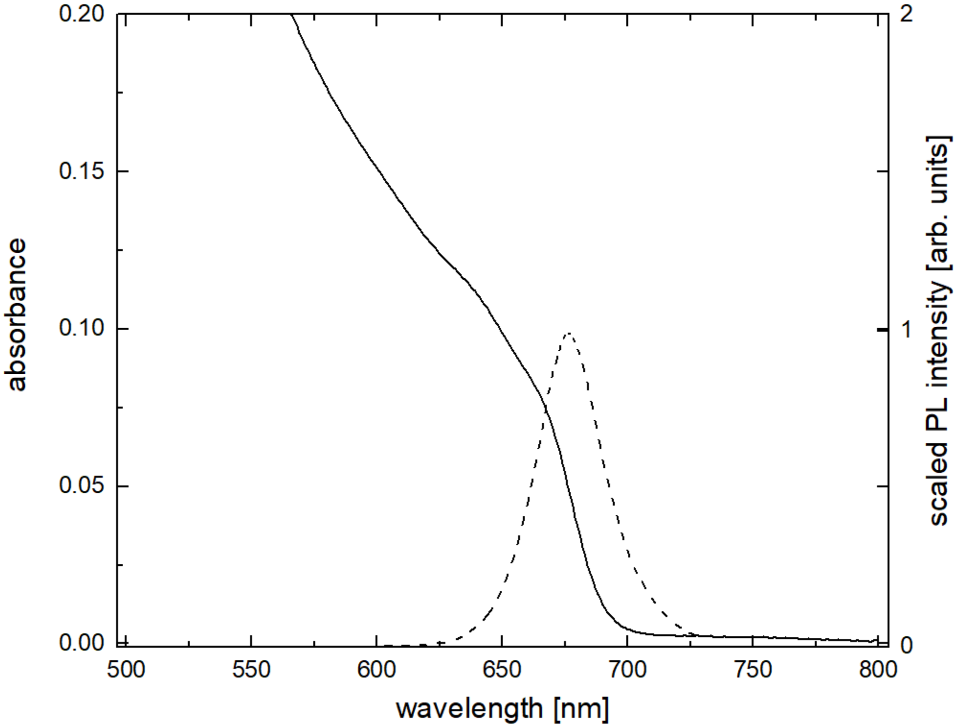

Figure 3.2: Visible absorption (solid) and PL (dashed) spectra of $CsPbI_3$ NCs in hexanes, prepared using hot injection.

The $CsPbI_3$ NC samples have a relatively narrow size distribution of 9.8 ± 2.0 nm (Figure 3.3) compared to what has been published in the literature up to this point, which is generally greater than 10% of the average nanocrystal size,[3,24] although it is significantly broader than for other quantum dot materials, such as CdSe.[26] The reason for the relatively broad size distribution of $CsPbX_3$ NCs lies in the extremely fast kinetics of NC nucleation and growth for this material.[21]

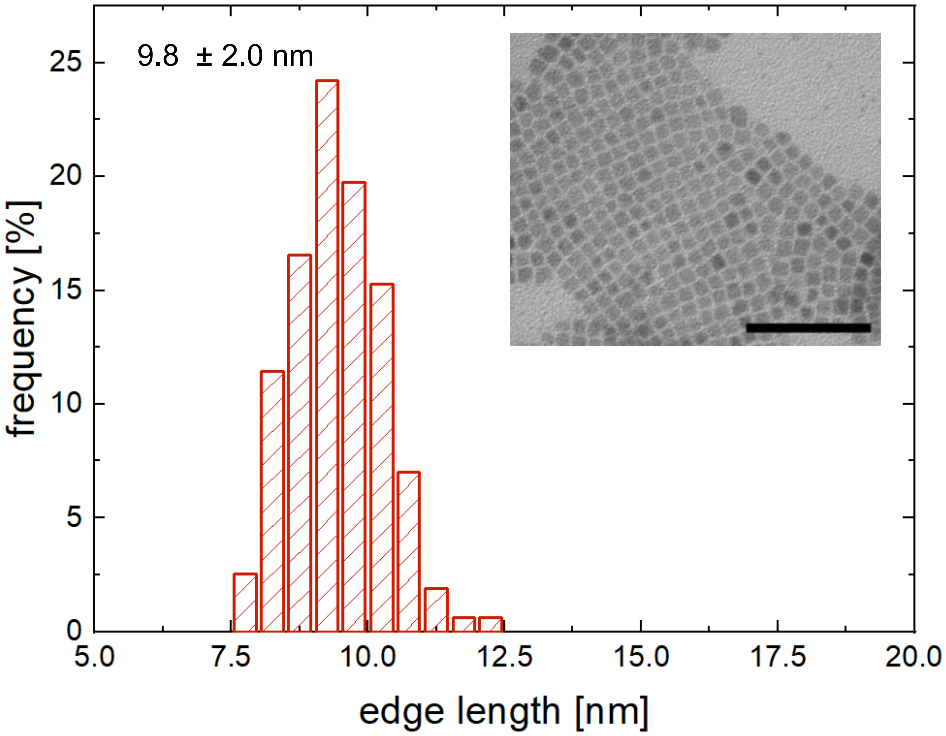

Figure 3.3: $CsPbI_3$ NC sample size distribution histogram (a) and reference TEM image (b). The scale bar represents 100 nm. The NCs were synthesized using hot injection.

The polymorph that $CsPbX_3$ nanocrystals adopt under ambient conditions has been a point of debate in the literature for some time, as x-ray diffraction (XRD) and high-resolution transmission electron microscopy (HRTEM) data have been interpreted as evidence for cubic (α-phase) as well as orthorhombic (γ-phase) perovskite crystal structures (see Section 3.4.1).[2,27–29] Powder XRD data indicate that our $CsPbI_3$ NC samples are in the orthorhombic γ-phase due to the presence of peaks between 16° and 28° 2θ. The incorrect assignment of the cubic α-phase that has been proposed in the literature comes from XRD measurements that did not resolve these peaks.[21,24,27,29,30] By comparing our experimental XRD data with simulated γ-phase and α-phase diffraction patterns (Figure 3.4), it is clear that the data are a closer match to the γ-phase. The unit cell dimensions of our samples are a = 8.6 Å, b = 9.0 Å, and c = 13.1 Å (error bars ± 0.1 Å) which are in good agreement with the reported values by Bertolotti *et al*.[29] Using the Scherrer method to corroborate our TEM size analysis, we found that the crystallite size was 10 ± 2 nm. This value indeed matches the NC size distribution we obtained from TEM image analysis (Figure 3.3), indicating that the NCs are single crystalline. Finally, the lattice spacings in the HRTEM images of the $CsPbI_3$ NCs are consistent with the orthorhombic γ-phase assignment as well (Figure 3.4).

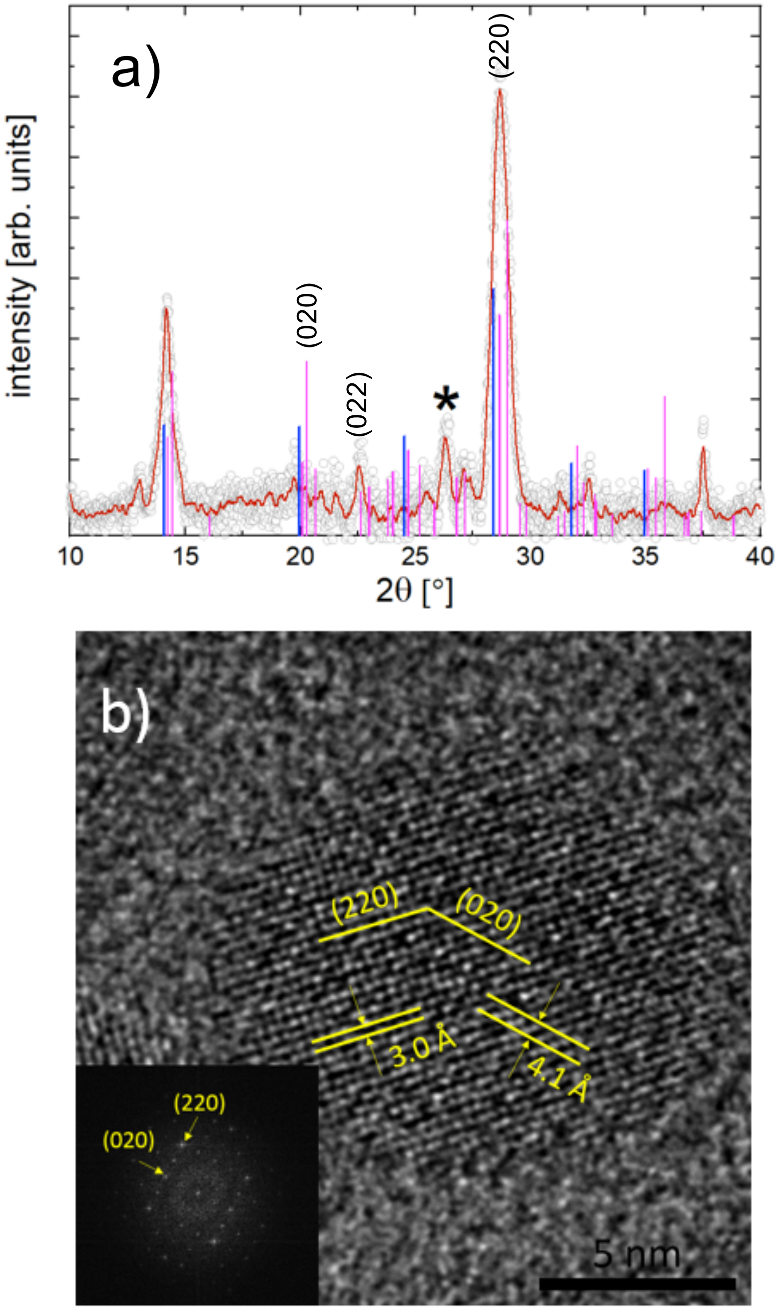

Figure 3.4: (a) XRD pattern of $CsPbI_3$ NCs prepared using hot injection. The light gray points are raw data, the solid red line is a 20-point sliding average. The magenta lines are the expected diffraction angles from the orthorhombic perovskite phase, and the blue lines are the expected diffraction angles for the cubic phase.[21] The peak labeled with a * is from left over PbI_2 from the synthesis procedure. The peaks labeled with miller indices correspond to reflections from the crystal planes indicated in (b). Sample HRTEM image of a $CsPbI_3$ NC and its Fourier transform, together with markers of the (020) and (220) planes (b).

3.3.2 $CsPbBr_3$ Nanocrystal Synthesis

The $CsPbBr_3$ NCs were synthesized with a method similar to the one used for $CsPbI_3$. However, it is possible to control the reaction of $CsPbBr_3$ thermodynamically rather than kinetically by controlling the Pb^{2+}:Br^- ratio in solution, giving narrow size distributions and more reproducible results.[25,31] In a typical synthesis, 75 mg of $PbBr_2$ (Aldrich, $\geq$ 98%), 5 mL of 1-octadecene (ODE) (Aldrich, technical grade 90%), 0.5 mL of oleic acid (OA) (Aldrich, technical grade 90%), and a total of 0.5 mL of OLA and OLA-Br were added to a 25 mL three neck round bottom flask. In a separate 25 mL round bottom flask, we added 162.5 mg of Cs_2CO_3 (Aldrich, 99%), 9 mL of ODE and 1 mL of OA to make a Cs-oleate solution.

Both flasks were stirred and heated to 120° C under vacuum for 1 hour to de-gas the solvents. Next, the flask containing the $PbBr_2$ was filled with nitrogen gas and brought to 160° C. This temperature was chosen to produce nanocrystals with edge sizes on the order of 10 nm to compare with our $CsPbI_3$ samples.[31] The Cs-precursor flask was also filled with nitrogen and allowed to cool to 100° C. Then 0.5 mL of the Cs-oleate solution was swiftly injected into the $PbBr_2$ containing solution. This reaction mixture was then cooled down to room temperature by immersing in a room temperature water bath. However, it was not necessary to perform this step as fast as possible (as in the case of $CsPbI_3$) since the reaction is not kinetically controlled.

To remove as much of the reaction solvents, unreacted precursors, and large aggregates as possible, 10 mL of anhydrous hexanes (Sigma-Aldrich, mixture of isomers anhydrous $\geq$ 99%) were added immediately after the reaction mixture had cooled to room temperature.[32] This colloidally disperses all the $CsPbBr_3$ NCs, but does not disperse or dissolve unreacted precursors or large $CsPbBr_3$ aggregates. This turbid mixture was centrifuged at 6600 g and the supernatant containing the synthesized colloidal NCs was saved. Next, dry nitrogen was blown over the surface of the colloid solution to slowly evaporate off hexanes. Upon sufficient evaporation of hexanes, the largest NCs began to precipitate out of the colloidal solution, which was characterized by a visual change in the solution from transparent to turbid. This occurs because hexanes are a better solvent for $CsPbBr_3$ NCs than ODE, in which the synthesis is performed. This turbid solution was then centrifuged (6600 g), and the NCs were collected from the resulting pellet and resuspended in hexanes. This process narrows the size distribution even further by rejecting smaller nanocrystals.

3.3.2.1 $CsPbBr_3$ Nanocrystal Characterization

As with $CsPbI_3$, we characterized our $CsPbBr_3$ NCs with PL spectroscopy, transmission electron microscopy, and powder X-ray diffraction. The nanocrystals have narrow PL spectra with full width at half-maximum (FWHM) of 15 nm, indicating a narrow size distribution (Figure 3.5).

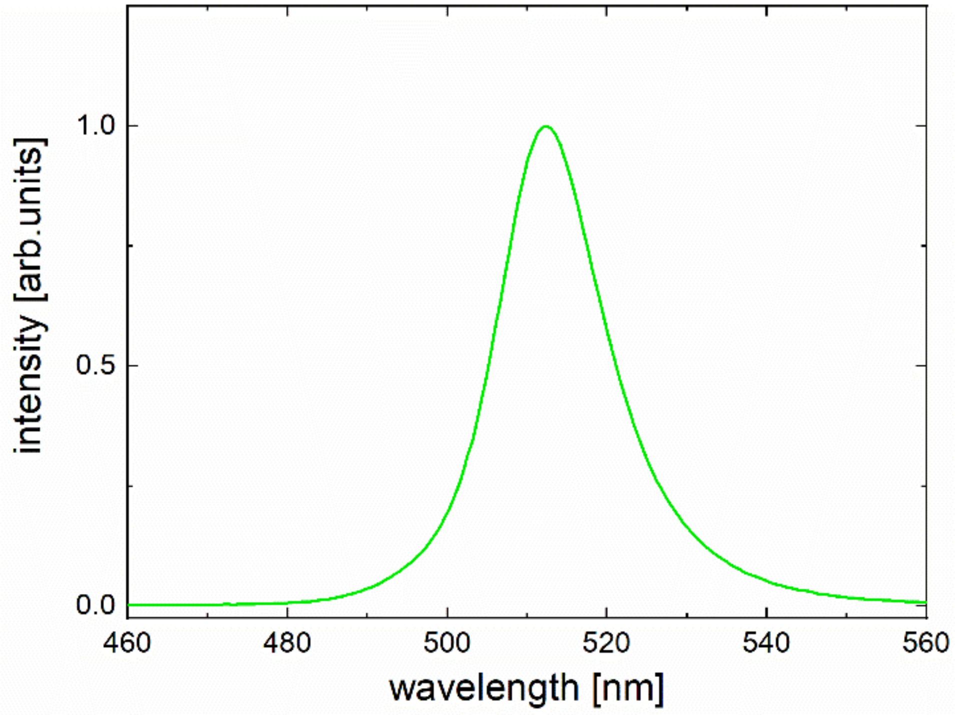

Figure 3.5: PL of $CsPbBr_3$ NCs in hexanes with 10.9 ± 1.2 nm edge length, prepared by hot injection.

We achieved a monodisperse sample with the procedure outlined above with NCs 10.9 ± 1.2 nm (Figure 3.6). The standard deviation in the $CsPbBr_3$ was nearly a factor of two smaller than for the $CsPbI_3$ NCs. However, the growth kinetics of $CsPbBr_3$ are still fast, preventing even higher monodispersity achievable in other semiconductor nanomaterials.

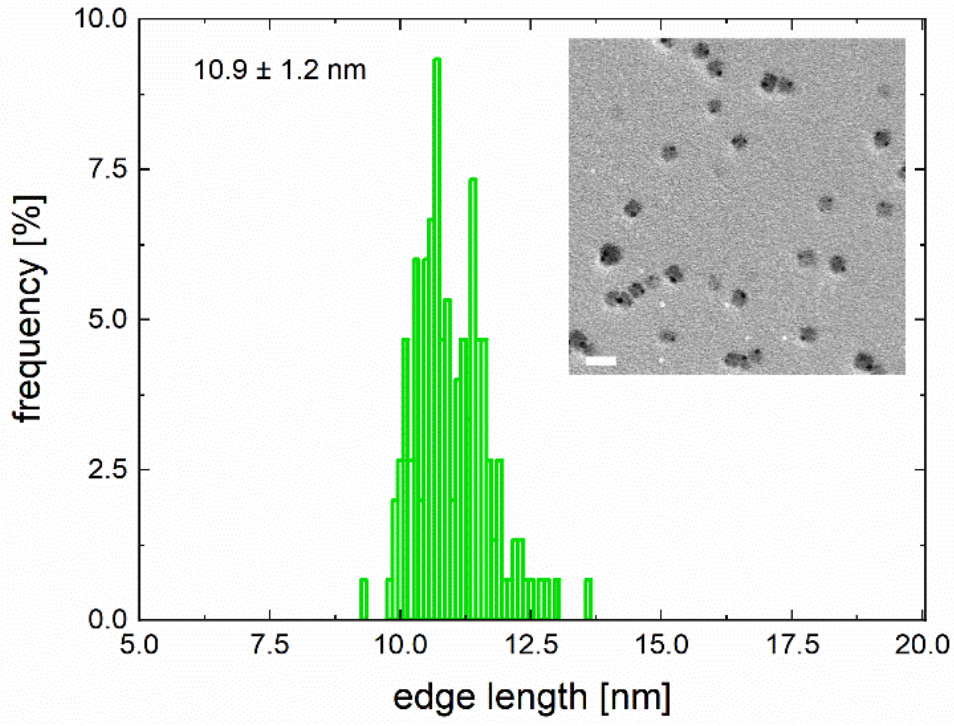

Figure 3.6: Size statistics of the $CsPbBr_3$ NCs prepared using hot injection, with typical TEM image of the NCs (inset). The scale bar is 20 nm.

A similar controversy over the crystal structure of $CsPbBr_3$ under ambient conditions as with $CsPbI_3$ has existed. The $CsPbBr_3$ NCs prepared in the present work were confirmed to be in the orthorhombic perovskite crystal structure using powder XRD (Figure 3.7). We show calculated diffraction angles for cubic and orthorhombic crystal structures, and it is clear that our experimental data matches the predicted pattern for orthorhombic crystal structure.

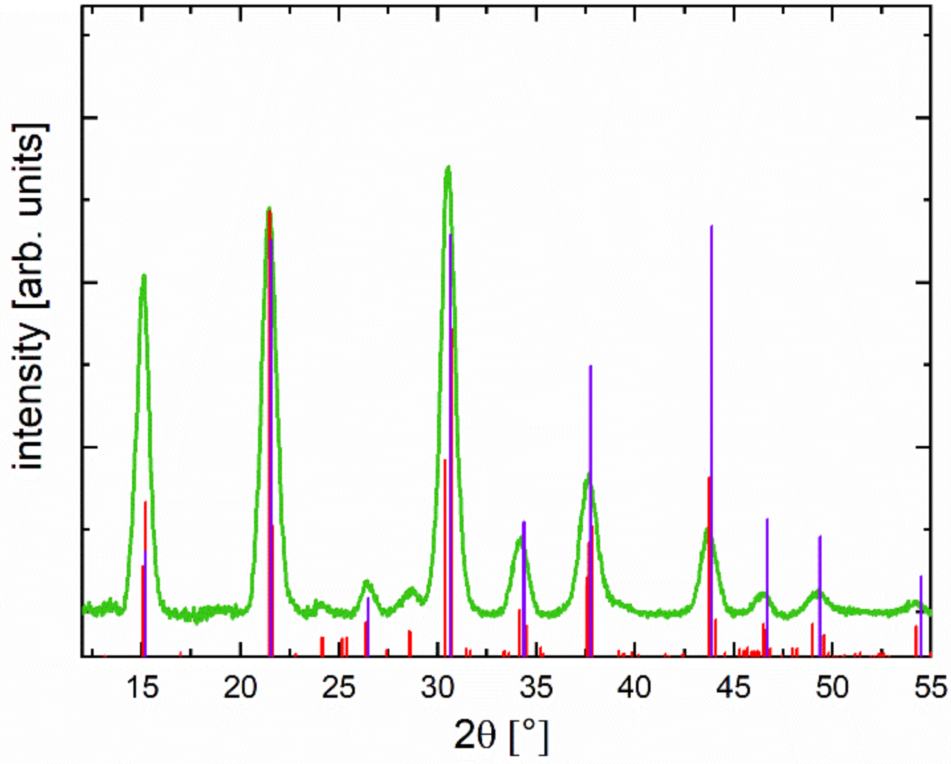

Figure 3.7: Powder XRD pattern of the $CsPbBr_3$ NCs made with hot injection. The red lines are the expected pattern for the orthorhombic perovskite structure while the purple lines are the expected pattern for the cubic perovskite structure.

3.3.3 $CsPbX_3$ Nanocrystal Synthesis via Sonication

Most procedures for synthesizing perovskite NCs require high-temperature injection under an inert atmosphere.[2,33] These methods produce very monodisperse samples with high quantum yields, but are not easily scalable. Tong *et al.* published a scalable procedure for synthesizing monodisperse samples of nanocubes and nanoplatelets of cesium lead halide perovskites ($CsPbX_3$ where X = Cl, Br, or I) in ambient air and without the need for high temperature injection.[28] In a typical synthesis, 0.1 mmol of cesium carbonate along with 0.3 mmol of PbX_2 (X = Br or I) salts were added to 10 mL of 1-octadecene with 0.5 mL each of oleylamine and oleic acid. All reagents were purchased from Sigma Aldrich and used without further purification.

This mixture was subjected to 10 minutes of tip ultrasonication at a power of 30 W. During ultrasonication, the color of the reaction mixture slowly changes from colorless to strongly colored (yellow for X = Br, deep red for X = I), yielding a cloudy suspension that contains both NCs and bulk material. To remove unreacted precursors and bulk material, the suspension was centrifuged at 6600 g for 10 minutes. The supernatant was discarded, and the pellet was re-suspended in hexanes. This solution was centrifuged again at 2000 rpm for 10 minutes to remove bulk material. The clear, colored supernatant containing the NCs was saved, and the pellet was discarded. The clear, colored solution was subsequently centrifuged at higher speeds (>9000 rpm, 20 minutes) to further separate nanocrystal size fractions.

3.3.3.1 Characterization of $CsPbX_3$ Nanocrystals from Sonication

The NCs synthesized with sonication have narrow PL spectra with full width at half-maximum (FWHM) of 15 nm and 35 nm for X = Br and X = I, respectively (Figure 3.8). The PL spectra match the PL from NCs made with the hot injection method, indicating samples of similar quality.

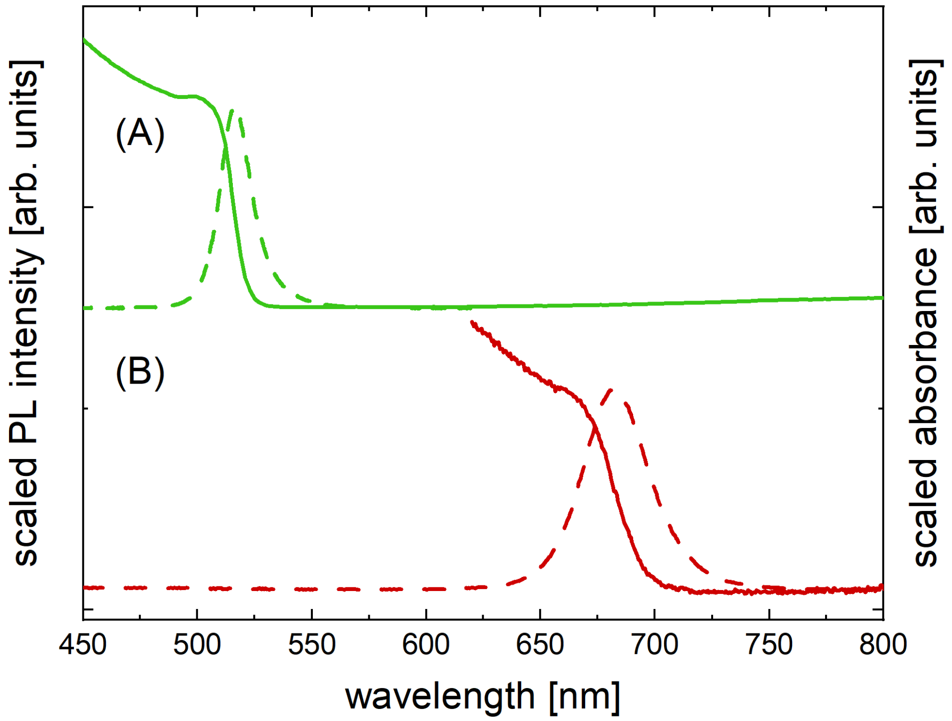

Figure 3.8: Visible absorption (solid) and PL (dashed) of $CsPbBr_3$ (A) and $CsPbI_3$ (B) NCs prepared using sonication. All spectra are scaled independently.

The resulting solutions contained monodisperse (8.6 ± 1.8 nm and 4.7 ± 0.5 nm for X = Br and I, respectively) $CsPbX_3$ NCs (Figure 3.9). The size distributions of the $CsPbBr_3$ is nearly the same as for the hot injection method after size separation centrifugation. The size statistics for the $CsPbI_3$ sample made using sonication are dominated by a highly monodisperse majority fraction of small NCs. Interestingly, the PL of the sonicated $CsPbI_3$ sample is not significantly blue shifted from the $CsPbI_3$ hot-injection sample, despite having a smaller average size. This can be explained by the minority population of large (~10 nm) NCs in the sonicated sample that can be seen in the size histogram and the TEM image. The smallest nanocrystals likely have significantly lower quantum yield than the larger NCs, allowing the larger NCs to dominate the PL response, and red shifting the overall PL peak.[21]

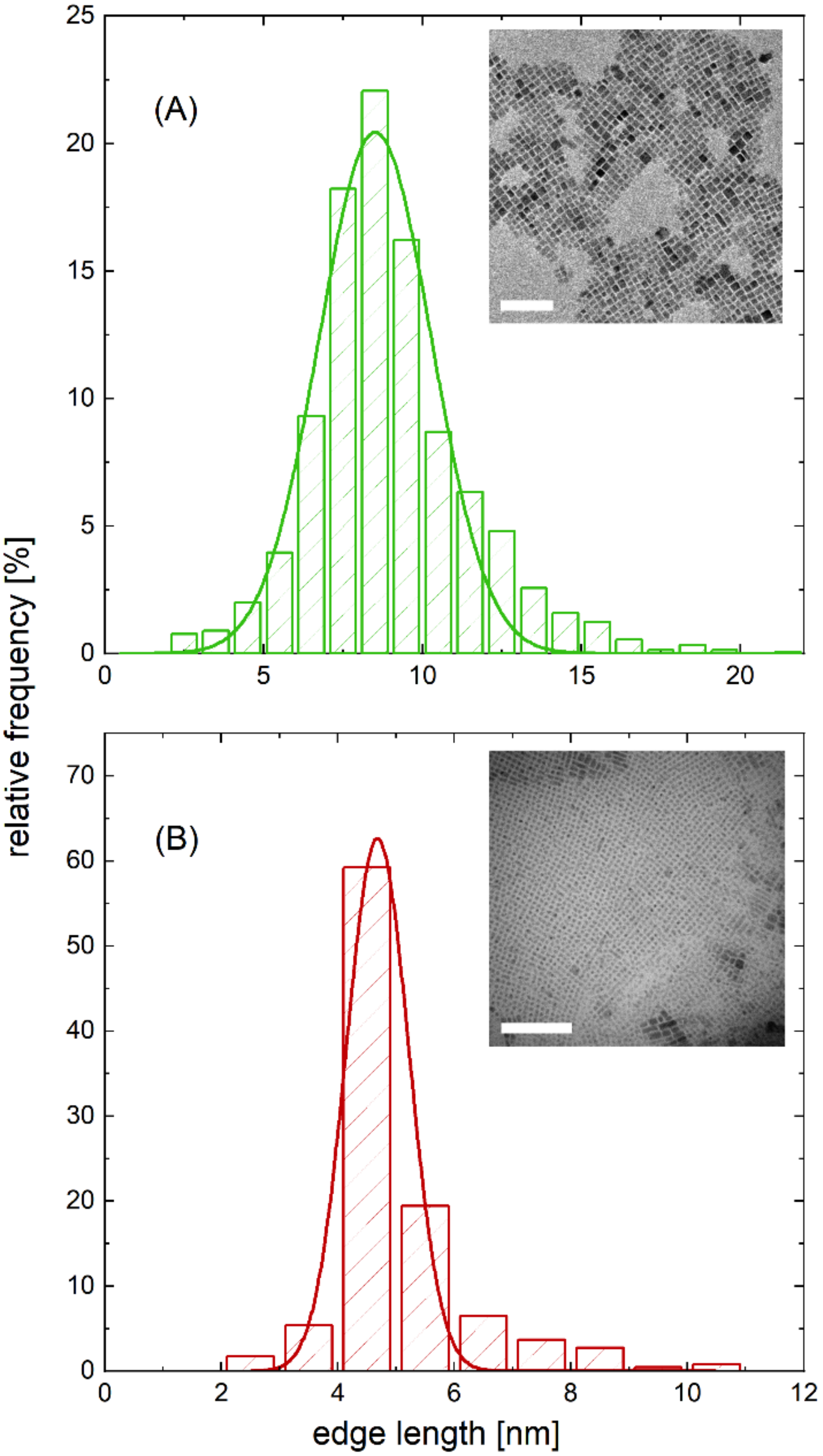

Figure 3.9: Particle size distributions for $CsPbBr_3$ (a) and $CsPbI_3$ (b) prepared using sonication. The scale bars are 100 nm.

High resolution transmission electron microscopy (HRTEM) images were taken using a FEI TALOS F200X CTEM/STEM at 200 keV and used to analyze the NC structure. The lattice spacing of the $CsPbBr_3$ and $CsPbI_3$ NCs match the reported values of the orthorhombic perovskite structure (Figure 3.10).

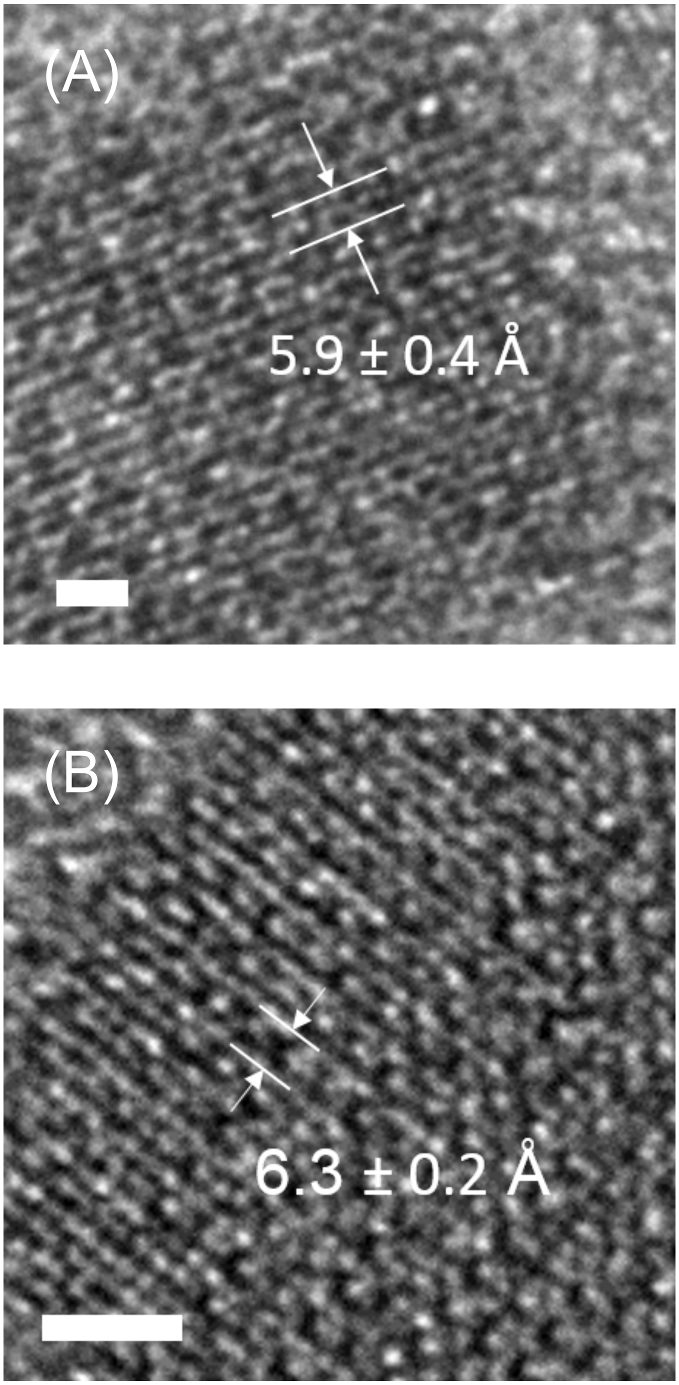

Figure 3.10: HRTEM image of a $CsPbBr_3$ NC prepared using sonication (A) and $CsPbI_3$ NC (B) with lattice spacing. Scale bars are 1 nm.

3.4 Photoluminescence Response of $CsPbX_3$ Nanocrystals Under Pressure

High pressure techniques have been previously applied to bulk and NC samples of $CsPbBr_3$,[20,34–37] and $(CH_3NH_3)PbX_3$ (X = Cl, Br, I)[24,38–43] as well as to bulk samples of $CsPbCl_3$,[35] $CH(NH_2)_2PbI_3$,[44] and the non-perovskite, yellow phase of $CsPbI_3$.[45] It is clear from these previous studies that small differences in the crystal structure of various perovskite materials at ambient pressure can manifest large differences in the pressure response. We use a molecular orbital (MO) picture and a bulk-like band gap picture to interpret our results, as the size of the nanocrystals results only in weak quantum confinement, and therefore thinking in these terms is appropriate. In addition, we compare how the ionic radius of the X anion affects the structural properties and pressure response. Finally, we compare and contrast the high-pressure response of NCs synthesized by two different methods.

3.4.1 Ambient Pressure Phase of $CsPbI_3$ Nanocrystals

Bulk $CsPbI_3$ is metastable in the perovskite crystal structure under ambient conditions, but is very sensitive to degradation due to moisture.[46] Multiple polymorphs exist at ambient pressure at different temperatures.[47] The most stable room temperature phase has a non-perovskite crystal structure (yellow phase or δ-phase).[46] Above room temperature, there are three perovskite crystal structures with different symmetry, denoted α-, β-, and γ-$CsPbI_3$ with cubic, tetragonal, and orthorhombic crystal structures respectively.[29] The γ-$CsPbI_3$ phase is a direct band gap semiconductor with a band gap around 1.8 eV.[3,48]

$CsPbI_3$ NCs are also metastable as perovskite structures at ambient temperature, however, are still very sensitive to moisture. The assignment of crystal structure is complicated because the diffraction peaks differentiating the three perovskite structures are weak in intensity. To make matters worse, nanocrystalline twins can exist in a single NC,[29] which can lead to destructive interference of the diffraction signatures characteristic for the orthorhombic lattice. As a result, several accounts in the literature describe their samples as cubic, while only recently, others clearly identify $CsPbI_3$ NCs as orthorhombic.[2,21,27–29] However, in agreement with our results (Figure 3.4) work by Bertolotti *et al*. and Luther and co-workers has been shown that $CsPbI_3$ NCs are in fact in the orthorhombic *Pnma* perovskite crystal structure under ambient conditions (γ-phase),[21,29] and have been shown to retain this structure for long periods of time in NC and nanowire samples.[24,47,49]

3.4.2 Pressure Response of $CsPbI_3$ Nanocrystals

To prepare a sample for high pressure experiments, the $CsPbI_3$ NCs were dispersed in paraffin, which is hydrostatic up to ca. 3.0 GPa, which is greater than the pressure range studied in the present work.[50] This was accomplished by adding equal amounts of paraffin oil to the solution of NCs in hexanes, followed by stirring under vacuum to remove the hexanes. The resulting solutions of NCs in paraffin were saturated.

We measured the pressure dependent shifts of the PL peak of our samples using hydrostatic pressures up to 2.5 GPa. We observed clear qualitative changes in behavior between different pressure regions. Figure 3.11 shows the PL spectra of $CsPbI_3$ NCs from a typical DAC pressure run. As the pressure is elevated from ambient, the PL emission peak shifts slightly towards longer wavelengths, while it shifts to the blue at higher pressures. At ca. 2.3 GPa, PL emission becomes very weak and finally disappears. Upon return to ambient pressure, the PL emission returns in full, and the peak is observed at the same wavelength as before pressurization.

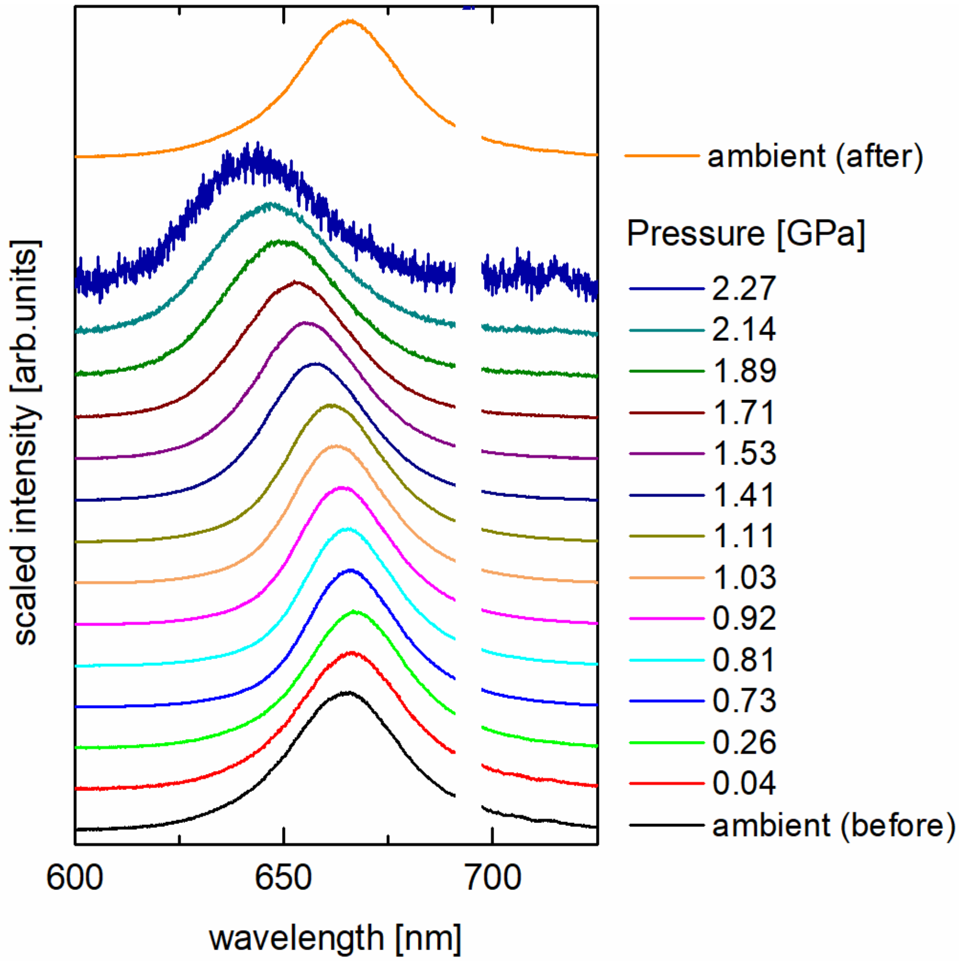

Figure 3.11: PL spectra of $CsPbI_3$ NCs at different pressures (right). All spectra are scaled to the same intensity. The ruby fluorescence peaks around 694 nm were deleted from the spectra for clarity (break in the spectra). The bottom and top traces show the PL spectra at ambient pressure before and after the pressure run.

Upon initial compression, the energy of the PL maximum shifts to lower energies nearly linearly (see Figure 3.12). We can approximately describe this behavior by

$$E_G = E_0 + \alpha p \tag{3.1}$$

where E_0 is the ambient optical gap, and the pressure coefficient, α, describes the slope dE_G/dp. At low pressures, we find a pressure coefficient $\alpha = -14.0 \pm 0.6$ meV/GPa. Further increase of pressure eventually leads to a change in the sign of α, resulting in a blue shift of the PL peak energy, beginning at ca 0.33 GPa, and continuing up to 2.5 GPa (Figure 3.12). The change in the sign of the pressure coefficient α is not accompanied by an observable drop in PL intensity.

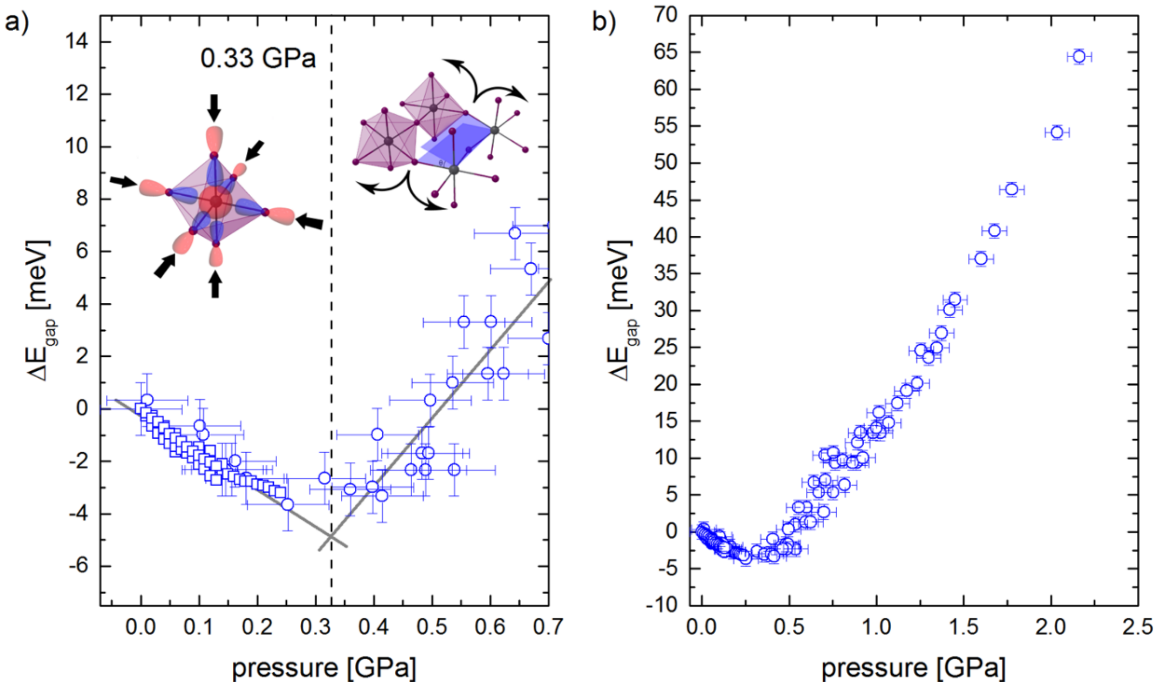

Figure 3.12: Pressure dependence of PL for $CsPbI_3$ nanocrystals. The band gap energy change is plotted as the deviation of the PL peak at a given pressure from the ambient peak position. (a) Pressure range below 0.7 GPa. Data points from the hydraulic pressure generator (open squares) and data taken using the DAC (open circles) from several runs from each setup are shown. The grey lines indicate linear fits of the data in the two regions shown in this panel. The point at which they cross indicates the pressure where the pressure response changes. (b) Overview of the entire pressure range up to 2.5 GPa, after which PL was no longer detected. Data from both the hydraulic pressure generator and the DAC are plotted together, and the data were obtained from several pressure runs. Error bars for the PL peak energy change are ±1 meV.

3.4.3 Pressure Response of $CsPbBr_3$ Nanocrystals

Figure 3.13 shows the pressure dependence of the PL peak energy E_g of $CsPbBr_3$ NCs under hydrostatic pressure. Upon initial compression, the energy of the PL maximum shifts to lower energies nearly linearly, and we can approximately describe this behavior by

$$E_G = E_0 + \alpha p \qquad (3.1$$

where E_0 is the ambient band gap, and the pressure coefficient α describes the slope dE_G/dp. At low pressures, we find a pressure coefficient α = -34.9 ± 0.8 meV/GPa, which is consistent with literature values between -35 meV/GPa for bulk samples and -50 meV/GPa for NC samples at similar pressures.[34,37]

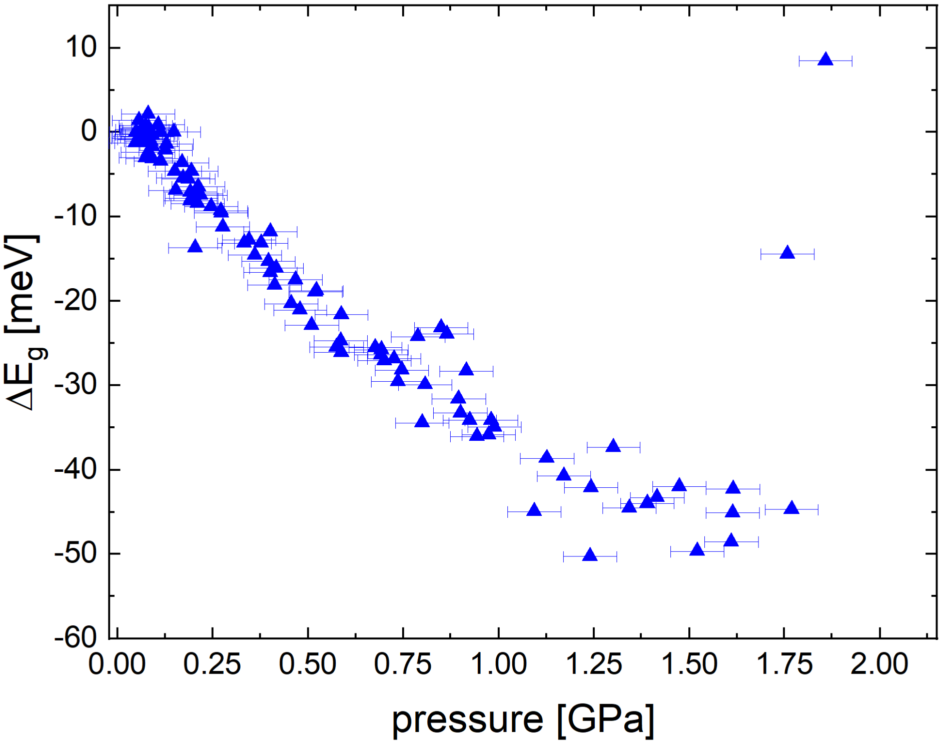

Figure 3.13: Pressure dependence of the PL peak for $CsPbBr_3$ nanocrystals. Different symbols correspond to different pressure runs. Data shown as filled symbols were acquired in the DAC setup, while data shown as open symbols were taken on the hydraulic setup. No PL was observed beyond 2.0 GPa. Error bars for PL energy and for pressure in the hydraulic data sets are smaller than the symbol size. Note that the lowest PL peak energies are slightly different for runs from different synthetic batches, but the phase change pressure remains the same.

Unlike $CsPbI_3$ NCs, where the change in the sign of α occurs near 0.33 GPa, the transition pressure for $CsPbBr_3$ much higher, between 1.2 GPa and 1.5 GPa (Figure 3.13).[34,37]

3.4.4 Pressure-Response of NCs Made from Sonication

NCs made using the scalable sonication method did not show any appreciable difference in the pressure-response of the PL (Figure 3.14). This shows that despite differences in the nanocrystal growth kinetics between the two methods, the resulting nanocrystals have the same structural and electronic properties. The pressure coefficient in the red shifting region of the $CsPbBr_3$ sonicated sample is -35 meV/GPa, which is in great agreement with the pressure coefficient from hot injection. This implies that this material is insensitive to differences in reaction conditions. The sonicated $CsPbI_3$ sample did not match the hot-injection method with α = -7.3 meV/GPa. Given the instability of $CsPbI_3$ NCs when exposed to moisture, this could imply a difference between the two samples coming from the sonication method being done under open air. It could also be due to the fact that the average size of the nanocrystals was smaller than those made in the hot-injection method. However, the PL appears to come mostly from the minority population of large NCs so this cannot account for the difference on its own. Likely, the difference in the slope is a combination of these two variables.

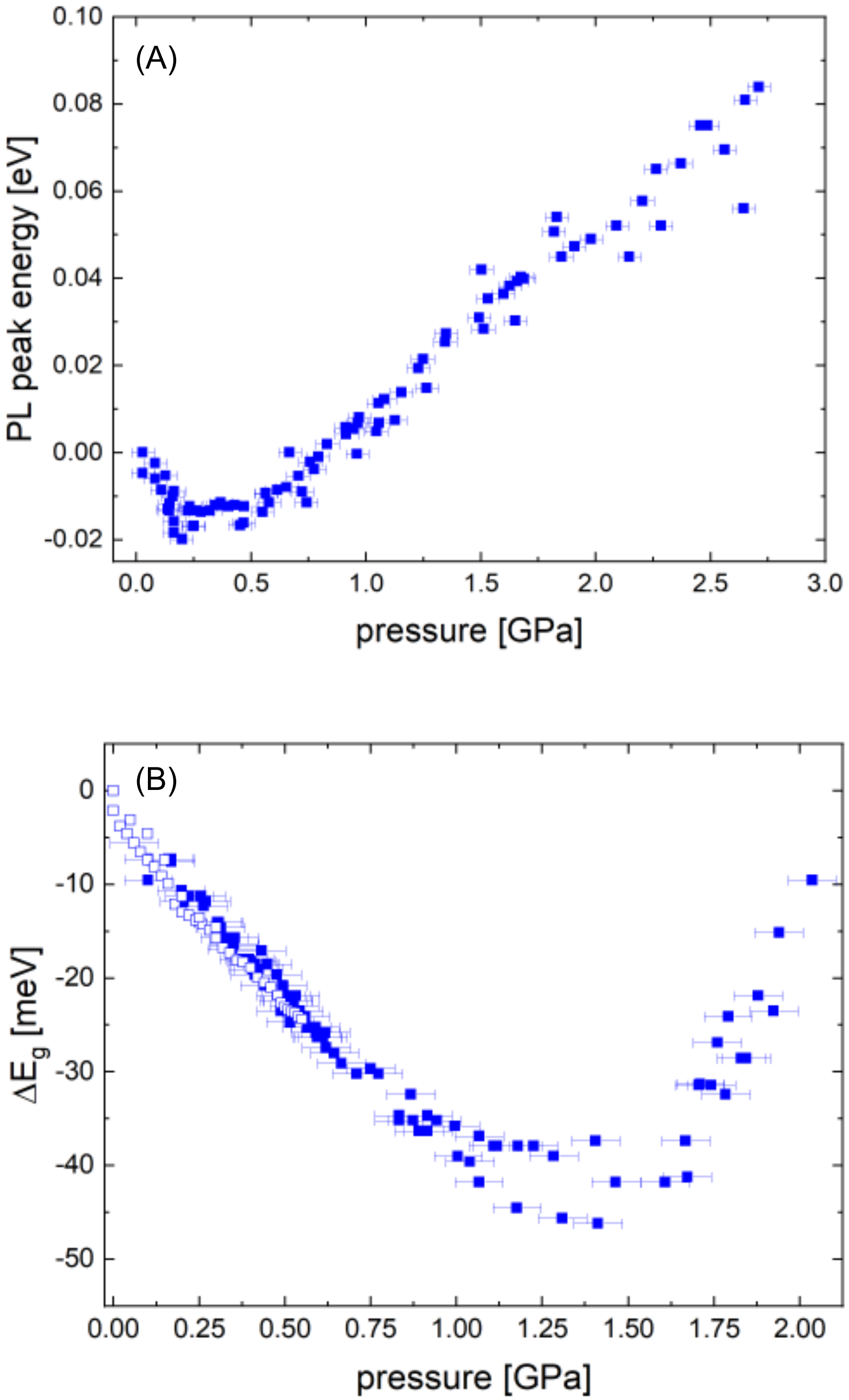

Figure 3.14: Pressure response of $CsPbI_3$ (A) and $CsPbBr_3$ (B) nanocrystals synthesized with by the sonication method. The open square data was taken with the hydraulic high-pressure generator, while the solid squares were taken with the diamond anvil cell.

3.5 Pressure-Response Mechanism

To explain the behavior observed in all four of our samples, we consider the three different ways in which the perovskite crystal structure can respond to application of pressure: by compression of the MX_6 octahedra, by tilting of the octahedra, or by a phase transition into a different crystal structure.[35,51] The behavior of these two materials under pressure was found by Zou and co-workers using *in situ* high pressure powder x-ray diffraction and they found that the perovskites are in the γ-phase up until the pressure where we see a disappearance in PL, at which they become amorphous.[37,52] In the following, we will discuss how the first two different modes of deformation can be expected to affect the optical gap thinking in terms of band theory and MO theory.

The band gap of bulk metal halide perovskites is at the Γ-point for orthorhombic structures.[53] By invoking the symmetry at the Γ-point, the valence band maximum (VBM) in $CsPbX_3$ perovskites must be made from the antibonding interaction of Pb 6s and I 5p (Br 4p) electronic orbitals in $CsPbI_3$ ($CsPbBr_3$) (Figure 3.15),[7,53,54] while the density of states at the conduction band minimum (CBM) is based primarily on the I 5p (Br 4p) orbitals and Pb 6p orbitals (Figure 3.15).[7,53–55] While the small dimensions of the NCs do not allow a rigorous use of the bulk nomenclature for the symmetry points of the Brillouin zone, we expect that the overall character of the corresponding MO picture will be qualitatively similar.

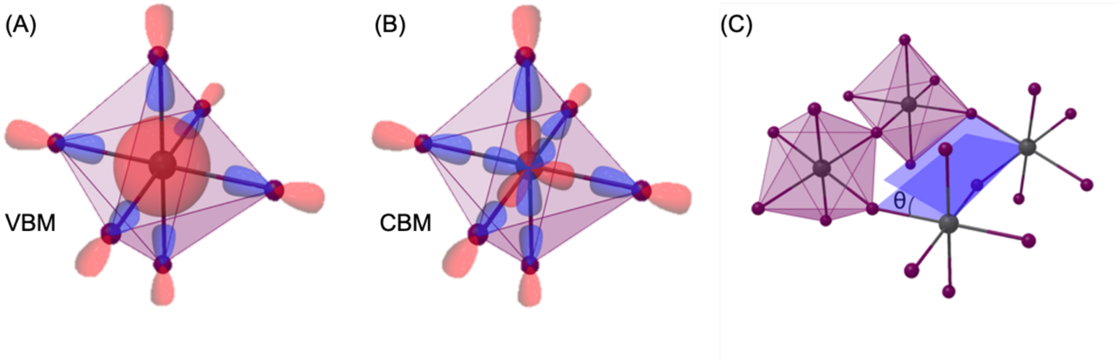

Figure 3.15: (A) Molecular orbitals generating the VBM. (B) Molecular orbitals generating the CBM (C) Tilting of the octahedra increases the dihedral angle θ.

Since the VBM at the Γ-point is dominated by antibonding interactions between the I 5p (Br 4p) and Pb 6s orbitals, compression of the octahedra will result in a destabilization of the VBM, pushing it to higher energies (Figure 3.15). The CBM is largely unaffected by octahedron compression, since the net overlap of the I 5p (Br 4p) and Pb 6p orbitals at the Γ-point gives the CBM a net nonbonding character (Figure 3.15), and small changes in the Pb-X distance will not result in pronounced changes of the CBM energy. Therefore, the mode of deformation characterized by octahedron compression will result in a narrowing of the band gap and a concomitant red shift of the PL peak through the destabilization of the VBM, as observed in other perovskite materials.[24,34,37]

Tilting of the octahedra (Figure 3.15) as a second mode of deformation will have the opposite effect, allowing for a change in the sign of α without a solid-solid phase transition. As shown by calculations by Amat *et al.*,[55] deviation of the Pb-X-Pb angle from 180° changes the mixing of Pb 6p and I 5p (Br 4p) orbitals in the CBM, and diminishes the contributions of Pb orbitals to the CBM. As a result, the impact of spin-orbit coupling on the CBM energy is lessened, and the CBM is destabilized. The net effect of tilting is a band gap increase and concomitant blue shift of the PL. This result is consistent with the band gap change induced by varying the A cation and the accompanying change in tilt angle θ between adjacent octahedra (Figure 3.15).[47,55]

The above discussion explains the high-pressure behavior for both $CsPbBr_3$ and $CsPbI_3$ NCs. The earlier change in the mode of deformation for $CsPbI_3$ can be qualitatively explained with the difference in the ionic radii of Br^- and I^-. Due to the smaller size of the bromide ions, the pressure at which octahedron compression bears a larger energy penalty than octahedron tilting, with the concomitant change in the mode of deformation, happens at a higher pressure than for the same perovskite crystal structure with iodide ions. The initial slopes of the pressure response also reflect the differences in sizes of the Br^- and I^- as the magnitude of the $CsPbI_3$ slope is greater, since the larger I^- is more sensitive to the overlap of the antibonding interactions in the VBM.

3.6 Conclusions

We have studied the structures and pressure response of the PL of $CsPbX_3$ (X = Br, I) NCs. Qualitatively, both materials behave similarly under applied hydrostatic pressure. Both begin by responding to the pressure by narrowing of the band gap until undergoing a change in the mode of deformation that reverses of the sign of dE_g/dp, and then continue to blue shift until a second phase transition causes the PL to disappear. $CsPbI_3$ NCs experience a change in the mode of deformation at the relatively low pressure of 0.3 GPa, followed by another solid-solid phase transition to a dark phase, which was reversible upon pressure release. In contrast, the change in the mode of deformation in $CsPbBr_3$ NCs occurred at a much higher pressure of approximately 1.3 GPa. A second phase transition to a dark phase was also found for $CsPbBr_3$.

We studied the pressure-response of both materials synthesized in two different ways. The hot injection method produces nanocrystals vary rapidly, with the reaction going to completion in milliseconds,[31] while the sonication method takes minutes to go to completion. Despite the difference in growth kinetics, the structural and electronic properties of the nanocrystals were found to be qualitatively the same. This result means that scalable synthetic procedures such as sonication can be used to make large quantities of perovskite NCs for various applications.

3.7 References

(1) MØLLER, C. H. R. K. N. Crystal Structure and Photoconductivity of Cæsium Plumbohalides. *Nature* **1958**, *182* (4647), 1436.

(2) Protesescu, L.; Yakunin, S.; Bodnarchuk, M. I.; Krieg, F.; Caputo, R.; Hendon, C. H.; Yang, R. X.; Walsh, A.; Kovalenko, M. V. Nanocrystals of Cesium Lead Halide Perovskites (CsPbX3, X = Cl, Br, and I): Novel Optoelectronic Materials Showing Bright Emission with Wide Color Gamut. *Nano Lett.* **2015**, *15*, 3692.

(3) Swarnkar, A.; Marshall, A. R.; Sanehira, E. M.; Chernomordik, B. D.; Moore, D. T.; Christians, J. A.; Chakrabarti, T.; Luther, J. M. Quantum Dot-Induced Phase Stabilization of α-CsPbI3 Perovskite for High-Efficiency Photovoltaics. *Science (80-.).* **2016**, *354*, 92.

(4) Huang, H.; Polavarapu, L.; Sichert, J. A.; Susha, A. S.; Urban, A. S.; Rogach, A. L. Colloidal Lead Halide Perovskite Nanocrystals: Synthesis, Optical Properties and Applications. *NPG Asia Mater.* **2016**, *8*, 1.

(5) Swarnkar, A.; Chulliyil, R.; Ravi, V. K.; Irfanullah, M.; Chowdhury, A.; Nag, A. Colloidal CsPbBr3 Perovskite Nanocrystals: Luminescence beyond Traditional Quantum Dots. *Angew. Chem., Int. Ed.* **2015**, *127*, 15644.

(6) Sutherland, B. R.; Sargent, E. H. Perovskite Photonic Sources. *Nat. Photonics* **2016**, *10*, 295.

(7) Manser, J. S.; Christians, J. A.; Kamat, P. V. Intriguing Optoelectronic Properties of Metal Halide Perovskites. *Chem. Rev.* **2016**, *116*, 12956.

(8) Chen, K.; Jin, W.; Zhang, Y.; Yang, T.; Reiss, P.; Zhong, Q.; Bach, U.; Li, Q.; Wang, Y.; Zhang, H.; Bao, Q.; Liu, Y. High Efficiency Mesoscopic Solar Cells Using CsPbI3 Perovskite Quantum Dots Enabled by Chemical Interface Engineering. *J. Am. Chem. Soc.* **2020**, *142* (8), 3775–3783.

(9) Di Stasio, F.; Christodoulou, S.; Huo, N.; Konstantatos, G. Near-Unity Photoluminescence Quantum Yield in CsPbBr3 Nanocrystal Solid-State Films via Postsynthesis Treatment with Lead Bromide. *Chem. Mater.* **2017**, *29* (18), 7663–7667.

(10) Koscher, B. A.; Swabeck, J. K.; Bronstein, N. D.; Alivisatos, A. P. Essentially Trap-Free CsPbBr3 Colloidal Nanocrystals by Postsynthetic Thiocyanate Surface Treatment. *J. Am. Chem. Soc.* **2017**, *139*, 6566.

(11) Pushkarev, A. P.; Korolev, V. I.; Markina, D. I.; Komissarenko, F. E.; Naujokaitis, A.; Drabavičius, A.; Pakštas, V.; Franckevičius, M.; Khubezhov, S. A.; Sannikov, D. A.; Zasedatelev, A. V; Lagoudakis, P. G.; Zakhidov, A. A.; Makarov, S. V. A Few-Minute Synthesis of CsPbBr3 Nanolasers with a High Quality Factor by Spraying at Ambient Conditions. *ACS Appl. Mater. Interfaces* **2019**, *11* (1), 1040–1048.

(12) Oksenberg, E.; Sanders, E.; Popovitz-Biro, R.; Houben, L.; Joselevich, E. Surface-Guided CsPbBr3 Perovskite Nanowires on Flat and Faceted Sapphire with Size-Dependent Photoluminescence and Fast Photoconductive Response. *Nano Lett.* **2018**, *18* (1), 424–433.

(13) Pan, A.; Ma, X.; Huang, S.; Wu, Y.; Jia, M.; Shi, Y.; Liu, Y.; Wangyang, P.; He, L.; Liu, Y. CsPbBr3 Perovskite Nanocrystal Grown on MXene Nanosheets for Enhanced Photoelectric Detection and Photocatalytic CO2 Reduction. *J. Phys. Chem. Lett.* **2019**, *10* (21), 6590–6597.

(14) Gui, P.; Chen, Z.; Li, B.; Yao, F.; Zheng, X.; Lin, Q.; Fang, G. High-Performance

Photodetectors Based on Single All-Inorganic CsPbBr3 Perovskite Microwire. *ACS Photonics* **2018**, *5* (6), 2113–2119.

(15) Chen, Z.; Hu, Y.; Wang, J.; Shen, Q.; Zhang, Y.; Ding, C.; Bai, Y.; Jiang, G.; Li, Z.; Gaponik, N. Boosting Photocatalytic CO2 Reduction on CsPbBr3 Perovskite Nanocrystals by Immobilizing Metal Complexes. *Chem. Mater.* **2020**, *32* (4), 1517–1525.

(16) Xu, Y.-F.; Yang, M.-Z.; Chen, B.-X.; Wang, X.-D.; Chen, H.-Y.; Kuang, D.-B.; Su, C.-Y. A CsPbBr3 Perovskite Quantum Dot/Graphene Oxide Composite for Photocatalytic CO2 Reduction. *J. Am. Chem. Soc.* **2017**, *139* (16), 5660–5663.

(17) Kong, Z.-C.; Liao, J.-F.; Dong, Y.-J.; Xu, Y.-F.; Chen, H.-Y.; Kuang, D.-B.; Su, C.-Y. Core@Shell CsPbBr3@Zeolitic Imidazolate Framework Nanocomposite for Efficient Photocatalytic CO2 Reduction. *ACS Energy Lett.* **2018**, *3* (11), 2656–2662.

(18) Goldschmidt, V. M. Die Gesetze Der Krystallochemie. *Naturwissenschaften* **1926**, *14* (21), 477–485.

(19) Bartel, C. J.; Sutton, C.; Goldsmith, B. R.; Ouyang, R.; Musgrave, C. B.; Ghiringhelli, L. M.; Scheffler, M. New Tolerance Factor to Predict the Stability of Perovskite Oxides and Halides. *Sci. Adv.* **2019**, *5* (2), eaav0693.

(20) Nagaoka, Y.; Hills-Kimball, K.; Tan, R.; Li, R.; Wang, Z.; Chen, O. Nanocube Superlattices of Cesium Lead Bromide Perovskites and Pressure-Induced Phase Transformations at Atomic and Mesoscale Levels. *Adv. Mater.* **2017**, *29*, 1606666.

(21) Zhao, Q.; Hazarika, A.; Schelhas, L. T.; Liu, J.; Gaulding, E. A.; Li, G.; Zhang, M.; Toney, M. F.; Sercel, P. C.; Luther, J. M. Size-Dependent Lattice Structure and Confinement Properties in CsPbI3 Perovskite Nanocrystals: Negative Surface Energy for Stabilization. *ACS Energy Lett.* **2020**, *5*, 238.

(22) Oehzelt, M.; Aichholzer, A.; Resel, R.; Heimel, G.; Venuti, E.; Della Valle, R. G. Crystal Structure of Oligoacenes Under High Pressure. *Phys. Rev. B Condens. Matter Mater. Phys.* **2006**, *74*, 104103.

(23) Strauch, D. *Semiconductors*; 1991.

(24) Wang, C.; Chesman, A. S. R.; Jasieniak, J. J. Stabilizing the Cubic Perovskite Phase of CsPbI3 Nanocrystals by Using an Alkyl Phosphinic Acid. *Chem. Commun.* **2016**, *53*, 232.

(25) Dutta, A.; Dutta, S. K.; Das Adhikari, S.; Pradhan, N. Tuning the Size of CsPbBr3 Nanocrystals: All at One Constant Temperature. *ACS Energy Lett.* **2018**, *3*, 329.

(26) Talapin, D. V; Rogach, A. L.; Kornowski, A.; Haase, M.; Weller, H. Highly Luminescent Monodisperse CdSe and CdSe/ZnS Nanocrystals Synthesized in a Hexadecylamine−Trioctylphosphine Oxide−Trioctylphospine Mixture. *Nano Lett.* **2001**, *1* (4), 207–211.

(27) Cottingham, P.; Brutchey, R. L. On The Crystal Structure of Colloidally Prepared CsPbBr3 Quantum Dots. *Chem. Commun.* **2016**, *52*, 5246.

(28) Tong, Y.; Bladt, E.; Aygüler, M. F.; Manzi, A.; Milowska, K. Z.; Hintermayr, V. A.; Docampo, P.; Bals, S.; Urban, A. S.; Polavarapu, L. Highly Luminescent Cesium Lead Halide Perovskite Nanocrystals with Tunable Composition and Thickness by Ultrasonication. *Angew. Chem., Int. Ed.* **2016**, *55*, 13887.

(29) Bertolotti, F.; Protesescu, L.; Kovalenko, M. V; Yakunin, S.; Cervellino, A.; Billinge, S. J. L.; Terban, M. W.; Pedersen, J. S.; Masciocchi, N.; Guagliardi, A. Coherent Nanotwins and Dynamic Disorder in Cesium Lead Halide Perovskite Nanocrystals. *ACS Nano* **2017**, *11*, 3819.

(30) Udayabhaskararao, T.; Houben, L.; Cohen, H.; Menahem, M.; Pinkas, I.; Avram, L.; Wolf,

T.; Teitelboim, A.; Leskes, M.; Yaffe, O. A Mechanistic Study of Phase Transformation in Perovskite Nanocrystals Driven by Ligand Passivation. *Chem. Mater.* **2017**, *30*, 84.

(31) Dong, Y.; Qiao, T.; Kim, D.; Parobek, D.; Rossi, D.; Son, D. H. Precise Control of Quantum Confinement in Cesium Lead Halide Perovskite Quantum Dots via Thermodynamic Equilibrium. *Nano Lett.* **2018**, *18*, 3716.

(32) Nenon, D. P.; Pressler, K.; Kang, J.; Koscher, B. A.; Olshansky, J. H.; Osowiecki, W. T.; Koc, M. A.; Wang, L.-W.; Alivisatos, A. P. Design Principles for Trap-Free CsPbX3 Nanocrystals: Enumerating and Eliminating Surface Halide Vacancies with Softer Lewis Bases. *J. Am. Chem. Soc.* **2018**, *140*, 17760.

(33) Bekenstein, Y.; Koscher, B. A.; Eaton, S. W.; Yang, P.; Alivisatos, A. P. Highly Luminescent Colloidal Nanoplates of Perovskite Cesium Lead Halide and Their Oriented Assemblies. *J. Am. Chem. Soc.* **2015**, *137*, 16008.

(34) Zhang, L.; Zeng, Q.; Wang, K. Pressure-Induced Structural and Optical Properties of Inorganic Halide Perovskite CsPbBr3. *J. Phys. Chem. Lett.* **2017**, *8*, 3752.

(35) Gesi, K.; Ozawa, K.; Hirotsu, S. Effect of Hydrostatic Pressure on the Structural Phase Transitions in CsPbCl3 and CsPbBr3. *J. Phys. Soc. Jpn.* **1975**, *38*, 463.

(36) Hirotsu, S.; Harada, J.; Iizumi, M.; Gesi, K. Structural Phase Transitions in CsPbBr3. *J. Phys. Soc. Jpn.* **1974**, *37*, 1393.

(37) Xiao, G.; Cao, Y.; Qi, G.; Wang, L.; Liu, C.; Ma, Z.; Yang, X.; Sui, Y.; Zheng, W.; Zou, B. Pressure Effects on Structure and Optical Properties in Cesium Lead Bromide Perovskite Nanocrystals. *J. Am. Chem. Soc.* **2017**, *139*, 10087.

(38) Szafrański, M.; Katrusiak, A. Photovoltaic Hybrid Perovskites Under Pressure. *J. Phys. Chem. Lett.* **2017**, *8*, 2496.

(39) Xiao, J.; Yang, Y.; Xu, X.; Shi, J.; Zhu, L.; Lv, S.; Wu, H.; Luo, Y.; Li, D.; Meng, Q. Pressure-Assisted CH3NH3PbI3 Morphology Reconstruction to Improve the High Performance of Perovskite Solar Cells. *J. Mater. Chem. A* **2015**, *3*, 5289.

(40) Capitani, F.; Marini, C.; Caramazza, S.; Postorino, P.; Garbarino, G.; Hanfland, M.; Pisanu, A.; Quadrelli, P.; Malavasi, L. High-Pressure Behavior of Methylammonium Lead Iodide (MAPbI3) Hybrid Perovskite. *J. Appl. Phys.* **2016**, *119*, 185901.

(41) Matsuishi, K.; Ishihara, T.; Onari, S.; Chang, Y. H.; Park, C. H. Optical Properties and Structural Phase Transitions of Lead-Halide Based Inorganic–Organic 3D and 2D Perovskite Semiconductors Under High Pressure. *Phys. Status Solidi B* **2004**, *241*, 3328.

(42) Yin, T.; Fang, Y.; Chong, W. K.; Ming, K. T.; Jiang, S.; Li, X.; Kuo, J.-L.; Fang, J.; Sum, T. C.; White, T. J. High-Pressure-Induced Comminution and Recrystallization of CH3NH3PbBr3 Nanocrystals as Large Thin Nanoplates. *Adv. Mater.* **2018**, *30*, 1705017.

(43) Jaffe, A.; Lin, Y.; Beavers, C. M.; Voss, J.; Mao, W. L.; Karunadasa, H. I. High-Pressure Single-Crystal Structures of 3D Lead-Halide Hybrid Perovskites and Pressure Effects on Their Electronic and Optical Properties. *ACS Cent. Sci.* **2016**, *2*, 201.

(44) Wang, P.; Guan, J.; Galeschuk, D. T. K.; Yao, Y.; He, C. F.; Jiang, S.; Zhang, S.; Liu, Y.; Jin, M.; Jin, C. Pressure-Induced Polymorphic, Optical, and Electronic Transitions of Formamidinium Lead Iodide Perovskite. *J. Phys. Chem. Lett.* **2017**, *8*, 2119.

(45) Yuan, G.; Qin, S.; Wu, X.; Ding, H.; Lu, A. Pressure-Induced Phase Transformation of CsPbI3 by X-Ray Diffraction and Raman Spectroscopy. *Phase Transitions* **2018**, *91*, 38.

(46) Straus, D. B.; Guo, S.; Cava, R. J. Kinetically Stable Single Crystals of Perovskite-Phase CsPbI3. *J. Am. Chem. Soc.* **2019**, *141* (29), 11435–11439.

(47) Stoumpos, C. C.; Kanatzidis, M. G. The Renaissance of Halide Perovskites and Their

Evolution as Emerging Semiconductors. *Acc. Chem. Res.* **2015**, *48*, 2791.

(48) Kondo, S.; Masaki, A.; Saito, T.; Asada, H. Fundamental Optical Absorption of CsPbI3 and Cs4PbI6. *Solid State Commun.* **2002**, *124*, 211.

(49) Lai, M.; Kong, Q.; Bischak, C. G.; Yu, Y.; Dou, L.; Eaton, S. W.; Ginsberg, N. S.; Yang, P. Structural, Optical, and Electrical Properties of Phase-Controlled Cesium Lead Iodide Nanowires. *Nano Res.* **2017**, *10*, 1107.

(50) Otto, J. W.; Vassiliou, J. K.; Frommeyer, G. Nonhydrostatic Compression of Elastically Anisotropic Polycrystals. I. Hydrostatic Limits of 4:1 Methanol-Ethanol and Paraffin Oil. *Compression Elastically Anisotropic Polycrystals. I. Hydrostatic Limits 41 Methanol-Ethanol Paraffin Oil* **1998**, *57*, 3253.

(51) Angel, R. J.; Zhao, J.; Ross, N. L. General Rules for Predicting Phase Transitions in Perovskites Due to Octahedral Tilting. *Phys. Rev. Lett.* **2005**, *95*, 25503.

(52) Cao, Y.; Qi, G.; Liu, C.; Wang, L.; Ma, Z.; Wang, K.; Du, F.; Xiao, G.; Zou, B. Pressure-Tailored Band Gap Engineering and Structure Evolution of Cubic Cesium Lead Iodide Perovskite Nanocrystals. *J. Phys. Chem. C* **2018**, *122*, 9332.

(53) Borriello, I.; Cantele, G.; Ninno, D. Ab Initio Investigation of Hybrid Organic-Inorganic Perovskites Based on Tin Halides. *Ab initio Investig. Hybrid Org. Perovskites Based Tin* **2008**, *77*, 235214.

(54) Fröhlich, D.; Heidrich, K.; Künzel, H.; Trendel, G.; Treusch, J. Cesium-Trihalogen-Plumbates a New Class of Ionic Semiconductors. *J. Lumin.* **1979**, *18*, 385.

(55) Amat, A.; Mosconi, E.; Ronca, E.; Quarti, C.; Umari, P.; Nazeeruddin, M. K.; Grätzel, M.; De Angelis, F. Cation-Induced Band-Gap Tuning in Organohalide Perovskites: Interplay of Spin–Orbit Coupling and Octahedra Tilting. *Nano Lett.* **2014**, *14*, 3608.

Chapter 4 Size-Dependence of the Pressure-Response of $CsPbBr_3$ Nanocrystals

This chapter has been adapted with permission from:

Beimborn II, J. C.; Walther, L.; Wilson, K.; Weber, J. M., “Size-Dependent Pressure-Response of the Photoluminescence of $CsPbBr_3$ Nanocrystals,” *J. Phys. Chem. Lett.,* **2020**, 11, 5, 1975-1980. DOI: 10.1021/acs.jpclett.0c00174. Copyright 2020 American Chemical Society

4.1 Introduction

Semiconductor nanocrystals (NCs) are a unique class of materials due to their size-dependent properties. The most striking of these is the change in their absorption and photoluminescence (PL) spectra that can be tuned based on their size when the diameter or edge length is less than or equal to the material’s bulk Bohr exciton diameter.[1–7] As the NC size decreases below this characteristic length scale, the electron-hole pair (exciton) experiences strong quantum confinement, which can have a profound effect on the electronic states of the NC. Concomitantly, crystal momentum k, used to describe the electronic band structure of bulk solid materials, is no longer a conserved quantity because momentum is no longer a good quantum number in a confined system, causing the bulk material’s electronic structure to turn from continuous bands into discrete excitonic states which can be crudely modeled with a particle in a three-dimensional box.[8–11] Invoking the particle in a box analogy, as the NC size decreases, the energy gap of the excitonic state is shifted to higher energies, blue shifting the material’s absorption and PL spectra.

The change in the optical and electronic properties of NCs due to quantum confinement are not the only size dependent characteristics, as thermodynamic and structural properties often change as a function of NC size as well. In macroscopic bulk materials, the thermodynamic properties are governed by the vast majority of atoms that are within the bulk volume of the sample, and surface effects can often be ignored. In NC samples, a large fraction of the total atoms are on the surface. This surface-to-volume ratio increases as NC size decreases, altering the thermodynamic and structural properties of NCs. For example, changes in the phase transition of NCs of different sizes can be drastic. In general, the surface energy at constant pressure relaxes in the liquid phase relative to the solid phase. This drives melting points to lower temperatures for smaller NCs, as the contribution of the surface energy to the overall internal energy of the NC grows.[12] Similarly, for many NC systems, it has been shown that the pressure at which the NCs undergo a solid-solid phase transition (at constant temperature) increases as size decreases.[13–16] Due to the high surface to volume ratio of NCs, their ambient crystal structure is generally one that minimizes the surface energy, which promotes the growth of facets with low index surfaces. In most cases, NCs converted from ambient phases to higher-pressure phases have higher index surfaces, and therefore greater surface energy.[17] As a consequence, it usually takes more pressure to force smaller NCs to stabilize the increased surface energy of the high-pressure phase.

The size dependent properties of metal halide perovskite (MHP) NCs have recently attracted attention due to the unique electronic and optical properties of MHPs as well as for their potential applications.[18–24] For example, the high surface defect tolerance of perovskite NCs allows photoluminescence (PL) quantum yields up to 90% without any surface modification,[6] reaching 100% with only minor post-synthetic treatment.[25,26] Similar to other semiconductor NCs, the optical and structural properties of perovskite NCs depend on their size, changing significantly when the diameter or edge length is less than or equal to the material's bulk Bohr exciton diameter,[1,2,4–7,24] warranting an investigation into the size-dependence of the pressure-response of the optical gap.

As discussed in section 3.4.1, many MHP NC systems undergo an isostructural solid-solid phase transition from their ambient orthorhombic perovskite phase (γ-phase) to a second orthorhombic perovskite phase under hydrostatic pressure.[27–32] This isostructural phase transition manifests itself in a change in the mode of deformation as pressure increases further. Because the crystal symmetry does not change in an isostructural phase transition, the increase in surface indices, generally found in high-pressure crystal phases, does not occur. Therefore, it is not at all clear *a priori* whether such pressure-induced phase changes follow a similar size dependence as in other materials, or whether MHPs display a qualitatively different behavior.

In this chapter, I will present results on the detailed size dependent pressure-response of the PL of $CsPbBr_3$ nanocrystals. Studies like this are necessary to understand the interplay of structural and electronic properties in MHPs which can in turn help optimize their performance in devices.[33–37]

4.2 CsPbBr$_3$ Nanocrystal Synthesis

Recent improvements in methods for synthesizing NCs with higher stability and narrower size distributions[7,26,38,39] allow detailed size-dependent experiments for $CsPbBr_3$ NCs. We tuned the size of the NCs by controlling the Br^-:Pb^{2+} ratio using oleylammonium bromide (OLA-Br). $CsPbBr_3$ NCs have Br^- rich surfaces, so as the Br^-:Pb^{2+} ratio increases, smaller NCs with larger surface to volume ratios are thermodynamically favored.[7,38] This removes the difficulty of trying to control the NC size through kinetics, which is nearly impossible due to the very fast nucleation and growth kinetics of MHP NCs.[7,38] The OLA-Br was synthesized by adding 1 mL of HBr

(Sigma-Aldrich, reagent grade 48%) to 10 mL of purified oleylamine (OLA)[40] with vigorous stirring. This must be done slowly, as the reaction is very exothermic.

For the NC synthesis, 75 mg of $PbBr_2$ (Aldrich, ≥ 98%), 5 mL of 1-octadecene (ODE) (Aldrich, technical grade 90%), 0.5 mL of oleic acid (OA) (Aldrich, technical grade 90%), and a total of 0.5 mL of OLA and OLA-Br were added to a 25 mL three neck round bottom flask. We changed the $Br^-:Pb^{2+}$ ratio by adjusting the OLA-Br:OLA ratio while keeping the final volume consistent across all syntheses.

In a separate 25 mL round bottom flask, we added 162.5 mg of Cs_2CO_3 (Aldrich, 99%), 9 mL of ODE and 1 mL of OA to make Cs-oleate. Both flasks were heated to 120° C under vacuum with rapid stirring for 1 hour to remove dissolved atmospheric gases. Next, the flask containing the $PbBr_2$ was filled with nitrogen gas and brought to a temperature between 80° C and 160° C depending on the desired NC size.[7] The lower the temperature, the smaller the final NCs were. The Cs-precursor flask was also filled with nitrogen and allowed to cool to 100° C. Then 0.5 mL of the Cs-oleate solution was drawn into a nitrogen purged syringe through a rubber septum in the round bottom flask and swiftly injected into the $PbBr_2$ containing solution. This reaction mixture was then cooled down to room temperature by immersing in a room temperature water bath. Since NC size is determined by the Br:Pb ratio rather than by the kinetics of the reaction, it was not necessary to cool the solution rapidly after adding the Cs-oleate.[41]

The monodispersity of the crude reaction mixture varied from one reaction to the next, so in order to increase the monodispersity of NCs, 10 mL of anhydrous hexanes (Sigma-Aldrich, mixture of isomers anhydrous ≥ 99%) were added immediately after the reaction mixture had cooled to room temperature.[26] This disperses all the $CsPbBr_3$ NCs, but does not disperse unreacted precursors or large $CsPbBr_3$ aggregates. This turbid mixture was centrifuged and the supernatant containing the synthesized colloidal NCs was saved as the first size fraction. Next, dry nitrogen was blown over the surface of the colloid to slowly evaporate off hexanes. Hexanes are a better solvent for $CsPbBr_3$ NCs than ODE, so upon sufficient evaporation of hexanes, the concentration of ODE reaches a point where largest NCs began to precipitate out of the colloidal solution. This event causes a sudden visual change in the solution from transparent to turbid. This turbid solution was then centrifuged, with the first NC size fraction in the pellet and the rest of the colloidal NCs remaining in the hexanes/ODE solution. This procedure was repeated until there were no hexanes remaining. NCs from each size fraction were resuspended in anhydrous hexanes for characterization. Only the most monodisperse samples were used in high-pressure experiments.

4.2.1 $CsPbBr_3$ Nanocrystal Characterization

Each size fraction of $CsPbBr_3$ NCs was characterized using photoluminescence, transmission electron microscopy, and powder x-ray diffraction. Each size fraction used had bright PL, with monodispersity on par with the best results reported in the literature at this point.[24]

4.2.1.1 Ambient Photoluminescence

To be consistent with the PL measurements under pressure, the perovskite NCs were resuspended in the hydrostatic medium, paraffin oil (Fluka Analytical). Paraffin oil is a poor solvent for the NCs (similar to ODE) so the solutions were very dilute colloids. Solutions were excited using a continuous wave 406 nm diode laser focused into the cuvette with an intensity of 0.1 W/cm^2. The spectra were measured using a fiber optic spectrometer (Avantes AvaSpec-2048, 300 lines/mm, 2.5 nm resolution, Avantes, 400 μm core UV-Vis-NIR fiber). The resulting PL spectra are displayed in Figure 4.1.

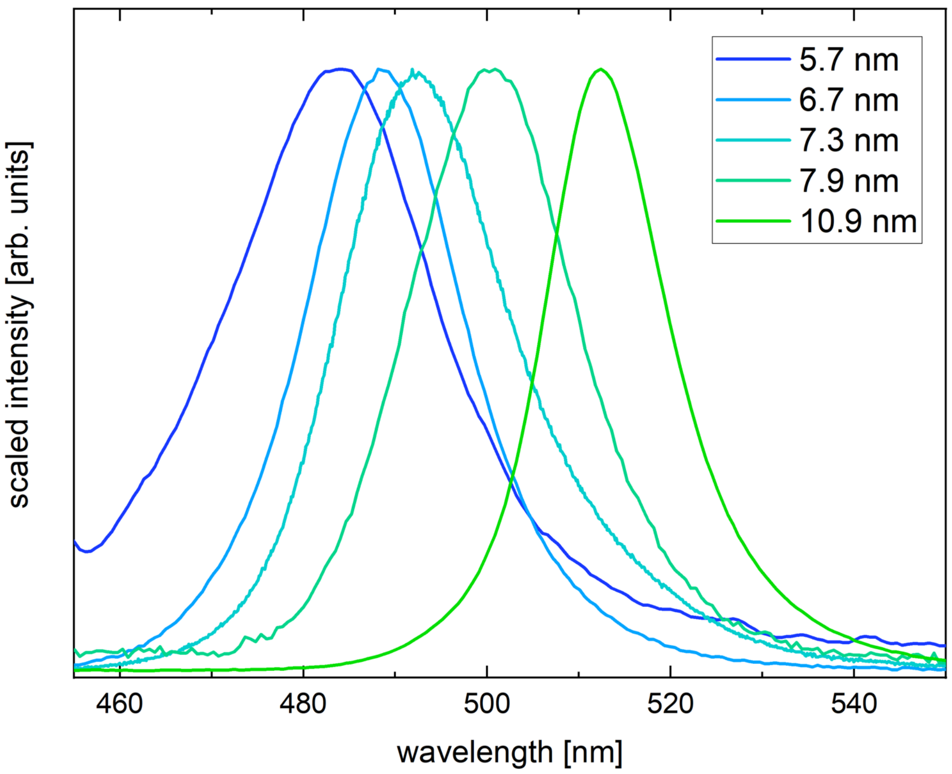

Figure 4.1: PL spectra of NC size fractions in paraffin oil at ambient pressure. Difference in PL full width half maximum (FWHM) are due to shorter lifetimes for smaller NCs, not from size distributions.

4.2.1.2 Transmission Electron Microscopy

Transmission electron microscopy (TEM) images were acquired using a FEI Tecnai ST20 and a FEI Tecnai F20 with an accelerating voltage of 200 kV. TEM samples were prepared by drop casting dilute hexanes solutions of NCs onto 300 mesh carbon film copper grids (Electron Microscopy Sciences) and allowing the hexanes to evaporate. The size analyses for all size samples are shown in Figure 4.2. All size distributions have ~10% error which is standard for metal halide perovskite NC samples with the current size selective techniques.[24]

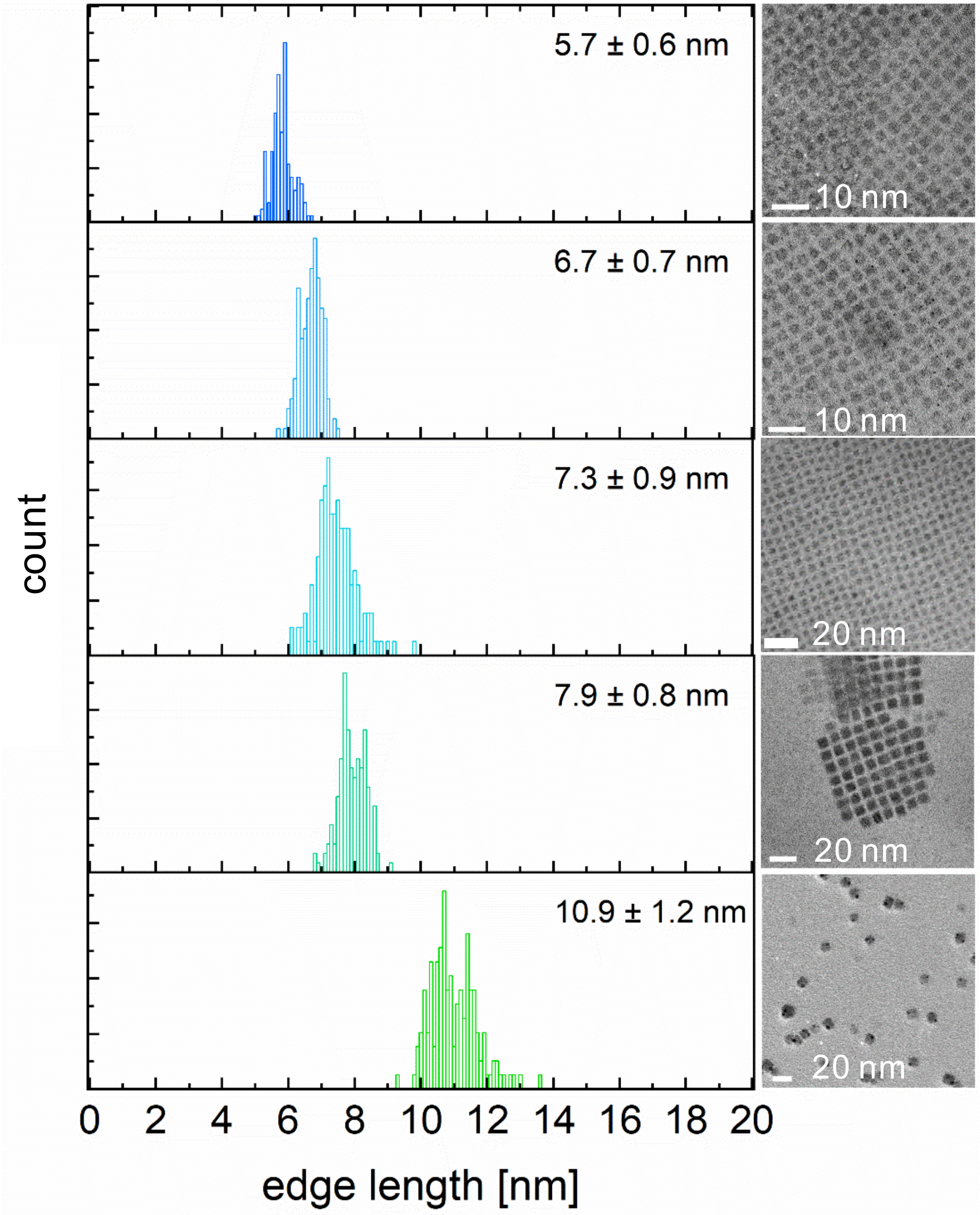

Figure 4.2: Size distributions and characteristic sample TEM images of all the NC samples studied. Each size distribution was obtained by determining the sizes of 150 NCs.

4.2.1.3 Discussion of the Ambient Crystal Structure of $CsPbBr_3$ Perovskite Nanocrystals

Before addressing the PL pressure response in detail, it is necessary to discuss the crystal structure of $CsPbBr_3$ NCs. As discussed in section 3.4.1, there was disagreement in the literature over the crystal structure they adopt at ambient temperature and pressure, as early as when cesium lead halide perovskite NCs were first synthesized.[6,42,43] Even in the most recent literature, this ambiguity remains as NCs with different sizes have been reported to have different crystal structures. Making matters more complicated, according to one report, NCs with about 10 nm edge length can have a mixture of crystal structures at room temperature and ambient pressure. Atomically resolved high resolution transmission electron microscopy (HRTEM) of $CsPbBr_3$ NCs by Brennen et al. revealed that NCs with 5 nm edge length were entirely cubic in crystal structure, even though larger NCs were at least partially orthorhombic.[44] For 5 nm nanocrystals (and up to at least 6.5 nm), X-ray diffraction (XRD) patterns suffer from Scherrer broadening that made it impossible with certain samples to unambiguously distinguish cubic from orthorhombic based on XRD alone.[34,45] Further, there is evidence of the coexistence of tetragonal and orthorhombic crystal structures in $CsPbBr_3$ NCs at liquid helium temperature, even though the orthorhombic to tetragonal phase transition is at 88 °C in bulk $CsPbBr_3$.[45,46] The complicated identification of crystal structure is not unique to MHPs, similar behavior has been observed in oxide perovskites, where the structure of crystalline domains can vary, even in nanocrystalline samples. For example, $BaTiO_3$ NCs have a cubic “shell” surrounding a tetragonal “core.”[47]

4.2.1.4 Powder X-Ray Diffraction

We analyzed our samples by XRD (Figure 4.3) at ambient temperature and pressure. For sizes ≤ 8 nm, the broadening due to overlap of the large number of diffraction features and Scherrer broadening make it impossible to make a conclusive assignment. Nevertheless, we do observe diffraction features for $22^\circ \leq 2\theta \leq 30^\circ$ for each size studied here that do not belong in the α-phase pattern, suggesting the γ perovskite crystal structure for all of our samples. The main difference between the cubic α-phase and the orthorhombic γ-phase is the symmetry reducing tilt of the $PbBr_6$ octahedra. The reduced symmetry of the γ-phase adds diffraction features to the XRD pattern, often clustered around angles seen in the α-phase pattern; however, it does not remove any of the features associated with the cubic structure. In $CsPbI_3$ NCs, the crystals adopt the γ-phase for all sizes that have been studied, although the smallest nanocrystals exhibit less of an octahedral tilt than the larger nanocrystals, decreasing the deviation from a cubic structure.[24] The small deviations from the cubic phase make the diffraction features associated with the orthorhombic phase even less pronounced. While the assignment of orthorhombic may seem to contradict the HRTEM results mentioned above, HRTEM is biased toward the structure of the surface, which likely exhibits even less octahedral tilt (resulting in an essentially cubic character) due to the high surface tension of NCs.[34,47]

Taking our data and the recent results by Luther and coworkers on $CsPbI_3$ NCs into account,[24] we assume that the $CsPbBr_3$ NC in the present work are orthorhombic for all sizes due to the existence of features in the XRD patterns that should not exist if the samples were cubic. The smallest sizes likely experience less of an octahedral tilt, making them nearly cubic as was observed in $CsPbI_3$ NCs.[24,34,42–44]

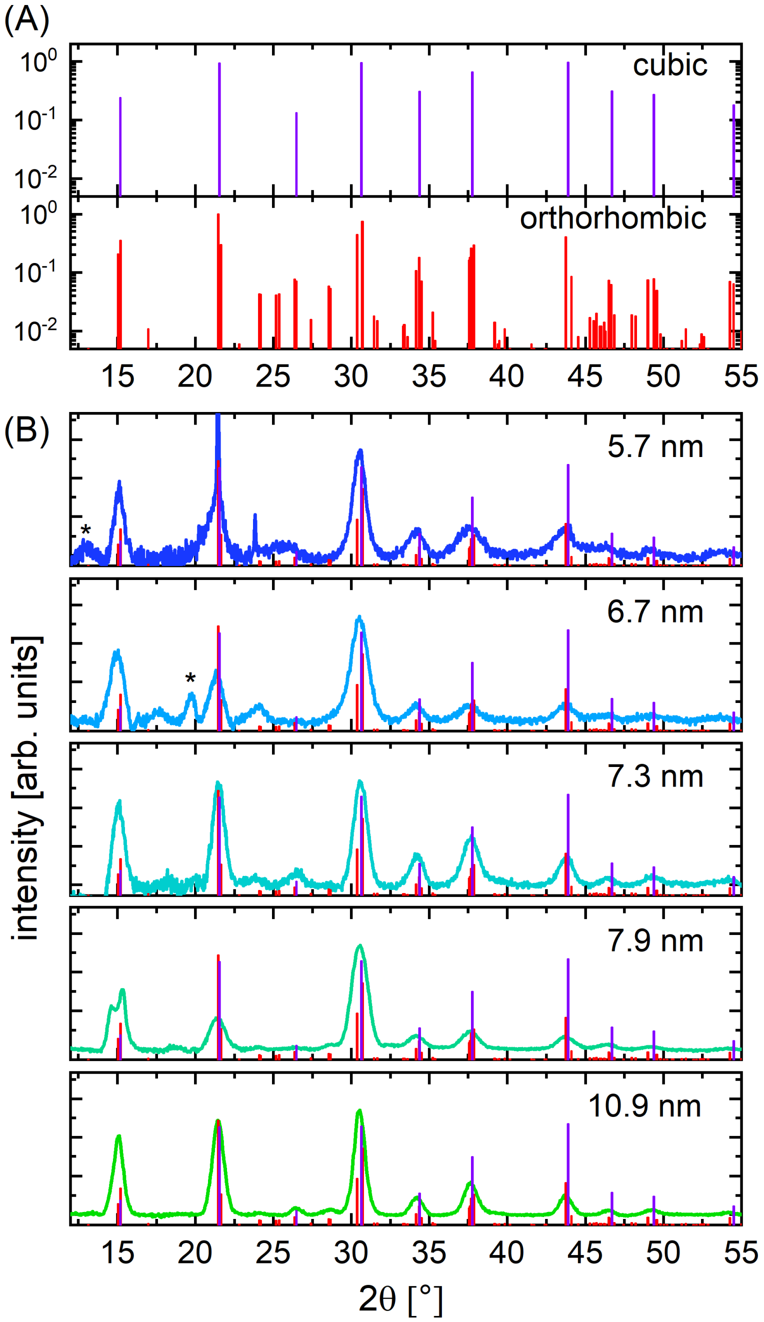

Figure 4.3: XRD Analysis of all nanocrystal samples used in our experiments. Part (A) shows simulations for cubic and orthorhombic structures as a semi-logarithmic plot to accentuate the low-intensity reflections. The red lines represent the orthorhombic perovskite pattern[48] and the violet lines are for the cubic perovskite crystal structure.[49] Part (B) shows a comparison of experimental XRD data with the simulated patterns (linear scale). Peaks marked with an asterisk (appearing in some of the samples, most clearly for 5.7 nm and 6.7 nm edge length) are due to residual precursor material.

4.3 PL Pressure-Response of $CsPbBr_3$ Nanocrystal Samples

The pressure induced phase changes in MHPs are conveniently accompanied by changes in the behavior of the PL under pressure.[27,28,32,34] This allows structural information to be studied by monitoring the PL spectrum of a NC sample as a function of pressure. While *in situ* XRD is needed to initially determine the pressure dependent phase behavior of a material, once the PL response is known it can be used to track the same changes in a given material.[34,45,46] This gives us the ability to understand trends in the size-dependent structural behavior under pressure without the need to use a synchrotron x-ray source. This approach has been used from the earliest experiments on the pressure response of semiconductor NCs[50] to monitor phase change behavior in high-pressure experiments, and has more recently also been employed for perovskite NCs in both high-pressure and temperature dependent experiments.[27,28,34]

As a simple, phenomenological description of the pressure response, the pressure dependent change of the PL peak energy from ambient can be written as

$$\Delta E(p) = E(p_0) + \alpha(p)p \tag{4.1}$$

where α is a (pressure dependent) pressure coefficient encoding the shift of the PL peak. As discussed in section 3.5, a transition pressure has been shown to exist for various MHPs where the response of their electronic structure to further pressure increase changes from a red shift to a blue shift, i.e., where $\alpha(p)$ changes its sign.[27–29,51,52] This sign change can be explained by the orbital contributions to the band structure and by the change in the mode of deformation at the transition pressure.

In lead halide perovskites, the behavior of the crystal structure under pressure and the accompanying effect on the electronic structure is well known.[27–29,32] For $CsPbBr_3$, the density of states at the valence band maximum (VBM) consists of Pb 6*s* and bromide 4*p* orbitals with anti-bonding interaction between the two.[27,53–55] The conduction band minimum (CBM) is largely formed from Pb 6*p* orbitals and bromide 4*p* orbitals with non-bonding interactions between them.[27,53–55] As the crystal lattice responds to pressure, the mode of deformation is first characterized by isotropic compression of the $PbBr_6$ octahedra, forcing greater overlap of the antibonding configuration of the Pb 6*s* and bromide 4*p* orbitals.[20,54,56] The compression of the octahedra therefore causes an increase the VBM energy, while leaving the CBM largely unaffected. This causes a decrease of the band gap that manifests itself as a red shift of the PL peak.

At the transition pressure, the mode of deformation changes concomitant with the aforementioned isostructural phase transition.[30] As the pressure is increased further, instead of continued octahedral compression, the octahedra begin to distort and tilt relative to one another, but for $CsPbBr_3$, they preserve the overall orthorhombic crystal symmetry.[27,42,43] This octahedral tilting and deformation diminishes the Pb character of the CBM and with it the stabilization of the CBM afforded by the spin orbit coupling in the Pb atoms.[53,57] Consequently, the CBM energy increases, while the VBM is mostly unaffected, which results in a blue shift of the PL spectrum. This change in the sign of the pressure coefficient is a direct result of the change in the mode of deformation of the crystal lattice and the isostructural phase transition, so it can be used to track this structural change without using *in situ* x-ray diffraction measurements.

The transition pressure and the pressure coefficients α for each NC size were found by pressurizing our NC samples in a diamond anvil cell while tracking the PL peak energy (Figure 4.4). Finally, the magnitude of the initial pressure coefficient α, which is defined as $\alpha = dE/dp$, is relatively constant and close to the reported bulk value for NCs with edge lengths above 7.5 nm, then decreases in magnitude for edge lengths below 7 nm (Figure 4.6). We will discuss these phenomena as follows by taking into account the surface-to-volume ratio, together with the transition to the strong confinement regime below 7.5 nm.[14,15,17,58,59]

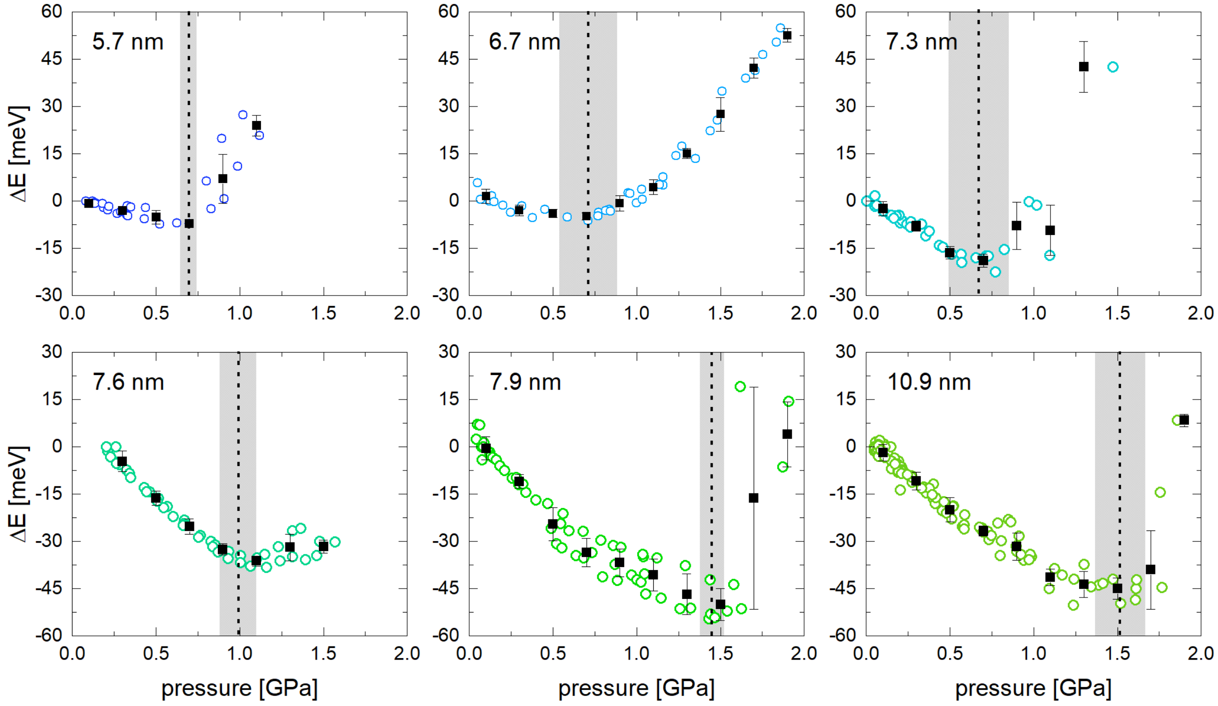

Figure 4.4: PL pressure response of NC samples studied in the present work. Open circles are raw data coming from at least two high pressure runs for each size, and black squares are the mean *ΔE* binned in pressure intervals of 0.2 GPa. The transition pressure is marked with vertical dotted lines with the uncertainty shaded in gray. The uncertainty in pressure for each data point is ±75 MPa.

The transition pressure decreases slightly with decreasing NC size for NCs above 7.5 nm, exhibits a step-like decrease as edge length decreases below ca. 7.5 nm, and remains at a constant value as the size is decreased further (Figure 4.5). For the largest NC samples studied, the transition pressure is slightly higher than in bulk samples. In contrast with other NC materials, the change in the mode of deformation at the isostructural phase transition point in MHPs by definition does not change the lattice indices of their facets.[27–29] Without significant surface rearrangement, there is probably no large penalty in the surface energy, so the change in the overall internal energy of the NCs at the transition does not increase drastically as the NC size decreases.

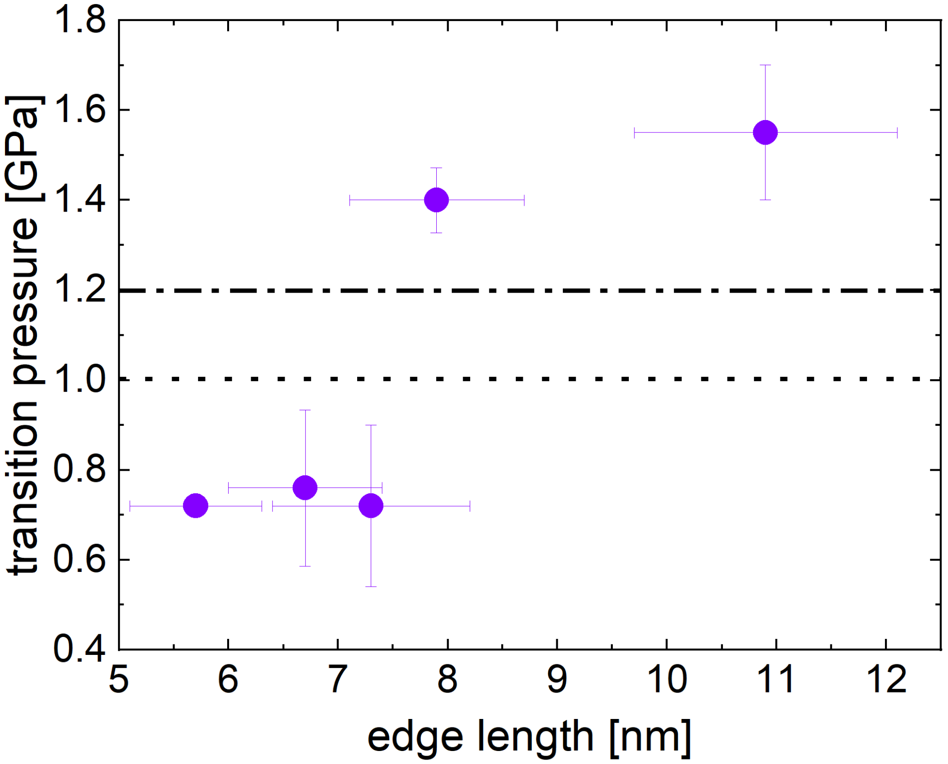

Figure 4.5: The transition pressure at which the PL turns from a red shift to a blue shift as a function of NC size. This is compared to the transition pressure in bulk $CsPbBr_3$ (dotted line) and the corresponding value reported in Xiao *et al.*[28] for 11.9 nm $CsPbBr_3$ NCs (dash-dotted line).

For the smallest sizes, the fluctuation length scale that can cause an isostructural phase transition involving a different octahedral tilt could be shorter than for the larger NCs, leading to a phase transition sooner since NCs undergo phase transitions starting from one nucleation site that quickly propagates through the rest of the crystal.[13,17,50,58,59] Furthermore, low energy Raman spectroscopy results on $CsPbBr_3$ have shown that local polar fluctuations at room temperature cause the Cs^+ ion to be displaced off center, inducing tilting in the octahedra.[60] With a higher surface-to-volume ratio and the surface acting as a nucleation site, these fluctuations that tilt the octahedra on small NCs may be more likely to cause a coherent phase transition at a lower pressure than in larger NCs, leading to a lower transition pressure.

The transition pressure for NCs with sizes from 5.7 nm to 7.3 nm edge length remains constant around 0.75 GPa, all of which have physical sizes equal to or smaller than the bulk Bohr exciton diameter ca. 7.5 nm.[46] The consistency in the transition pressure as the size is decreased below 7.5 nm, may be an indication that crossing over into the strong quantum confinement regime in the NCs plays a role in the structural transition. Charge carriers form large polarons in $CsPbBr_3$, distorting the crystal lattice upon photoinduced excitation.[61] This distortion can actually cause a reversible photoinduced phase transition when 400 nm light excites $CsPbBr_3$ NCs (ca. 11 nm), lasting on the order of 5 ns.[62] These NCs undergo an orthorhombic to cubic phase transition, which happens because the excitation causes a lattice dilation, subsequently rotating the octahedra so that the Pb-Br-Pb bond angles increase to 180°. Photoexcitation in the cubic perovskite methyl ammonium lead iodide ($MAPbI_3$) causes a distortion in the PbI_6 octahedra away from the cubic structure,[63] not unlike the distortion found in the high-pressure phase of $CsPbBr_3$ NCs.[28] The photoinduced structural changes are not due to local heating of the sample, but are direct results of coupling to phonon modes.[62,63] The nanocrystals below 7.5 nm edge length adopt an orthorhombic crystal structure that is already closer to the cubic phase than the larger NCs as discussed above. Therefore, it is possible that the photoexcitation in these small NCs induces an octahedral distortion characteristic of the higher-pressure orthorhombic phase. Under hydrostatic pressure, this photoinduced distortion is no longer only metastable, but becomes favored when the distortion is enough to overcome the barrier of the phase transformation to the high-pressure phase. This would initiate the band gap widening by decreasing the Pb 6*p* character in the CBM as the pressure is increased further, changing the sign of α. It is important to note that our PL measurements do not provide information about octahedral tilt or distortion at any given pressure, but they can tell us about a change in octahedral tilt or distortion from one pressure to the next, since an increase in the tilt/distortion causes destabilization of the CBM.

In addition to having a lower transition pressure, NCs below 7.5 nm edge length also show a smaller magnitude of the initial pressure coefficient for the isotropic compression phase (Figure 4.6). As nanocrystal size decreases below the bulk Bohr exciton radius, the wavefunction is delocalized over the entire nanocrystal, coupling the core states to surface polaronic states.[64–66]

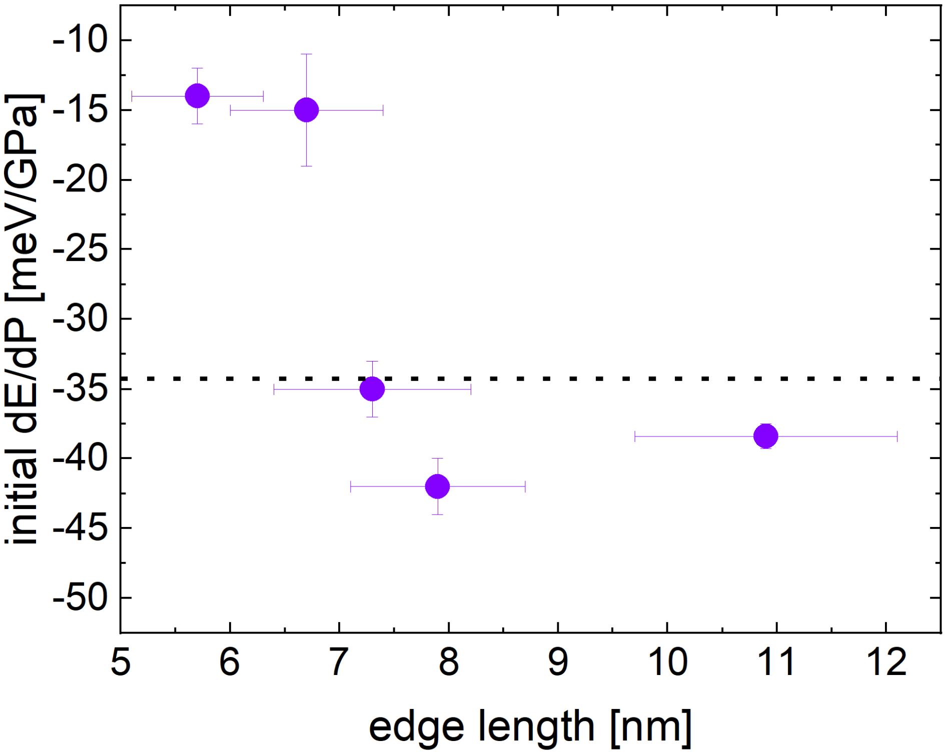

Figure 4.6: The magnitude of the initial pressure coefficient decreases as NC size increases. The dotted line represents the bulk pressure coefficient reported in Zhang *et al.*[67]

The surface polaronic states are below the band gap energy and are less affected by perturbations to the crystal lattice than the core electronic states in NCs are. This would predict that for NCs in the strong confinement regime, the pressure coefficient measured from tracking PL would approach zero, as there is a low tunneling barrier to the surface polaronic states due to the strong coupling (Figure 4.7). This has been experimentally shown for CdSe NCs.[66] Likewise, our data show that $CsPbBr_3$ NCs that are smaller than the bulk Bohr exciton radius experience a large drop in the magnitude of the pressure coefficient, likely due to the strong coupling to surface polarons.

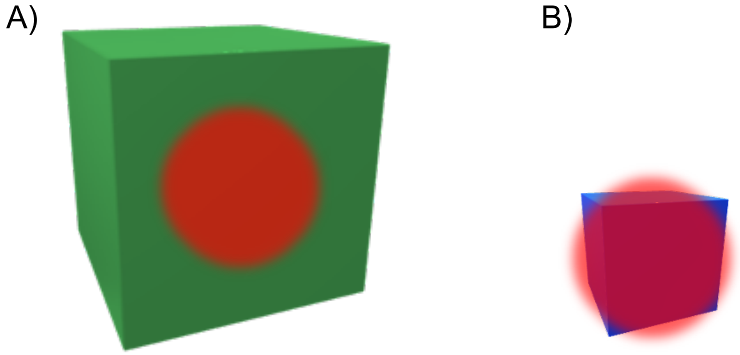

Figure 4.7: (A) Large NC showing exciton wave function within the bulk of the crystal, which produces lower coupling to surface states. (B) Small NC showing exciton wavefunction extending to the surface of the NC, which enhances the coupling to surface states.

4.4 Conclusion

In summary, we have probed the isostructural phase transition pressures and pressure coefficients for a range of sizes of $CsPbBr_3$ NCs using PL spectroscopy. Contrary to NC systems whose pressure induced solid-solid phase transitions involve changing the crystal symmetry, we observed a reduction in the phase transition pressure as NC size decreases. We explain this observation by the fact that the lowest pressure phase transition in perovskite NCs does not lead to the formation of high index facets, so the energy barrier for the phase transition is not drastically increased as NC size decreases. Furthermore, the smaller size of the NCs means that the fluctuation length scale needed to cause a coherent transition is necessarily smaller than for the larger NCs. The NCs with the strongest quantum confinement exhibit both a drop in the transition pressure as well as the magnitude of the pressure coefficient. Both of these effects can be explained by the complete delocalization of the wavefunction over the whole NC, allowing strong coupling to polaronic states.

4.5 References

(1) Rossetti, R.; Ellison, J. L.; Gibson, J. M.; Brus, L. E. Size Effects in the Excited Electronic States of Small Colloidal CdS Crystallites. *J. Chem. Phys.* **1984**, *80*, 4464.

(2) Norris, D. J.; Bawendi, M. G. Measurement and Assignment of the Size-Dependent Optical Spectrum in CdSe Quantum Dots. *Phys. Rev. B Condens. Matter Mater. Phys.* **1996**, *53*, 16338.

(3) Brus, L. E. Electron–Electron and Electron-Hole Interactions in Small Semiconductor Crystallites: The Size Dependence of the Lowest Excited Electronic State. *J. Chem. Phys.* **1984**, *80*, 4403.

(4) Wang, Y.; Herron, N. Nanometer-Sized Semiconductor Clusters: Materials Synthesis, Quantum Size Effects, and Photophysical Properties. *J. Phys. Chem.* **1991**, *95*, 525.

(5) Steigerwald, M. L.; Brus, L. E. Semiconductor Crystallites: A Class of Large Molecules. *Acc. Chem. Res.* **1990**, *23*, 183.

(6) Protesescu, L.; Yakunin, S.; Bodnarchuk, M. I.; Krieg, F.; Caputo, R.; Hendon, C. H.; Yang, R. X.; Walsh, A.; Kovalenko, M. V. Nanocrystals of Cesium Lead Halide Perovskites (CsPbX3, X = Cl, Br, and I): Novel Optoelectronic Materials Showing Bright Emission with Wide Color Gamut. *Nano Lett.* **2015**, *15*, 3692.

(7) Dong, Y.; Qiao, T.; Kim, D.; Parobek, D.; Rossi, D.; Son, D. H. Precise Control of Quantum Confinement in Cesium Lead Halide Perovskite Quantum Dots via Thermodynamic Equilibrium. *Nano Lett.* **2018**, *18*, 3716.

(8) Bawendi, M. G.; Steigerwald, M. L.; Brus, L. E. The Quantum Mechanics of Larger

Semiconductor Clusters (“Quantum Dots”). *Annu. Rev. Phys. Chem.* **1990**, *41* (1), 477–496.

(9) Ellingson, R. J.; Beard, M. C.; Johnson, J. C.; Yu, P.; Micic, O. I.; Nozik, A. J.; Shabaev, A.; Efros, A. L. Highly Efficient Multiple Exciton Generation in Colloidal PbSe and PbS Quantum Dots. *Nano Lett.* **2005**, *5* (5), 865–871.

(10) Beard, M. C.; Blackburn, J. L.; Johnson, J. C.; Rumbles, G. Status and Prognosis of Future-Generation Photoconversion to Photovoltaics and Solar Fuels. *ACS Energy Lett.* **2016**, *1* (2), 344–347.

(11) Nozik, A. J. Multiple Exciton Generation in Semiconductor Quantum Dots. *Chem. Phys. Lett.* **2008**, *457* (1), 3–11.

(12) Goldstein, A. N.; Echer, C. M.; Alivisatos, A. P. Melting in Semiconductor Nanocrystals. *Science (80-.).* **1992**, *256*, 1425.

(13) Tolbert, S. H.; Alivisatos, A. P. High-Pressure Structural Transformations in Semiconductor Nanocrystals. *Annu. Rev. Phys. Chem.* **1995**, *46*, 595.

(14) Tolbert, S. H.; Alivisatos, A. P. The Wurtzite to Rock Salt Structural Transformation in CdSe Nanocrystals Under High Pressure. *J. Chem. Phys.* **1995**, *102*, 4642.

(15) Chen, C.-C.; Herhold, A. B.; Johnson, C. S.; Alivisatos, A. P. Size Dependence of Structural Metastability in Semiconductor Nanocrystals. *Science (80-.).* **1997**, *276*, 398.

(16) Chen, Z.; Sun, C. Q.; Zhou, Y.; Ouyang, G. Size Dependence of the Pressure-Induced Phase Transition in Nanocrystals. *J. Phys. Chem. C* **2008**, *112*, 2423.

(17) Tolbert, S. H.; Herhold, A. B.; Brus, L. E.; Alivisatos, A. P. Pressure-Induced Structural Transformations in Si Nanocrystals: Surface and Shape Effects. *Phys. Rev. Lett.* **1996**, *76*, 4384.

(18) Milstein, T. J.; Kroupa, D. M.; Gamelin, D. R. Picosecond Quantum Cutting Generates

Photoluminescence Quantum Yields Over 100% in Ytterbium-Doped CsPbCl3 Nanocrystals. *Nano Lett.* **2018**, *18*, 3792.

(19) Fu, Y.; Zhu, H.; Chen, J.; Hautzinger, M. P.; Zhu, X. Y.; Jin, S. Metal Halide Perovskite Nanostructures for Optoelectronic Applications and the Study of Physical Properties. *Nat. Rev. Mater.* **2019**, *4*, 169.

(20) Manser, J. S.; Christians, J. A.; Kamat, P. V. Intriguing Optoelectronic Properties of Metal Halide Perovskites. *Chem. Rev.* **2016**, *116*, 12956.

(21) Akkerman, Q. A.; Rainò, G.; Kovalenko, M. V; Manna, L. Genesis, Challenges and Opportunities for Colloidal Lead Halide Perovskite Nanocrystals. *Nat. Mater.* **2018**, *17*, 394.

(22) Jena, A. K.; Kulkarni, A.; Miyasaka, T. Halide Perovskite Photovoltaics: Background, Status, and Future Prospects. *Chem. Rev.* **2019**, *119*, 3036.

(23) Shamsi, J.; Urban, A. S.; Imran, M.; De Trizio, L.; Manna, L. Metal Halide Perovskite Nanocrystals: Synthesis, Post-Synthesis Modifications, and Their Optical Properties. *Chem. Rev.* **2019**, *119*, 3296.

(24) Zhao, Q.; Hazarika, A.; Schelhas, L. T.; Liu, J.; Gaulding, E. A.; Li, G.; Zhang, M.; Toney, M. F.; Sercel, P. C.; Luther, J. M. Size-Dependent Lattice Structure and Confinement Properties in CsPbI3 Perovskite Nanocrystals: Negative Surface Energy for Stabilization. *ACS Energy Lett.* **2020**, *5*, 238.

(25) Koscher, B. A.; Swabeck, J. K.; Bronstein, N. D.; Alivisatos, A. P. Essentially Trap-Free CsPbBr3 Colloidal Nanocrystals by Postsynthetic Thiocyanate Surface Treatment. *J. Am. Chem. Soc.* **2017**, *139*, 6566.

(26) Nenon, D. P.; Pressler, K.; Kang, J.; Koscher, B. A.; Olshansky, J. H.; Osowiecki, W. T.;

Koc, M. A.; Wang, L.-W.; Alivisatos, A. P. Design Principles for Trap-Free CsPbX3 Nanocrystals: Enumerating and Eliminating Surface Halide Vacancies with Softer Lewis Bases. *J. Am. Chem. Soc.* **2018**, *140*, 17760.

(27) Beimborn, J. C.; Hall, L. M. G.; Tongying, P.; Dukovic, G.; Weber, J. M. Pressure Response of Photoluminescence in Cesium Lead Iodide Perovskite Nanocrystals. *J. Phys. Chem. C* **2018**, *122* (20), 11024–11030.

(28) Xiao, G.; Cao, Y.; Qi, G.; Wang, L.; Liu, C.; Ma, Z.; Yang, X.; Sui, Y.; Zheng, W.; Zou, B. Pressure Effects on Structure and Optical Properties in Cesium Lead Bromide Perovskite Nanocrystals. *J. Am. Chem. Soc.* **2017**, *139*, 10087.

(29) Cao, Y.; Qi, G.; Liu, C.; Wang, L.; Ma, Z.; Wang, K.; Du, F.; Xiao, G.; Zou, B. Pressure-Tailored Band Gap Engineering and Structure Evolution of Cubic Cesium Lead Iodide Perovskite Nanocrystals. *J. Phys. Chem. C* **2018**, *122*, 9332.

(30) Kincaid, J. M.; Stell, G.; Goldmark, E. Isostructural Phase Transitions Due to Core Collapse. II. A Three-Dimensional Model with a Solid–Solid Critical Point. *J. Chem. Phys.* **1976**, *65*, 2172.

(31) Li, M.; Liu, T.; Wang, Y.; Yang, W.; Lü, X. Pressure Responses of Halide Perovskites With Various Compositions, Dimensionalities, and Morphologies. *Matter Radiat. Extrem.* **2020**, *5*, 18201.

(32) Beimborn, J. C.; Walther, L. R.; Wilson, K. D.; Weber, J. M. Size-Dependent Pressure-Response of the Photoluminescence of CsPbBr3 Nanocrystals. *J. Phys. Chem. Lett.* **2020**, *11* (5), 1975–1980.

(33) Ashner, M. N.; Shulenberger, K. E.; Krieg, F.; Powers, E. R.; Kovalenko, M. V; Bawendi, M. G.; Tisdale, W. A. Size-Dependent Biexciton Spectrum in CsPbBr3 Perovskite

Nanocrystals. *ACS Energy Lett.* **2019**, *4*, 2639.

(34) Liu, L.; Zhao, R.; Xiao, C.; Zhang, F.; Pevere, F.; Shi, K.; Huang, H.; Zhong, H.; Sychugov, I. Size-Dependent Phase Transition in Perovskite Nanocrystals. *J. Phys. Chem. Lett.* **2019**, *10*, 5451.

(35) Brennan, M. C.; Herr, J. E.; Nguyen-Beck, T. S.; Zinna, J.; Draguta, S.; Rouvimov, S.; Parkhill, J.; Kuno, M. Origin of the Size-Dependent Stokes Shift in CsPbBr3 Perovskite Nanocrystals. *J. Am. Chem. Soc.* **2017**, *139*, 12201.

(36) Butkus, J.; Vashishtha, P.; Chen, K.; Gallaher, J. K.; Prasad, S. K. K.; Metin, D. Z.; Laufersky, G.; Gaston, N.; Halpert, J. E.; Hodgkiss, J. M. The Evolution of Quantum Confinement in CsPbBr3 Perovskite Nanocrystals. *Chem. Mater.* **2017**, *29*, 3644.

(37) Scheidt, R. A.; Atwell, C.; Kamat, P. V. Tracking Transformative Transitions: From CsPbBr3 Nanocrystals to Bulk Perovskite Films. *ACS Mater. Lett.* **2019**, *1*, 8.

(38) Dutta, A.; Dutta, S. K.; Das Adhikari, S.; Pradhan, N. Tuning the Size of CsPbBr3 Nanocrystals: All at One Constant Temperature. *ACS Energy Lett.* **2018**, *3*, 329.

(39) Yoo, D.; Woo, J. Y.; Kim, Y.; Kim, S. W.; Wei, S.-H.; Jeong, S.; Kim, Y.-H. Origin of the Stability and Transition from Anionic to Cationic Surface Ligand Passivation of All-Inorganic Cesium Lead Halide Perovskite Nanocrystals. *J. Phys. Chem. Lett.* **2020**, *11*, 652.

(40) Baranov, D.; Lynch, M. J.; Curtis, A. C.; Carollo, A. R.; Douglass, C. R.; Mateo-Tejada, A. M.; Jonas, D. M. Purification of Oleylamine for Materials Synthesis and Spectroscopic Diagnostics for Trans Isomers. *Chem. Mater.* **2019**, *31* (4), 1223–1230.

(41) Shi, H.; Du, M.-H. Shallow Halogen Vacancies in Halide Optoelectronic Materials. *Phys. Rev. B* **2014**, *90* (17), 174103.

(42) Cottingham, P.; Brutchey, R. L. On The Crystal Structure of Colloidally Prepared CsPbBr3

Quantum Dots. *Chem. Commun.* **2016**, *52*, 5246.

(43) Bertolotti, F.; Protesescu, L.; Kovalenko, M. V; Yakunin, S.; Cervellino, A.; Billinge, S. J. L.; Terban, M. W.; Pedersen, J. S.; Masciocchi, N.; Guagliardi, A. Coherent Nanotwins and Dynamic Disorder in Cesium Lead Halide Perovskite Nanocrystals. *ACS Nano* **2017**, *11*, 3819.

(44) Brennan, M. C.; Kuno, M.; Rouvimov, S. Crystal Structure of Individual CsPbBr3 Perovskite Nanocubes. *Inorg. Chem.* **2019**, *58*, 1555.

(45) Fu, M.; Tamarat, P.; Huang, H.; Even, J.; Rogach, A. L.; Lounis, B. Neutral and Charged Exciton Fine Structure in Single Lead Halide Perovskite Nanocrystals Revealed by Magneto-Optical Spectroscopy. *Nano Lett.* **2017**, *17*, 2895.

(46) Ramade, J.; Andriambariarijaona, L. M.; Steinmetz, V.; Goubet, N.; Legrand, L.; Barisien, T.; Bernardot, F.; Testelin, C.; Lhuillier, E.; Bramati, A. Fine Structure of Excitons and Electron–Hole Exchange Energy in Polymorphic CsPbBr3 Single Nanocrystals. *Nanoscale* **2018**, *10*, 6393.

(47) Aoyagi, S.; Kuroiwa, Y.; Sawada, A.; Kawaji, H.; Atake, T. Size Effect on Crystal Structure and Chemical Bonding Nature in BaTiO3 Nanopowder. *J. Therm. Anal. Calorim.* **2005**, *81*, 627.

(48) Stoumpos, C. C.; Malliakas, C. D.; Peters, J. A.; Liu, Z.; Sebastian, M.; Im, J.; Chasapis, T. C.; Wibowo, A. C.; Chung, D. Y.; Freeman, A. J. Crystal Growth of the Perovskite Semiconductor CsPbBr3: A New Material for High-Energy Radiation Detection. *Cryst. Growth Des.* **2013**, *13*, 2722.

(49) Rodová, M.; Brožek, J.; Knížek, K.; Nitsch, K. Phase Transitions in Ternary Caesium Lead Bromide. *J. Therm. Anal. Calorim.* **2003**, *71*, 667.

(50) Tolbert, S. H.; Alivisatos, A. P. Size Dependence of the Solid-Solid Phase Transition in CdSe Nanocrystals. *Z. Phys. D At., Mol. Clust.* **1993**, *26*, 56.

(51) Li, Q.; Li, S.; Wang, K.; Quan, Z.; Meng, Y.; Zou, B. High-Pressure Study of Perovskite-Like Organometal Halide: Band-Gap Narrowing and Structural Evolution of [NH3-(CH2)4-NH3]CuCl4. *J. Phys. Chem. Lett.* **2017**, *8*, 500.

(52) Wang, L.; Wang, K.; Xiao, G.; Zeng, Q.; Zou, B. Pressure-Induced Structural Evolution and Band Gap Shifts of Organometal Halide Perovskite-Based Methylammonium Lead Chloride. *J. Phys. Chem. Lett.* **2016**, *7*, 5273.

(53) Lee, J.-H.; Bristowe, N. C.; Lee, J. H.; Lee, S.-H.; Bristowe, P. D.; Cheetham, A. K.; Jang, H. M. Resolving the Physical Origin of Octahedral Tilting in Halide Perovskites. *Chem. Mater.* **2016**, *28*, 4259.

(54) Prasanna, R.; Gold-Parker, A.; Leijtens, T.; Conings, B.; Babayigit, A.; Boyen, H.-G.; Toney, M. F.; McGehee, M. D. Band Gap Tuning via Lattice Contraction and Octahedral Tilting in Perovskite Materials for Photovoltaics. *J. Am. Chem. Soc.* **2017**, *139*, 11117.

(55) Garcia-Fernandez, P.; Aramburu, J. A.; Barriuso, M. T.; Moreno, M. Key Role of Covalent Bonding in Octahedral Tilting in Perovskites. *J. Phys. Chem. Lett.* **2010**, *1*, 647.

(56) Ghosh, D.; Aziz, A.; Dawson, J. A.; Walker, A. B.; Islam, M. S. Putting the Squeeze on Lead Iodide Perovskites: Pressure-Induced Effects To Tune Their Structural and Optoelectronic Behavior. *Chem. Mater.* **2019**, *31*, 4063.

(57) Amat, A.; Mosconi, E.; Ronca, E.; Quarti, C.; Umari, P.; Nazeeruddin, M. K.; Grätzel, M.; De Angelis, F. Cation-Induced Band-Gap Tuning in Organohalide Perovskites: Interplay of Spin–Orbit Coupling and Octahedra Tilting. *Nano Lett.* **2014**, *14*, 3608.

(58) Herhold, A. B.; Tolbert, S. H.; Guzelian, A. A.; Alivisatos, A. P.; Pelizzetti, E. *Fine*

Particles Science and Technology: From Micro to Nanoparticles; 1996.

(59) Grünwald, M.; Lutker, K.; Alivisatos, A. P.; Rabani, E.; Geissler, P. L. Metastability in Pressure-Induced Structural Transformations of CdSe/ZnS Core/Shell Nanocrystals. *Nano Lett.* **2013**, *13*, 1367.

(60) Yaffe, O.; Guo, Y.; Tan, L. Z.; Egger, D. A.; Hull, T.; Stoumpos, C. C.; Zheng, F.; Heinz, T. F.; Kronik, L.; Kanatzidis, M. G. Local Polar Fluctuations in Lead Halide Perovskite Crystals. *Phys. Rev. Lett.* **2017**, *118*, 136001.

(61) Puppin, M.; Polishchuk, S.; Colonna, N.; Crepaldi, A.; Dirin, D. N.; Nazarenko, O.; De Gennaro, R.; Gatti, G.; Roth, S.; Barillot, T.; Poletto, L.; Xian, R. P.; Rettig, L.; Wolf, M.; Ernstorfer, R.; Kovalenko, M. V.; Marzari, N.; Grioni, M.; Chergui, M. Evidence of Large Polarons in Photoemission Band Mapping of the Perovskite Semiconductor ${\mathrm{CsPbBr}}_{3}$. *Phys. Rev. Lett.* **2020**, *124* (20), 206402.

(62) Kirschner, M. S.; Diroll, B. T.; Guo, P.; Harvey, S. M.; Helweh, W.; Flanders, N. C.; Brumberg, A.; Watkins, N. E.; Leonard, A. A.; Evans, A. M.; Wasielewski, M. R.; Dichtel, W. R.; Zhang, X.; Chen, L. X.; Schaller, R. D. Photoinduced, Reversible Phase Transitions in All-Inorganic Perovskite Nanocrystals. *Nat. Commun.* **2019**, *10* (1), 504.

(63) Wu, X.; Tan, L. Z.; Shen, X.; Hu, T.; Miyata, K.; Trinh, M. T.; Li, R.; Coffee, R.; Liu, S.; Egger, D. A.; Makasyuk, I.; Zheng, Q.; Fry, A.; Robinson, J. S.; Smith, M. D.; Guzelturk, B.; Karunadasa, H. I.; Wang, X.; Zhu, X.; Kronik, L.; Rappe, A. M.; Lindenberg, A. M. Light-Induced Picosecond Rotational Disordering of the Inorganic Sublattice in Hybrid Perovskites. *Sci. Adv.* **2017**, *3* (7), e1602388.

(64) Efros, A. L.; Rosen, M. The Electronic Structure of Semiconductor Nanocrystals. *Annu. Rev. Mater. Sci.* **2000**, *30* (1), 475–521.

(65) Nirmal, M.; Brus, L. Luminescence Photophysics in Semiconductor Nanocrystals. *Acc. Chem. Res.* **1999**, *32* (5), 407–414.

(66) Meulenberg, R. W.; Strouse, G. F. Pressure-Induced Electronic Coupling in CdSe Semiconductor Quantum Dots. *Phys. Rev. B* **2002**, *66* (3), 35317.

(67) Zhang, L.; Zeng, Q.; Wang, K. Pressure-Induced Structural and Optical Properties of Inorganic Halide Perovskite CsPbBr3. *J. Phys. Chem. Lett.* **2017**, *8*, 3752.

(68) Nagaoka, Y.; Hills-Kimball, K.; Tan, R.; Li, R.; Wang, Z.; Chen, O. Nanocube Superlattices of Cesium Lead Bromide Perovskites and Pressure-Induced Phase Transformations at Atomic and Mesoscale Levels. *Adv. Mater.* **2017**, *29*, 1606666.

Chapter 5 Pressure Response of Rubrene Upconversion Photoluminescence Through Cation and Anion Sensitized Triplet-Triplet Annihilation

This chapter has been adapted with permission from:

Spectroscopy of Resonant Intermediate States for Triplet-Triplet Annihilation Upconversion in Crystalline Rubrene – Radical Ions as Sensitizers, Beimborn II, J. C.; Zagorec-Marks, W.; Weber, J. M., *J. Phys. Chem. Lett.,* 2020, 11, 17, 7212-7217. DOI: 10.1021/acs.jpclett.0c01999. Copyright 2020 American Chemical Society

5.1 Introduction

Organic semiconducting materials are much softer than inorganic semiconductors due to the weak nature of the van der Waals forces that hold the crystal together. This makes pressure an obvious tool to probe how changes to the intermolecular distances affect the electronic structure of the organic material. A number of organic semiconducting materials have the ability to undergo single fission (SF) which has potential to improve photovoltaic efficiencies.[1] SF takes place when a singlet Frenkel exciton localized on a single molecule can share its energy with a neighboring ground state molecule, splitting the singlet exciton and creating two triplet excitons.[1–3] This is a spin allowed process because the triplet pair, ^{1}(TT) is still a singlet overall.[1] There are many factors that go into whether or not an organic material will be able to undergo SF, but one important feature the material must have is sufficient intermolecular coupling.[1,4,5] Efficient SF also requires that

$$E(S_1) - 2E(T_1) \geq 0 \tag{5.1}$$

where $E(S_1)$ is the energy of the first singlet excited state and $E(T_1)$ is the energy of the first triplet state. For negative energy differences close enough to zero, SF can still happen through thermal activation.

This phenomenon has gained a lot of interest because it could improve the efficiency of organic photovoltaics (OPV) devices by creating two excitons from only one absorbed photon.[1,4,6] SF can be a faster process than fluorescence in some organic materials, even if thermal activation is required. In rubrene (5,6,11,12-tetraphenyltetracene, see Figure 5.1) crystals, $E(S_1) = 2.23$ eV and $E(T_1) = 1.14$ eV, so $E(S_1) - 2E(T_1) = -0.05$ eV, which means with thermal activation, SF should occur.[7] The SF rate constant has been measured to be 5×10^{10} s^{-1} when exciting above the band gap (3.12 eV excitation energy, 2.23 eV band gap energy) while the fluorescence rate constant is only 6.25×10^{7} s^{-1},[7,8] and SF is responsible for quenching 99.9% of the fluorescence in rubrene crystals.[9]

The reverse process where two triplet excitons fuse to make one singlet exciton can occur as well.[6,10,11] It happens through the same intermolecular electronic coupling process as SF, but in reverse. Unlike fission, it requires that the two triplet excitons collide for TTA to occur. TTA was first observed by Parker and co-workers over fifty years ago,[12] but has recently regained interest due to applications in improved OPV efficiency,[13–15] medical imaging,[16] and photocatalysis.[17] The effects of intermolecular coupling on SF and TTA have been studied extensively in the past by changing the rates of SF in different polymorphs, by adding different functional groups, or by covalently bridging dimers.[2,3,18–20] By using high-pressure to alter the crystal structure of a material, a continuous picture can be built up to how SF or TTA are affected by the pressure induced changes in intermolecular coupling, rather than the discrete, and perturbative methods mentioned above.

Rubrene has been used widely in UCPL systems in both the solution and solid phase.[21–25] It is also an important model system for organic semiconductor crystal materials with high carrier mobilities, on the order of 1-20 cm^2 V^{-1} s^{-1}.[26] Orthorhombic rubrene single crystals can be grown using sublimation and physical vapor transport[27] and are usually needle-like with sizes ranging from millimeters to centimeters along the elongated crystal axis.[28] We recently showed that rubrene crystals undergo TTA-UCPL using radical ions embedded in the crystal as near-infrared sensitizers. In this chapter, I will explain the mechanism behind radical ion sensitized TTA-UCPL in rubrene crystals and show through our high-pressure results that TTA is quenched through compression of the crystal lattice, and that this also most likely quenches SF by monitoring the PL intensity of the rubrene.

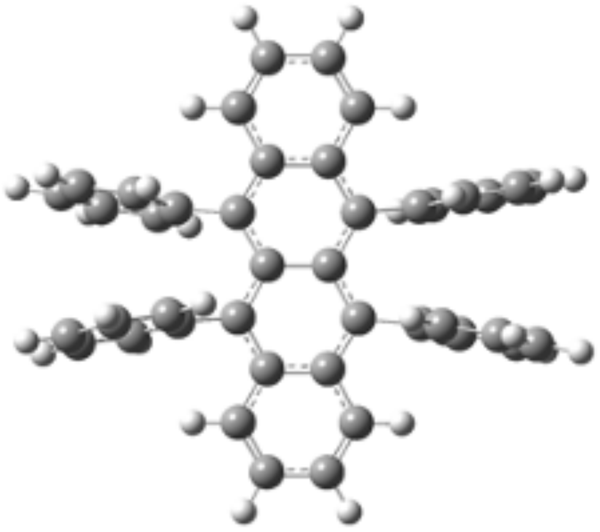

Figure 5.1: Rubrene (5,6,11,12-tetraphenyltetracene) molecular structure.

5.2 Rubrene Crystal Preparation

Crystals used for UCPL experiments were grown using a procedure for physical vapor transport (PVT) adapted from Zeng *et al.*[27] For each trial, 20 mg of rubrene powder (Sigma

Aldrich, sublimed grade, 99.99%) were loaded into a 40 cm long borosilicate glass tube, which was then placed in a tube furnace. One end of the furnace was connected to an argon tank and flow controller, and the other end was connected to a mineral oil bubbler to prevent back flow of atmospheric gases. The argon flow was set at 100 mL/min. The furnace was purged with argon through the bubbler for ten minutes to ensure that there was no remaining atmospheric oxygen. After purging, the furnace was set to ramp up the temperature to 290° C over the course of 3 hours. The temperature was then held at 290° C for 24 hours. After 24 hours, the temperature was allowed to cool back to room temperature before extracting the crystals. Crystals were generally needle-like (Figure 5.2) with lengths on the long axis between 1 mm and 10 mm, widths ca. 0.5 mm, and thickness ca. 5-10 μm.

Crystals were carefully collected from the borosilicate tube to avoid damaging them. To this end, an electrostatically charged glass rod inserted into the tube was used to collect the crystals by electrostatic attraction. Once crystals were removed from the tube, they were placed on either the outside of a modified quartz cuvette used for the UCPLE and temperature dependence experiments or on glass microscope slides for other UCPL experiments and characterization. Static charges in the crystals and on the glass or quartz surfaces were enough to securely hold the crystals to the quartz cuvette or glass slides. Crystals used in the diamond anvil cell (DAC) needed to be small enough to fit in the sample compartment in a stainless-steel gasket between the diamonds (see section 2.2 for details) which required carefully breaking off pieces of larger specimens before inserting them into the gasket hole.

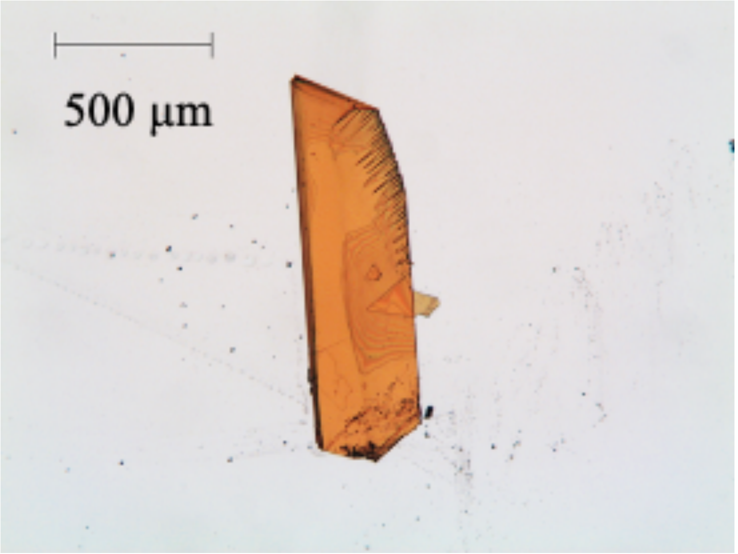

Figure 5.2: Microscope image of a rubrene crystal grown with PVT.

5.2.1 Characterization of Rubrene Crystals

5.2.1.1 UV-Vis Absorption

UV-vis absorption spectroscopy was performed on PVT grown rubrene crystals to confirm there were no impurity absorption features as well as estimate the thickness of the crystal (Figure 5.3).[27,29–31] We measured the absorbance in transmission mode using a Agilent Cary 5000 UV-Vis-NIR spectrophotometer by mounting a single rubrene needle-like crystal to a glass slide. The baseline spectrum was measured through the same glass slide, but next to where the crystal was mounted. To estimate the thickness, we followed the method by Fillard *et al.* for calculating film thickness in an absorbing material. This method takes advantage of the etalon effect between the first and second surfaces of the crystal producing interference fringes on the baseline of the spectrum (Figure 5.3, 575 nm – 700 nm).[31] Assuming a constant index of refraction for rubrene from 600 nm – 700nm of 2.0,[32] the spacing of fringes in our sample, gave us an estimated crystal thickness of 5.3 μm for this specimen.

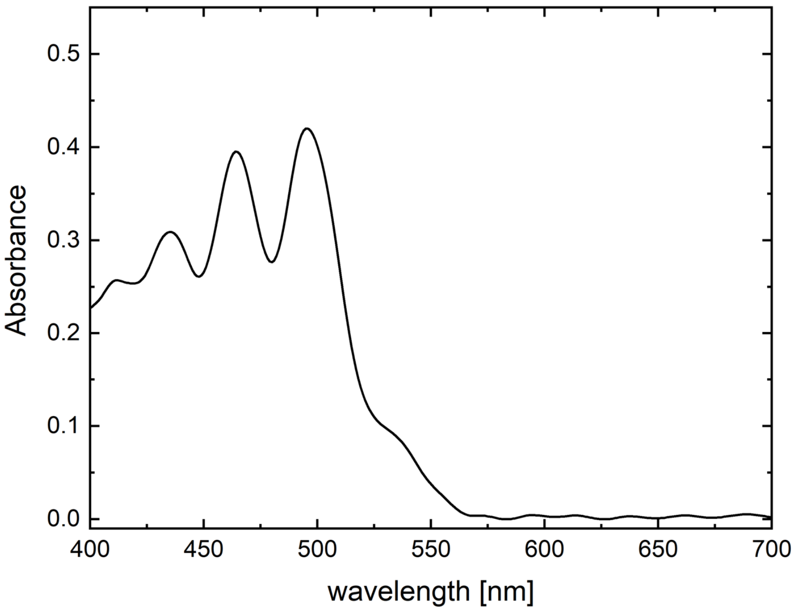

Figure 5.3: UV-vis absorption of a rubrene crystal grown from PVT. The oscillations on the baseline beyond 550 nm are interference fringes from an etalon effect between the first and second surfaces of the crystal.

5.2.1.2 Powder X-Ray Diffraction

We used powder x-ray diffraction (Bruker D8 Advance) on as-purchased rubrene powders and PVT grown crystals (Figure 5.4). In both cases, we placed a few powder grains or crystals onto a Si low-background holder (Bruker). Both powder and crystal samples have orthorhombic symmetry and space group Cmca (a = 26.8 Å, b = 7.2 Å, and c = 14.2 Å), consistent with the literature.[29] Some peaks are missing from the crystal sample because of imperfect randomization of the orientation of the crystals stacking on the sample holder, preventing access to all possible reflections in the diffractogram. Despite the missing peaks, the reflections present in the diffractogram are a clear match to the orthorhombic powder sample.

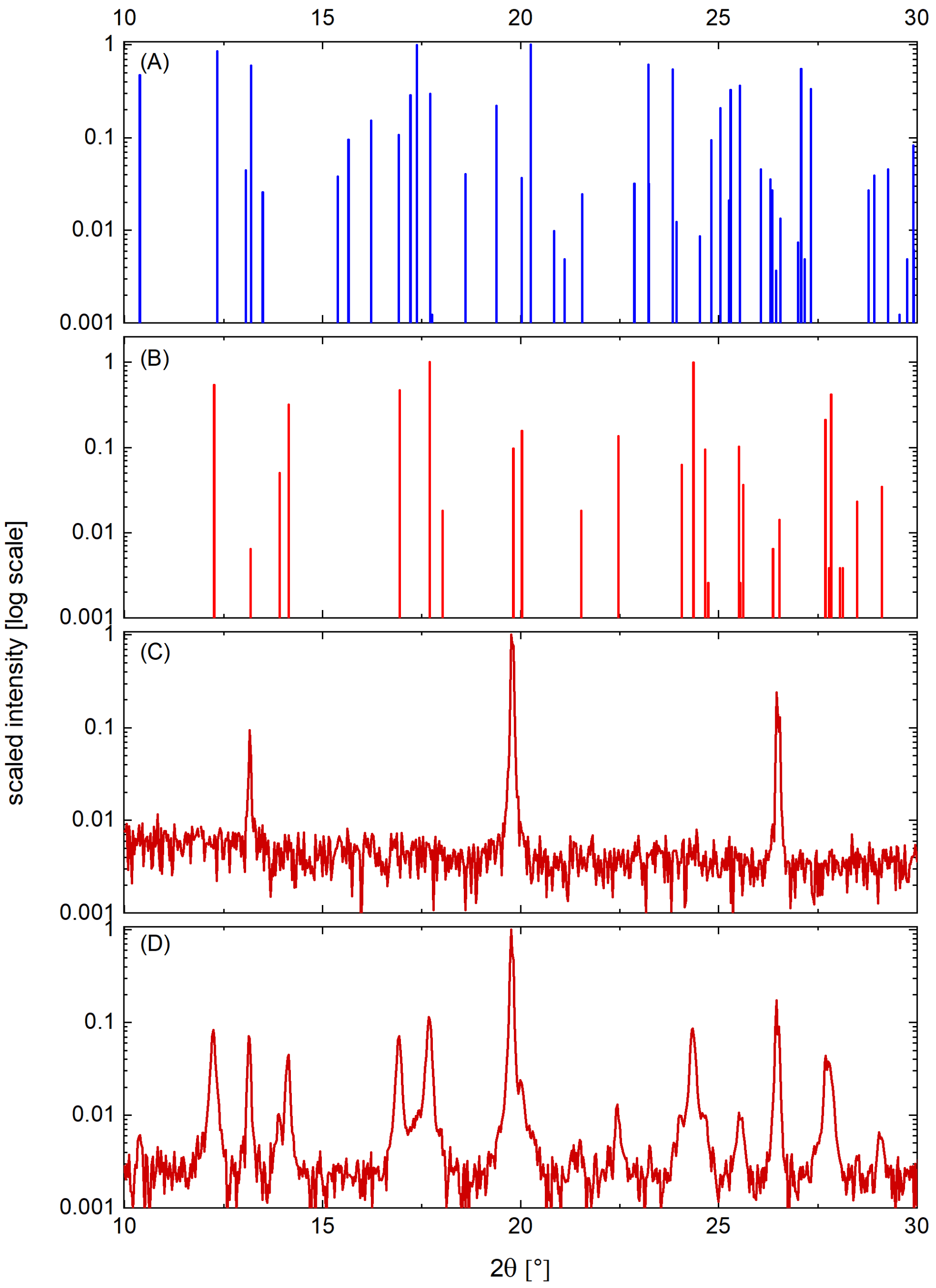

Figure 5.4: Powder XRD of rubrene samples. (A) calculated XRD pattern for triclinic rubrene, (B) calculated XRD pattern for orthorhombic rubrene, (C) crystals grown using PVT, and (D) rubrene powder. Intensity axes are on a logarithmic scale in order to see both the low and high intensity peaks.

5.3 Upconversion Photoluminescence in Rubrene

In general, TTA upconversion photoluminescence (UCPL) utilizes a combination of a "sensitizer species", absorbing longer wavelengths and transferring energy to an "emitter" species, which emits radiation at shorter wavelengths. The concept has been successfully demonstrated in solutions[10,11,23,24,33,34] as well as solid materials.[8,22,25,35–39] In order for TTA-UCPL to work in a particular system, the sensitizer and emitter combination must fulfil several requirements.[34] The sensitizer must be able to undergo efficient intersystem crossing into its triplet state once it has absorbed a photon, and many sensitizers therefore incorporate heavy metal atoms to increase spin orbit coupling.[40,41] Next, energy must transfer from the sensitizer to the triplet state of the emitter, requiring a sufficiently long lifetime of the sensitizer triplet state. The emitter triplet state (as an excited molecule in solution or as a triplet exciton in a crystal) must then diffuse in order to find and interact with another emitter in its triplet state. If the two triplets happen to migrate close enough, and are in the combined singlet state, ^{1}(TT), they can then combine energy through intermolecular electronic coupling to bring one molecule to the singlet excited state, S_1, leaving the other in the ground state, S_0. The excited singlet molecule can then fluoresce, emitting light with a higher energy than was originally absorbed by the sensitizer.

Interestingly, UCPL has been demonstrated in rubrene crystal and powder samples without any added sensitizing material.[8,21,25] Rubrene crystals are able to convert sufficiently intense near-infrared (NIR) light to visible light matching the fluorescence spectrum of solid rubrene.[8,21] One obvious explanation of this phenomenon would be that rubrene is undergoing two photon absorption (TPA, resonant or non-resonant), emitting from its singlet excited state, in which case the upconversion yield would vary with the square of the incident light intensity. However, using both cw and fs-pulsed radiation ca. 800 nm, a quartic dependence on the laser intensity at the lowest laser intensities is observed, implying a four-photon process rather than the quadratic signature of TPA.[8,25] This suggests the existence of a resonant intermediate state in the rubrene crystal which absorbs NIR light. This intermediate state then transfers energy to rubrene triplet excitons, which can then undergo TTA.

We used upconversion photoluminescence excitation (UCPLE) spectroscopy to measure the wavelength-dependent absorption characteristics of the species giving rise to the intermediate absorption in the NIR, using rubrene powders (Sigma-Aldrich, sublimed grade 99.99%) as well as single crystals grown using physical vapor transport.[27,29] For collecting UCPLE spectra, we scanned the frequency of an optical parametric oscillator pumped by a Nd:YAG laser (pulse duration 5-7 ns, see sections 2.4.1 - 2.4.4 for experimental details), and measured the intensity of the upconversion photoluminescence as a function of laser frequency (Figure 5.5).

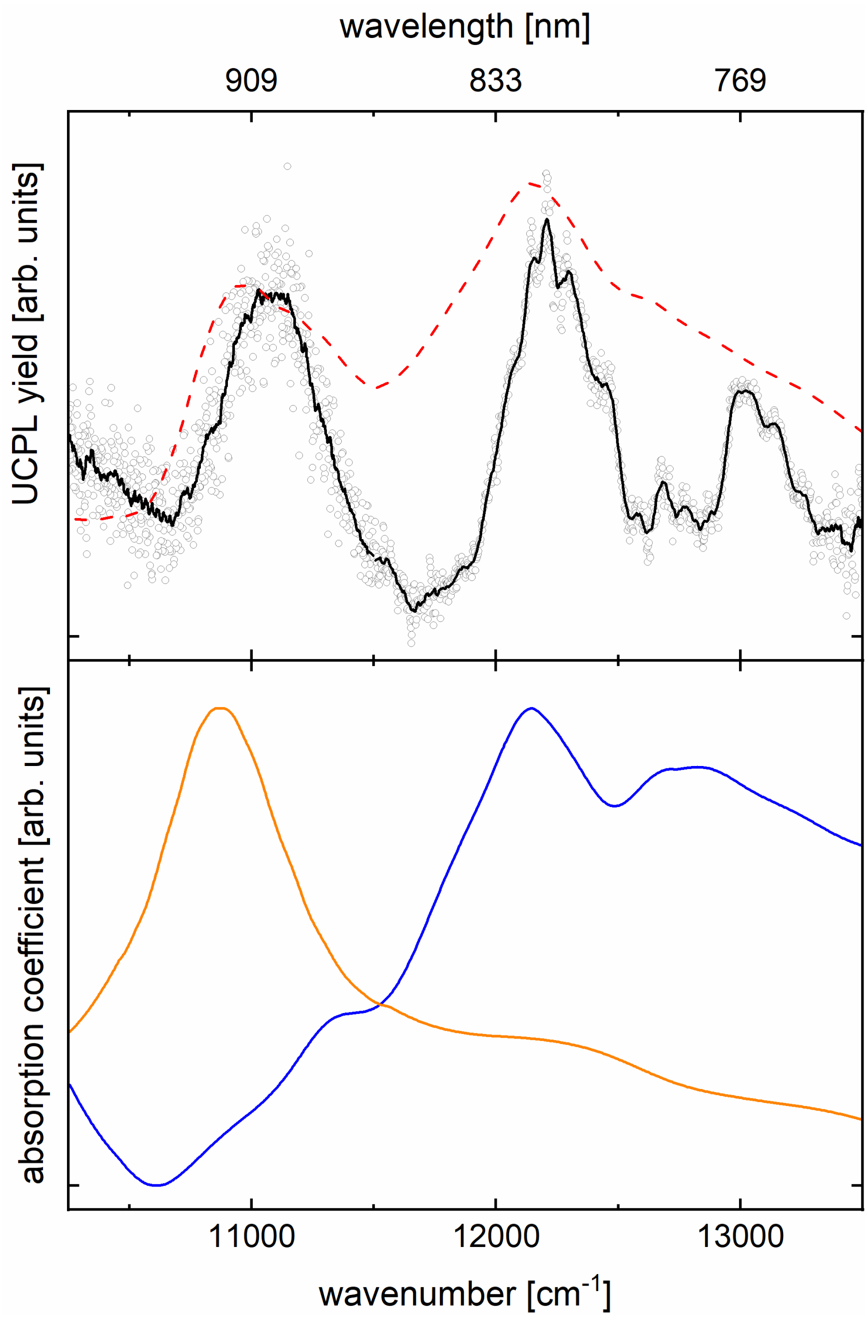

Figure 5.5: Bottom panel: solution absorption spectra of the rubrene radical cation (orange line) and radical anion (blue line); data in the lower panel were adapted from Tagawa and co-workers.[42] Top panel: UCPLE spectrum of crystalline rubrene, corrected for a four-photon process by dividing the raw UCPL intensity by the fluence to the fourth power. The open circles are individual data points, the black trace is a 20-point-smoothed curve to guide the eye. The red line is the arithmetic product of the absorption spectra of the radical ions shown in the lower panel.

We observed three distinct features in the NIR with enhanced upconverted photoluminescence, at ca. 11,100 cm^{-1} (900 nm), 12,200 cm^{-1} (820 nm), and 13,000 cm^{-1} (769 nm), respectively. The mechanism for electrochemiluminescence of rubrene in solution sheds light on the mechanism for UCPL in the crystals. It involves the recombination of a rubrene radical cation and a rubrene radical anion, producing an excited triplet and a ground state, both neutral molecules.[43–45] If the presence of both excited anions and cations is necessary to observe UCPL, then the UCPLE spectrum of rubrene should be proportional to the product of cation and anion absorption spectra:

$$Y_{UCPL}(\omega) \propto \alpha_{+}(\omega) \cdot \alpha_{-}(\omega) \tag{5.2}$$

where $Y_{UCPL}(\omega)$ is the upconversion yield, and $\alpha_{+}(\omega)$ and $\alpha_{-}(\omega)$ are the absorption coefficients of the rubrene radical cation and radical anion, respectively. Figure 5.5 shows a comparison of the experimental data and the product of the absorption spectra of the radical ions, taken from the work of Tagawa and coworkers.[42] The overall shape of the UCPLE spectrum agrees quite well with the product of the ion spectra, strongly suggesting that the excitation of both cations and anions is necessary for the observation of UCPL in rubrene. Deviations between our experimental results and the product of the ion absorption spectra are likely due to the fact that the ion absorption spectra were measured in solution whereas our measurements were performed on solid crystals.[42] These deviations are in all cases less than ca. 200 cm^{-1}, which is a reasonable expectations for shifts due to solvatochromic and crystal effects.

While the analogy to solution phase chemiluminescence is compelling, we must also rule out other possible mechanisms such as non-resonant TPA. Neutral rubrene does not absorb resonantly in this region, and there is disagreement in the literature over the non-resonant TPA spectrum of rubrene.[46,47] To test if TPA was responsible for the UCPL, we measured the UCPL intensity as a function of laser intensity with the laser frequency resonant with the observed peaks. If TPA were the origin of UCPL, the UCPL intensity would scale quadratically with the intensity. However, we found a quartic dependence on intensity, in agreement with previous work by Bardeen and coworkers (Figure 5.6).[8]

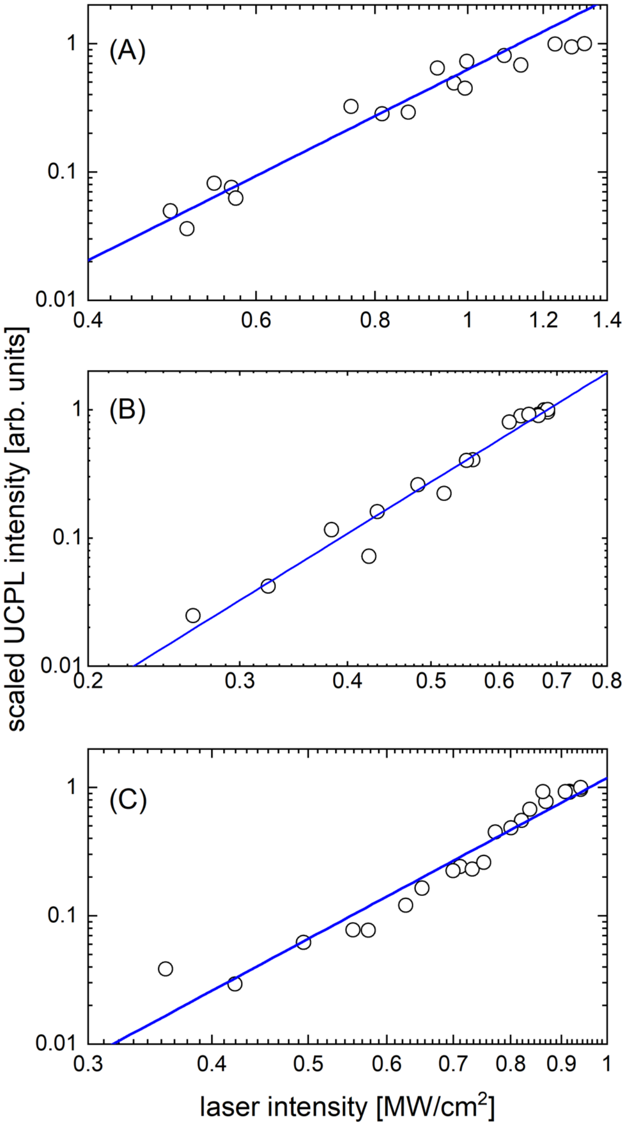

Figure 5.6: Dependence of the UCPL signal intensity on the excitation laser intensity at three excitation wavelengths. Signals were scaled to compare results from multiple samples. Open circles are raw data, the blue line is a fit of the laser intensity dependence to the experimental data. Laser excitation wavelength was set to 769 nm (A), 821 nm (B), and 890 nm (C) to be resonant with the observed transitions in the UCPLE spectrum. The exponents from the fit of the data are 4.16 ± 0.20 for 769 nm, 4.16 ± 0.22 for 821 nm, and 3.73 ± 0.30 for 890 nm excitation.

Rubrene powders used as purchased without further purification (at 99.99% nominal purity) qualitatively show the same UCPLE spectrum as twice sublimed rubrene crystal samples (Figure 5.7) with similar overall UCPL signal intensities, so the presence of a chemical impurity causing UCPL is very unlikely.

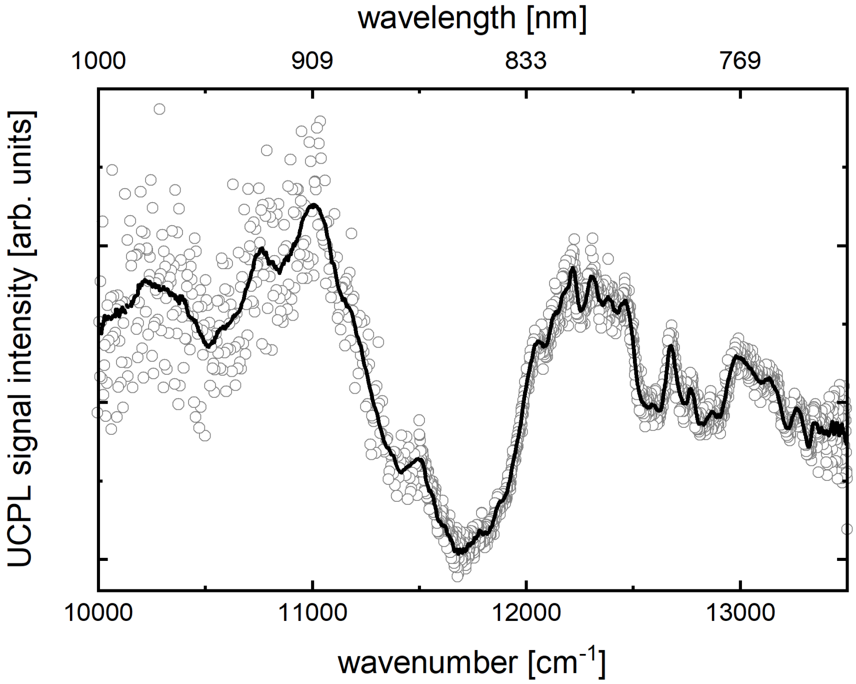

Figure 5.7: UCPLE spectrum of rubrene powder as received from Sigma Aldrich. Raw data points are plotted as open circles. The black trace is a 50-point-smoothed curve to guide the eye.

Rubrene can undergo reactive changes when exposed to light in the presence of oxygen, although the most recent literature shows that typical amounts of photooxidation products at the surface of rubrene crystals handled at normal conditions are rather small.[48] In addition, the conjugation in rubrene is broken in all common degradation products. As a result, one would expect that the degradation products have larger HOMO-LUMO gaps and $S_0 \rightarrow S_1$ transition energies that are higher than for rubrene itself, ruling out the possibility of a degradation product sensitizing TTA in the NIR.

Since recombination of radical anions and cations in solution results in the formation of two neutral molecules, one in the ground state and the other in the T_1 triplet state,[44,45] a mechanistic picture emerges that explains the shape of the UCPLE spectrum (Figure 5.5 and Figure 5.7) in solid rubrene, as well as the quartic intensity dependence of the process (Figure 5.6). NIR radiation is not energetic enough to produce charged radical ion species in rubrene, so the charged species must already exist in the crystal prior to excitation.[22] However, this begs the question as to why the observed UCPL process in solid rubrene requires excitation, since electrogenerated chemiluminescence in rubrene solutions through the formation of a triplet is observed without prior photoexcitation.[44,45]

In solution, cationic and anionic species can freely migrate to find one another, recombining and forming triplet excited molecules. If this were the case in solid rubrene, the charged species would rapidly recombine, leaving little to none left for UCPL. However, if the charged species are immobilized within the crystal lattice at surface sites or defects, excitation may be necessary to overcome the trap barrier, allowing diffusion through the crystal. Therefore, the starting species for the observed UCPL process may be localized, immobile rubrene anions and cations. The charged nature of the rubrene anions and cations likely distort the local crystal lattice, which can be thought of as charged defect sites. After excitation, these charged sites become mobile, leading to the formation of charge transfer (CT) polarons,[49–51] enabling the charges to move through the crystal after excitation. Although the lifetimes of such CT polarons in crystalline rubrene have not been measured to our knowledge, these relaxation processes occur by losing energy to phonon excitations as the mobile charge distorts the lattice as it moves. If a similar time scale as relaxation of the $S_1 \rightarrow S_0$ in neutral rubrene, relaxation of the charged species may happen on the 100 ps – 100 ns time scale.[7] The cation and the anion are both doublets so when they combine in a spin allowed process, they can produce a triplet exciton (assuming the same spin on the cation and the anion) or a singlet exciton (assuming opposite spin on the cation and anion) as well as a neutral ground state molecule (Figure 5.8).[43,45] Once there is a sufficient population of triplet excitons, they can recombine via TTA, producing a rubrene molecule in the S_1 state and another in the neutral ground state.

This proposed process has many opportunities for loss along the way, which is apparent in the low yield of UCPL. For example, the CT polaron could non-radiatively relax before it finds a partner of opposite charge, immobilizing the charge once again. The triplet excitons may relax through a process other than TTA, which will not provide an excited singlet. Or, since SF has a faster rate than fluorescence in rubrene, the produced excited singlet may share its excitation with a neighboring molecule, remaking two triplets.[8,9,52] There are of course even more potential loss mechanisms than what was mentioned here.

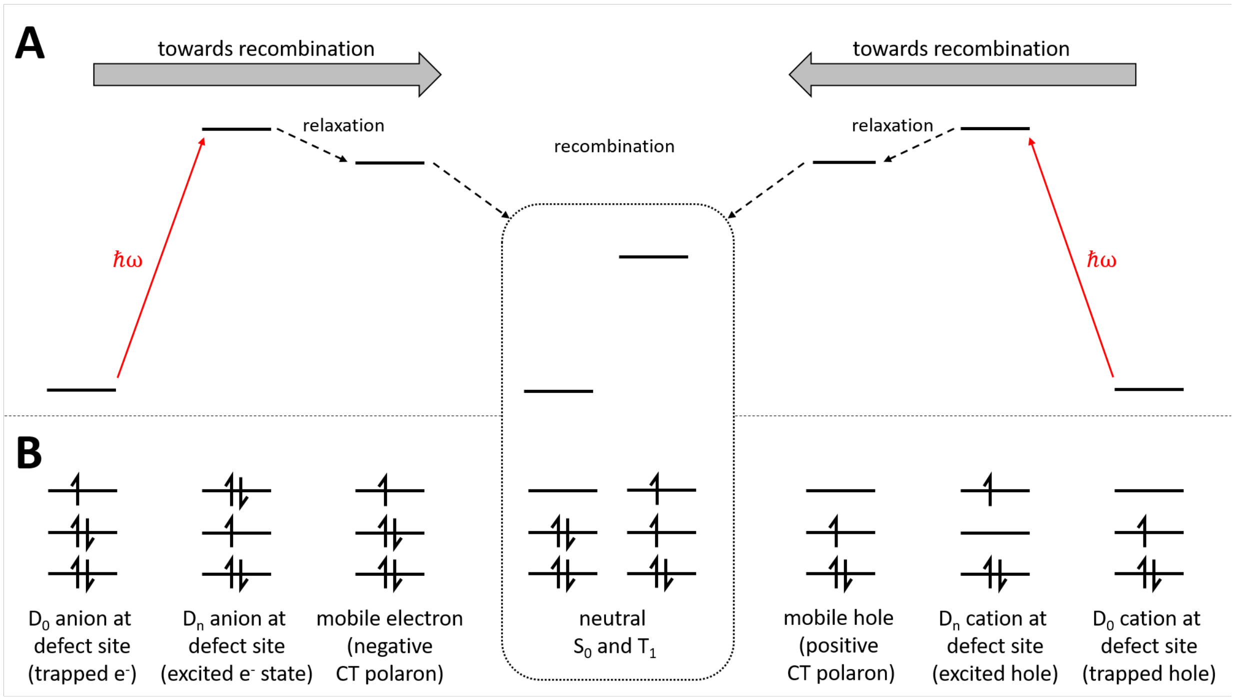

Figure 5.8: (A) Qualitative reaction diagram showing the recombination of electrons and holes in the proposed mechanism of UCPL from the excitation of trapped electrons (left) and holes (right)

through relaxation processes in the crystal to the generation of a triplet exciton (center). (B) Schematic electron configurations in the reaction mechanism. Ground and excited state electron configurations of rubrene ions have been determined using TDDFT (see Supporting Information).

A simple kinetic model which takes into account as much of the known information about each step of the proposed mechanism as possible should corroborate the quartic dependence of the excitation intensity if this mechanism is indeed correct. The excited mobile negative and positive charge carriers, N_e and N_h, are governed by

$$\frac{dN_e}{dt} = \Phi(\mathrm{t})N_{e0}\sigma_{CTe} - k_R N_e N_h - k_L N_e \tag{5.3}$$

and $$\frac{dN_h}{dt} = \Phi(t)N_{h0}\sigma_{CTh} - k_R N_e N_h - k_L N_h \tag{5.4}$$

where N_{e0} and N_{h0} are the initial densities of the trapped electrons and holes, $\Phi(\mathrm{t})$ is the photon fluence (in photons per cm^2 and s, the time dependence encodes the laser pulse duration), and σ_{CTe} and σ_{CTh} are the mobile charge carrier formation cross sections. The parameter k_R is the charge recombination rate constant, and k_L is the rate constant for loss processes, depleting the mobile charge carriers (set to be the same for negative and positive carriers for simplicity). The density of triplets, N_T, is described by

$$\frac{dN_T}{dt} = k_R N_e N_h - k_A N_T^2 + 2k_{SF} N_S - k_Q N_T \tag{5.5}$$

where N_S is the density of singlet excitons formed by TTA, k_A is the TTA rate constant, k_{SF} the singlet fission rate constant, and k_Q a triplet quenching rate constant. Finally, the singlet population is governed by

$$\frac{dN_S}{dt} = k_A N_T^2 - k_{PL} N_S - k_{SF} N_S \qquad 5.6$$

where k_{PL} is the PL rate constant. Several of the individual steps in the proposed mechanism have been studied, and therefore we can find several parameters of the proposed model from the literature and are summarized in Table 5.1.[8] There are of course unknown parameters in the proposed model and others that could be added to our model to account for more loss mechanisms such as triplet-triplet quenching. The unknown parameters in that were included in the current model are σ_{CTe}, σ_{CTh}, k_R, and k_L. A wide range of these unknown parameters exists for which the model reproduces the experimentally observed quartic intensity dependence of UCPL and are tabulated in Table 5.1. Although the model is relatively simple, the match with our experimental data supports the proposed mechanism.

Table 5.1: Parameters used in the kinetic model

$\boldsymbol{\sigma_{CTe}}$, $\boldsymbol{\sigma_{CTh}}$ (cm^2)[(a)]	$\boldsymbol{k_R}$ ($cm^3\ s^{-1}$)[(a)]	$\boldsymbol{k_L}$ (s^{-1})[(a)]	$\boldsymbol{k_A}$ ($cm^3\ s^{-1}$)[(b)]	$\boldsymbol{k_{SF}}$ (s^{-1})[(b)]	$\boldsymbol{k_Q}$ (s^{-1})[(b)]	$\boldsymbol{k_{PL}}$ (s^{-1})[(b)]
$10^{-21} – 10^{-15}$	$10^{-15} – 10^{-9}$	$10^{5} – 10^{6}$	10^{-12}	$5 \cdot 10^{10}$	$1.67 \cdot 10^{4}$	$6.25 \cdot 10^{7}$

(a) Range of parameters tested in the present work that produce quartic intensity dependence.

(b) Values taken from Table 2 in ref. [8].

The initial source of the localized charges is not entirely clear, but they could originate from charges that tunnel into the rubrene from surrounding surfaces, such as the borosilicate tube the crystals were made in, or from the surface of the cuvette that they were mounted to for measurements. What is clear is that the proposed mechanism will result in a depletion of the initially localized charge carriers over time as they are lost due to recombination. This is consistent with the observation of significant photobleaching (Figure 5.9) of the UCPL. This was also observed by Nienhaus and coworkers in other processes that involve intrinsic charge carriers in rubrene and tied to surface effects.[22] Irradiation of rubrene in paraffin oil with a pulsed excitation source operating at 20 Hz and a time-averaged intensity of 50 mW/cm^2 results in the UCPL signal decaying, reaching 45% of its initial value after ca. 450 s (7.5 minutes) and only slightly decreasing from this value over the course of hours (Figure 5.9). In paraffin oil, the UCPL signal does not recover when left in the dark, allowing to study the effect of pressure on the UCPL intensity under high pressure when using paraffin oil as a pressure transmitting medium. This is an important detail because our pressure experiments require a twenty-minute equilibration time (see section 2.2 for details) between measurements, so there cannot be significant changes to the UCPL intensity before and after the equilibration period.

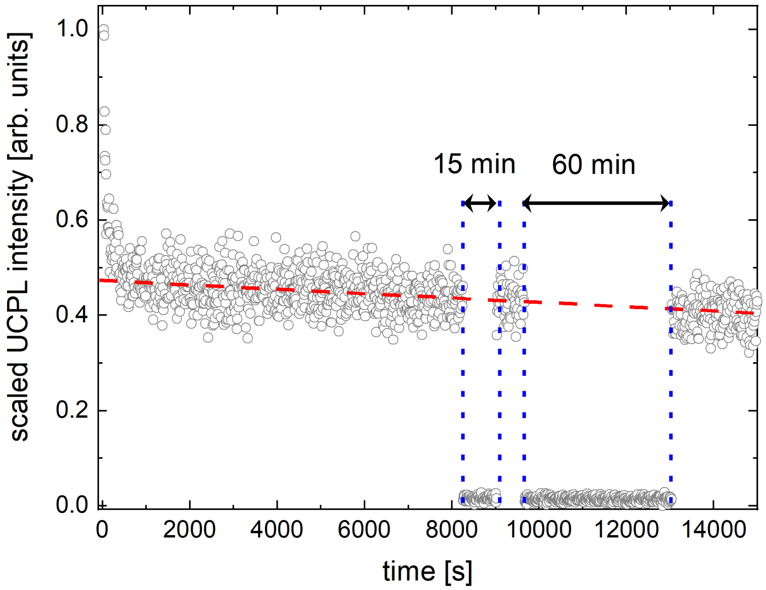

Figure 5.9: Bleaching of UCPL under constant irradiation of 765 nm pulsed radiation operating at 20 Hz and an average power of 50 mW/cm^2. The red dashed line guides the eye to the slow decay of intensity over the course of hours. The vertical blue dashed lines indicate when the laser was blocked from irradiating the sample.

5.4 Pressure-Response of the Intermediate State

We measured the UCPLE spectrum from 12,200 cm^{-1} (820 nm) to 13,600 cm^{-1} (735 nm) at ambient pressure in the diamond anvil cell (DAC) as well as at an elevated pressure of 1.65 GPa (Figure 5.10). The signal to noise is much lower for these measurements than the previous UCPLE spectra shown due to the significant decrease in rubrene material that can be used in the DAC (see section 2.2 and 2.4.3 - 2.4.4 for experimental details). Under pressure the UCPLE feature ca. 765 nm blue shifts and broadens. Once we knew roughly how the absorption spectra of the cation and anions in the rubrene sample evolve under pressure, we then measured how the intensity of the PL and UCPL spectra change as a function of pressure, as a means to indirectly measure the efficiency of SF and TTA as a function of pressure.

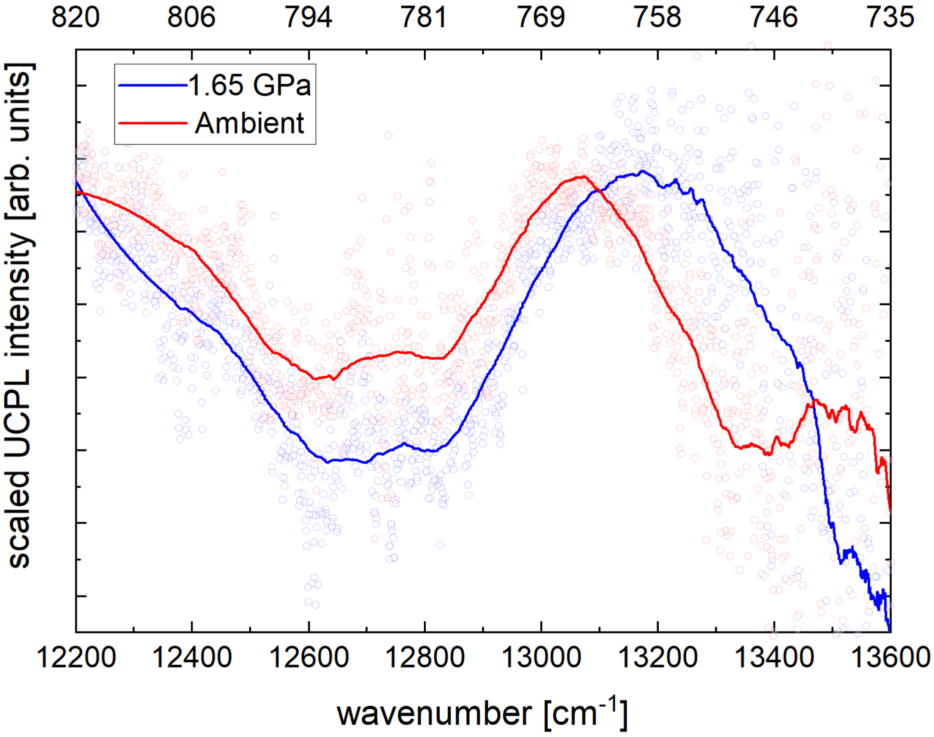

Figure 5.10: UCPLE spectra of rubrene crystals in the DAC. Spectra were recorded at ambient (red data points) and 1.65 GPa (blue data points). The red and blue traces are 300-point-smoothed curves to guide the eye.

5.5 Pressure Quenching of Photoluminescence and Upconversion Photoluminescence

We measured the UCPL and PL intensity as a function of pressure as a way to qualitatively probe changes to the intermolecular coupling due to decreased intermolecular distances of neighboring rubrene molecules in the crystal. The rubrene samples were excited with 406 nm CW laser light and the resulting PL spectra were recorded on a fiber optic spectrometer (see section 2.4.4 for experimental details). For the UCPL spectra, the rubrene was excited with 765 nm light from output of the OPO and the resulting UCPL spectra were recorded on a fiber optic spectrometer (see section 2.4.4 for experimental details). The NIR excitation wavelength was chosen because it remains resonant with the UCPLE feature in Figure 5.10 throughout a large portion of the pressure range tested here.

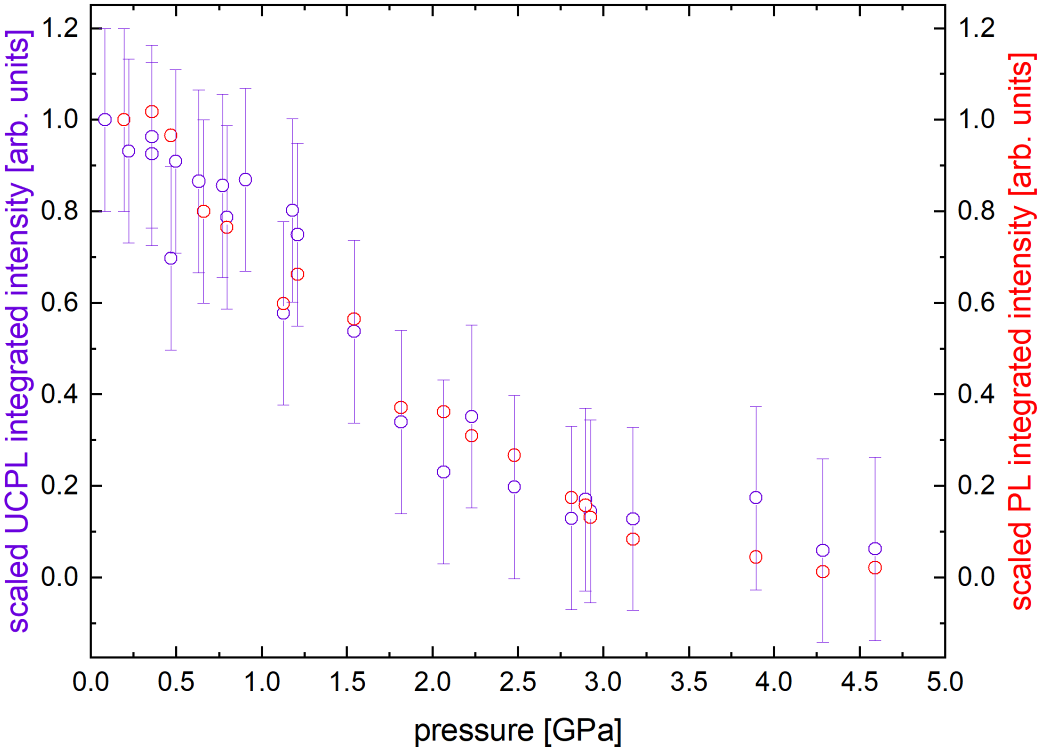

Figure 5.11: UCPL (purple) and PL (red) quenching under pressure. The relatively large error bars on the UCPL data come fluctuations in the intensity of the output of the OPO, which has a large effect on the UCPL, due to the quartic dependence.

Figure 5.11 shows the integrated intensities of the UCPL and PL spectra as a function of pressure. Not only do both UCPL and PL experience quenching, but when scaled to have the same initial integrated intensity, the two behaviors are nearly identical. This may seem curious, as the UCPL goes through excitation of radical ions, energy transfer to triplet excitons, and then TTA to finally fluoresce from the S_1 state in rubrene, while intrinsic PL only requires an excitation from the ground state to S_1. However, in rubrene crystals, only a fraction of 10^{-3} of an initially excited singlet exciton will undergo fluorescence, due to very efficient SF.[9] The triplets generated from SF may recombine, reforming an S_1 and S_0 state on neighboring molecules, which can then undergo fluorescence. This process of fission and fusion can repeat multiple times and accounts for nearly all the PL observed from crystalline rubrene.[9] Given this fact, it is not surprising that the UCPL and PL have nearly the identical response to changes in the crystal structure induced by pressure.

The increase in the packing density and intermolecular interactions is to blame for the quenching of the UCPL and PL. Due to the C_{2h} symmetry of each rubrene molecule, if they were stacked perfectly so that the tetracene backbones were face-to-face, the intermolecular electronic coupling constant between the LUMO of one molecule and the HOMO of a neighboring molecule, which is responsible for SF, would be exactly zero.[5] In the orthorhombic crystal structure, the molecules are not perfectly face to face, but the overlap of out of phase *p*-orbitals still exist (Figure 5.12). The HOMO and the LUMO interactions are not the only orbitals responsible for the coupling that produces SF, but understanding how they interact gives a picture of how pressure will enhance SF.

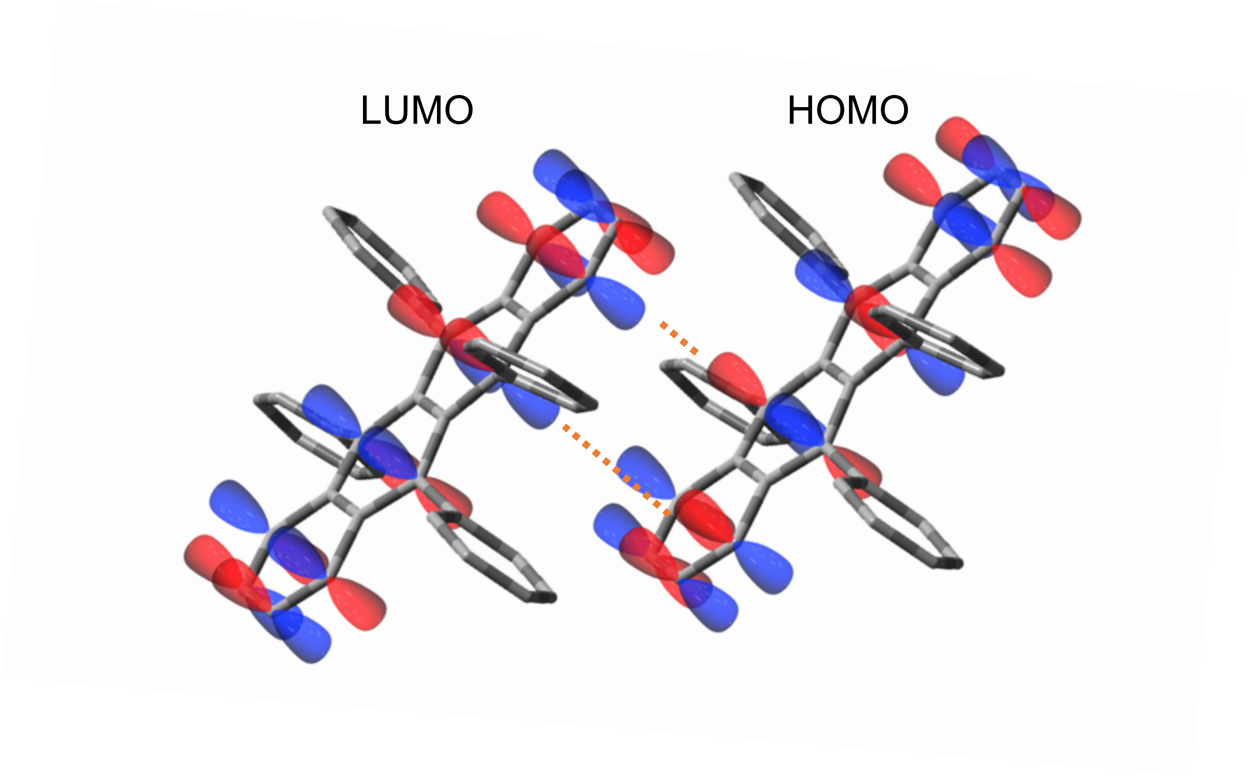

Figure 5.12: Schematic drawing of two rubrene molecules in an orthorhombic crystal. The molecule on the left shows the *p*-orbitals of the LUMO, while the molecule on the right shows the *p*-orbitals of the HOMO. Decreasing the distance between neighboring molecules enhances the orbital overlap, increasing the intermolecular electronic coupling.

The only reason SF is possible in rubrene crystals is because the orthorhombic crystal structure has rubrene molecules in a position such that the tetracene backbones are slipped relative to one another and kept far apart by the phenyl groups. When pressure is applied, the molecules are forced closer together increasing the orbital interactions, which may increase the overall intermolecular electronic coupling. As the intermolecular electronic coupling increases, the rates for both SF and TTA would increase as well. Since SF is in competition with fluorescence, an increase in the rate of SF would manifest itself as a decrease in PL intensity as a function of pressure, which is what we have observed here (Figure 5.11).[3] UCPL relies on TTA in order to proceed, so on may ask why do we see a decrease in the UCPL signal as a function of pressure as well? Ultimately, UCPL must reach the S_1 state before emitting light. If the SF rate has increased, the S_1 state prepared through TTA will be more likely to internally convert back to the ^{1}(TT) state, quenching the UCPL signal.

In order to understand exactly what the applied pressure is doing to the crystal lattice, and therefore what is causing the enhancement of SF, we would need to do *in situ* XRD of rubrene under pressure to determine exactly how the crystal (and possibly the individual rubrene molecules) deform. The quenching of the PL and UCPL signals decrease linearly until a critical pressure where the intensity does not drop further with increasing pressure. At this pressure, it appears that further pressure does not increase the SF rate any further. It is not clear from our data on its own whether or not the SF rate remains constant or begins to fall. At these high pressures, there are likely more contributions to PL and UCPL quenching besides the SF rate.

5.6 Conclusion

In conclusion, we propose that the UCPL observed in rubrene crystals and powders is due to the excitation of interband states that correspond to excited states of radical cations and radical anions in the crystal. We measured the rubrene UCPLE spectrum in crystalline samples as well as powders and found that the measured UCPLE features in the NIR are in good agreement with a product of the experimental absorption spectra of the two radical ion species. Excitation of localized, molecular charge carriers results in mobile charge carriers, which can recombine to produce triplet excitons. These triplet excitons can then undergo TTA, resulting in photoluminescence. This model accounts for the features in the UCPLE spectrum, the quartic intensity dependence of the UCPL signal, and the photobleaching of UCPL. Under pressure, the increase in the orbital interactions between neighboring molecules quenches the UCPL and PL signal. This is likely due to an increase in the SF rate, which competes with fluorescence. This is a potentially important finding, as increasing the rate of SF has the potential to improve photovoltaic devices.

5.7 References

(1) Smith, M. B.; Michl, J. Singlet Fission. *Chem. Rev.* **2010**, *110* (11), 6891–6936.

(2) Arias, D. H.; Ryerson, J. L.; Cook, J. D.; Damrauer, N. H.; Johnson, J. C. Polymorphism Influences Singlet Fission Rates in Tetracene Thin Films. *Chem. Sci.* **2016**, *7* (2), 1185–1191.

(3) Grumstrup, E. M.; Johnson, J. C.; Damrauer, N. H. Enhanced Triplet Formation in Polycrystalline Tetracene Films by Femtosecond Optical-Pulse Shaping. *Phys. Rev. Lett.* **2010**, *105* (25), 257403.

(4) Pandey, A. K. Highly Efficient Spin-Conversion Effect Leading to Energy up-Converted Electroluminescence in Singlet Fission Photovoltaics. *Sci. Rep.* **2015**, *5*, 1–6.

(5) Miyata, K.; Kurashige, Y.; Watanabe, K.; Sugimoto, T.; Takahashi, S.; Tanaka, S.; Takeya, J.; Yanai, T.; Matsumoto, Y. Coherent Singlet Fission Activated by Symmetry Breaking. *Nat. Chem.* **2017**, *9* (10), 983–989.

(6) Gray, V.; Dzebo, D.; Abrahamsson, M.; Albinsson, B.; Moth-Poulsen, K. Triplet-Triplet Annihilation Photon-Upconversion: Towards Solar Energy Applications. *Phys. Chem. Chem. Phys.* **2014**, *16* (22), 10345–10352.

(7) Ma, L.; Zhang, K.; Kloc, C.; Sun, H.; Michel-Beyerle, M. E.; Gurzadyan, G. G. Singlet Fission in Rubrene Single Crystal: Direct Observation by Femtosecond Pump–Probe Spectroscopy. *Phys. Chem. Chem. Phys.* **2012**, *14* (23), 8307–8312.

(8) Cruz, C. D.; Choi, H. H.; Podzorov, V.; Chronister, E. L.; Bardeen, C. J. Photon Upconversion in Crystalline Rubrene: Resonant Enhancement by an Interband State. *J.*

Phys. Chem. C **2018**, *122* (31), 17632–17642.

(9) Ma, L.; Zhang, K.; Kloc, C.; Sun, H.; Soci, C.; Michel-Beyerle, M. E.; Gurzadyan, G. G. Fluorescence from Rubrene Single Crystals: Interplay of Singlet Fission and Energy Trapping. *Phys. Rev. B* **2013**, *87* (20), 201203.

(10) Gertsen, A. S.; Koerstz, M.; Mikkelsen, K. V. Benchmarking Triplet-Triplet Annihilation Photon Upconversion Schemes. *Phys. Chem. Chem. Phys.* **2018**, *20* (17), 12182–12192.

(11) Cheng, Y. Y.; Fückel, B.; Khoury, T.; Clady, R. G. C. R.; Tayebjee, M. J. Y.; Ekins-Daukes, N. J.; Crossley, M. J.; Schmidt, T. W. Kinetic Analysis of Photochemical Upconversion by Triplet-Triplet Annihilation: Beyond Any Spin Statistical Limit. *J. Phys. Chem. Lett.* **2010**, *1* (12), 1795–1799.

(12) Parker, C. A.; Bowen, E. J. Sensitized P-Type Delayed Fluorescence. *Proc. R. Soc. London. Ser. A. Math. Phys. Sci.* **1963**, *276* (1364), 125–135.

(13) Gray, V.; Moth-Poulsen, K.; Albinsson, B.; Abrahamsson, M. Towards Efficient Solid-State Triplet–Triplet Annihilation Based Photon Upconversion: Supramolecular, Macromolecular and Self-Assembled Systems. *Coord. Chem. Rev.* **2018**, *362*, 54–71.

(14) Tayebjee, M. J. Y.; McCamey, D. R.; Schmidt, T. W. Beyond Shockley–Queisser: Molecular Approaches to High-Efficiency Photovoltaics. *J. Phys. Chem. Lett.* **2015**, *6* (12), 2367–2378.

(15) Nattestad, A.; Cheng, Y. Y.; MacQueen, R. W.; Schulze, T. F.; Thompson, F. W.; Mozer, A. J.; Fückel, B.; Khoury, T.; Crossley, M. J.; Lips, K.; Wallace, G. G.; Schmidt, T. W. Dye-Sensitized Solar Cell with Integrated Triplet–Triplet Annihilation Upconversion System. *J. Phys. Chem. Lett.* **2013**, *4* (12), 2073–2078.

(16) Chen, S.; Weitemier, A. Z.; Zeng, X.; He, L.; Wang, X.; Tao, Y.; Huang, A. J. Y.;

Hashimotodani, Y.; Kano, M.; Iwasaki, H.; Parajuli, L. K.; Okabe, S.; Teh, D. B. L.; All, A. H.; Tsutsui-Kimura, I.; Tanaka, K. F.; Liu, X.; McHugh, T. J. Near-Infrared Deep Brain Stimulation via Upconversion Nanoparticle–Mediated Optogenetics. *Science (80-.).* **2018**, *359* (6376), 679–684.

(17) Ravetz, B. D.; Pun, A. B.; Churchill, E. M.; Congreve, D. N.; Rovis, T.; Campos, L. M. Photoredox Catalysis Using Infrared Light via Triplet Fusion Upconversion. *Nature* **2019**, *565* (7739), 343–346.

(18) Alguire, E. C.; Subotnik, J. E.; Damrauer, N. H. Exploring Non-Condon Effects in a Covalent Tetracene Dimer: How Important Are Vibrations in Determining the Electronic Coupling for Singlet Fission? *J. Phys. Chem. A* **2015**, *119* (2), 299–311.

(19) Damrauer, N. H.; Snyder, J. L. Symmetry-Directed Control of Electronic Coupling for Singlet Fission in Covalent Bis–Acene Dimers. *J. Phys. Chem. Lett.* **2015**, *6* (22), 4456–4462.

(20) Dillon, R. J.; Piland, G. B.; Bardeen, C. J. Different Rates of Singlet Fission in Monoclinic versus Orthorhombic Crystal Forms of Diphenylhexatriene. *J. Am. Chem. Soc.* **2013**, *135* (46), 17278–17281.

(21) Liu, H.; Yan, F.; Li, W.; Lee, C. S.; Chu, B.; Chen, Y.; Li, X.; Han, L.; Su, Z.; Zhu, J.; Kong, X.; Zhang, L.; Luo, Y. Up-Conversion Luminescence of Crystalline Rubrene without Any Sensitizers. *Org. Electron.* **2010**, *11* (5), 946–950.

(22) Wieghold, S.; Nienhaus, L. Precharging Photon Upconversion: Interfacial Interactions in Solution-Processed Perovskite Upconversion Devices. *J. Phys. Chem. Lett.* **2020**, *11* (3), 601–607.

(23) Schulze, T. F.; Schmidt, T. W. Photochemical Upconversion: Present Status and Prospects

for Its Application to Solar Energy Conversion. *Energy Environ. Sci.* **2015**, *8* (1), 103–125.

(24) Islangulov, R. R.; Kozlov, D. V.; Castellano, F. N. Low Power Upconversion Using MLCT Sensitizers. *Chem. Commun.* **2005**, *1* (30), 3776–3778.

(25) Beimborn, J. C.; Zagorec-Marks, W.; Weber, J. M. Spectroscopy of Resonant Intermediate States for Triplet–Triplet Annihilation Upconversion in Crystalline Rubrene: Radical Ions as Sensitizers. *J. Phys. Chem. Lett.* **2020**, *11* (17), 7212–7217.

(26) Choi, H. H.; Cho, K.; Frisbie, C. D.; Sirringhaus, H.; Podzorov, V. Critical Assessment of Charge Mobility Extraction in FETs. *Nat. Mater.* **2018**, *17* (1), 2–7.

(27) Zeng, X.; Zhang, D.; Duan, L.; Wang, L.; Dong, G.; Qiu, Y. Morphology and Fluorescence Spectra of Rubrene Single Crystals Grown by Physical Vapor Transport. *Appl. Surf. Sci.* **2007**, *253* (14), 6047–6051.

(28) Irkhin, P.; Biaggio, I. Direct Imaging of Anisotropic Exciton Diffusion and Triplet Diffusion Length in Rubrene Single Crystals. *Phys. Rev. Lett.* **2011**, *107* (1), 1–4.

(29) Jurchescu, O. D.; Meetsma, A.; Palstra, T. T. M. Low-Temperature Structure of Rubrene Single Crystals Grown by Vapor Transport. *Acta Crystallogr. Sect. B* **2006**, *62* (2), 330–334.

(30) Chen, Y.; Lee, B.; Fu, D.; Podzorov, V. The Origin of a 650 Nm Photoluminescence Band in Rubrene. *Adv. Mater.* **2011**, *23* (45), 5370–5375.

(31) Manifacier, J. C.; Gasiot, J.; Fillard, J. P. A Simple Method for the Determination of the Optical Constants n, k and the Thickness of a Weakly Absorbing Thin Film. *J. Phys. E.* **1976**, *9* (11), 1002–1004.

(32) Sugimoto, S.; Fukunishi, Y.; Fukaya, Y.; Yamao, T.; Hotta, S. Refractive Index Dispersion and Anisotropic Group Refractive Indices of Rubrene Crystals. *Trans. Mater. Res. Soc.*

Japan **2013**, *38* (2), 301–304.

(33) Schmidt, T. W.; Castellano, F. N. Photochemical Upconversion: The Primacy of Kinetics. *J. Phys. Chem. Lett.* **2014**, *5* (22), 4062–4072.

(34) Singh-Rachford, T. N.; Castellano, F. N. Photon Upconversion Based on Sensitized Triplet-Triplet Annihilation. *Coord. Chem. Rev.* **2010**, *254* (21–22), 2560–2573.

(35) Nienhaus, L.; Correa-Baena, J. P.; Wieghold, S.; Einzinger, M.; Lin, T. A.; Shulenberger, K. E.; Klein, N. D.; Wu, M.; Bulović, V.; Buonassisi, T.; Baldo, M. A.; Bawendi, M. G. Triplet-Sensitization by Lead Halide Perovskite Thin Films for near-Infrared-to-Visible Upconversion. *ACS Energy Lett.* **2019**, *4* (4), 888–895.

(36) Nienhaus, L.; Wu, M.; Geva, N.; Shepherd, J. J.; Wilson, M. W. B.; Bulović, V.; Van Voorhis, T.; Baldo, M. A.; Bawendi, M. G. Speed Limit for Triplet-Exciton Transfer in Solid-State PbS Nanocrystal-Sensitized Photon Upconversion. *ACS Nano* **2017**, *11* (8), 7848–7857.

(37) Wieghold, S.; Bieber, A. S.; Vanorman, Z. A.; Nienhaus, L. Influence of Triplet Diffusion on Lead Halide Perovskite-Sensitized Solid-State Upconversion. *J. Phys. Chem. Lett.* **2019**, *10* (13), 3806–3811.

(38) Geva, N.; Nienhaus, L.; Wu, M.; Bulović, V.; Baldo, M. A.; Van Voorhis, T.; Bawendi, M. G. A Heterogeneous Kinetics Model for Triplet Exciton Transfer in Solid-State Upconversion. *J. Phys. Chem. Lett.* **2019**, *10* (11), 3147–3152.

(39) Xia, P.; Raulerson, E. K.; Coleman, D.; Gerke, C. S.; Mangolini, L.; Tang, M. L.; Roberts, S. T. Achieving Spin-Triplet Exciton Transfer between Silicon and Molecular Acceptors for Photon Upconversion. *Nat. Chem.* **2020**, *12* (2), 137–144.

(40) Kiseleva, N.; Nazari, P.; Dee, C.; Busko, D.; Richards, B. S.; Seitz, M.; Howard, I. A.;

Turshatov, A. Lanthanide Sensitizers for Large Anti-Stokes Shift Near-Infrared-to-Visible Triplet–Triplet Annihilation Photon Upconversion. *J. Phys. Chem. Lett.* **2020**, *11* (7), 2477–2481.

(41) Bender, J. A.; Raulerson, E. K.; Li, X.; Goldzak, T.; Xia, P.; Van Voorhis, T.; Tang, M. L.; Roberts, S. T. Surface States Mediate Triplet Energy Transfer in Nanocrystal–Acene Composite Systems. *J. Am. Chem. Soc.* **2018**, *140* (24), 7543–7553.

(42) Saeki, A.; Seki, S.; Takenobu, T.; Iwasa, Y.; Tagawa, S. Mobility and Dynamics of Charge Carriers in Rubrene Single Crystals Studied by Flash-Photolysis Microwave Conductivity and Optical Spectroscopy. *Adv. Mater.* **2008**, *20* (5), 920–923.

(43) Hercules, D. M.; Lansbury, R. C.; Roe, D. K. Chemiluminescence from the Reduction of Rubrene Radical Cations. *J. Am. Chem. Soc.* **1966**, *88* (20), 4578–4583.

(44) Chang, J.; Hercules, D. M.; Roe, D. K. The Role of the Triplet State in the Electrochemiluminescence of Rubrene. *Electrochim. Acta* **1968**, *13* (5), 1197–1207.

(45) Yeh, L.-S. R.; Bard, A. J. Electrogenerated Chemiluminescence. Direct Heterogeneous Formation of the Triplet State by Reduction of Rubrene Radical Cation at an n-Type Zinc Oxide Electrode. *Chem. Phys. Lett.* **1976**, *44* (2), 339–343.

(46) Ma, L.; Galstyan, G.; Zhang, K.; Kloc, C.; Sun, H.; Soci, C.; Michel-Beyerle, M. E.; Gurzadyan, G. G. Two-Photon-Induced Singlet Fission in Rubrene Single Crystal. *J. Chem. Phys.* **2013**, *138* (18), 3–9.

(47) Irkhin, P.; Biaggio, I. Two-Photon Absorption Spectroscopy of Rubrene Single Crystals. *Phys. Rev. B - Condens. Matter Mater. Phys.* **2014**, *89* (20), 1–5.

(48) Mastrogiovanni, D. D. T.; Mayer, J.; Wan, A. S.; Vishnyakov, A.; Neimark, A. V; Podzorov, V.; Feldman, L. C.; Garfunkel, E. Oxygen Incorporation in Rubrene Single

Crystals. *Sci. Rep.* **2014**, *4* (1), 4753.

(49) Cudazzo, P.; Gatti, M.; Rubio, A. Excitons in Molecular Crystals from First-Principles Many-Body Perturbation Theory: Picene versus Pentacene. *Phys. Rev. B* **2012**, *86* (19), 195307.

(50) Davydov, A. S. *Theory of Molecular Excitons*; McGraw-Hill: New York, 1962.

(51) Agranovich, V. *Excitations in Organic Solids*; Oxford University Press: Oxford, 2008.

(52) Ryasnyanskiy, A.; Biaggio, I. Triplet Exciton Dynamics in Rubrene Single Crystals. *Phys. Rev. B* **2011**, *84* (19), 193203.

Bibliography

Agranovich, V. *Excitations in Organic Solids*; Oxford University Press: Oxford, 2008.

Akkerman, Q. A.; Rainò, G.; Kovalenko, M. V; Manna, L. Genesis, Challenges and Opportunities for Colloidal Lead Halide Perovskite Nanocrystals. *Nat. Mater.* **2018**, *17*, 394.

Alguire, E. C.; Subotnik, J. E.; Damrauer, N. H. Exploring Non-Condon Effects in a Covalent Tetracene Dimer: How Important Are Vibrations in Determining the Electronic Coupling for Singlet Fission? *J. Phys. Chem. A* **2015**, *119* (2), 299–311.

Amat, A.; Mosconi, E.; Ronca, E.; Quarti, C.; Umari, P.; Nazeeruddin, M. K.; Grätzel, M.; De Angelis, F. Cation-Induced Band-Gap Tuning in Organohalide Perovskites: Interplay of Spin–Orbit Coupling and Octahedra Tilting. *Nano Lett.* **2014**, *14*, 3608.

Angel, R. J.; Zhao, J.; Ross, N. L. General Rules for Predicting Phase Transitions in Perovskites Due to Octahedral Tilting. *Phys. Rev. Lett.* **2005**, *95*, 25503.

Aoyagi, S.; Kuroiwa, Y.; Sawada, A.; Kawaji, H.; Atake, T. Size Effect on Crystal Structure and Chemical Bonding Nature in BaTiO3 Nanopowder. *J. Therm. Anal. Calorim.* **2005**, *81*, 627.

Arias, D. H.; Ryerson, J. L.; Cook, J. D.; Damrauer, N. H.; Johnson, J. C. Polymorphism Influences Singlet Fission Rates in Tetracene Thin Films. *Chem. Sci.* **2016**, *7* (2), 1185–1191.

Ashner, M. N.; Shulenberger, K. E.; Krieg, F.; Powers, E. R.; Kovalenko, M. V; Bawendi, M. G.; Tisdale, W. A. Size-Dependent Biexciton Spectrum in CsPbBr3 Perovskite Nanocrystals. *ACS Energy Lett.* **2019**, *4*, 2639.

Baranov, D.; Lynch, M. J.; Curtis, A. C.; Carollo, A. R.; Douglass, C. R.; Mateo-Tejada, A. M.; Jonas, D. M. Purification of Oleylamine for Materials Synthesis and Spectroscopic Diagnostics for Trans Isomers. *Chem. Mater.* **2019**, *31* (4), 1223–1230.

Bartel, C. J.; Sutton, C.; Goldsmith, B. R.; Ouyang, R.; Musgrave, C. B.; Ghiringhelli, L. M.; Scheffler, M. New Tolerance Factor to Predict the Stability of Perovskite Oxides and Halides. *Sci. Adv.* **2019**, *5* (2), eaav0693.

Bawendi, M. G.; Steigerwald, M. L.; Brus, L. E. The Quantum Mechanics of Larger Semiconductor Clusters (“Quantum Dots”). *Annu. Rev. Phys. Chem.* **1990**, *41* (1), 477–496.

Beard, M. C.; Blackburn, J. L.; Johnson, J. C.; Rumbles, G. Status and Prognosis of Future-Generation Photoconversion to Photovoltaics and Solar Fuels. *ACS Energy Lett.* **2016**, *1* (2), 344–347.

Beimborn, J. C.; Hall, L. M. G.; Tongying, P.; Dukovic, G.; Weber, J. M. Pressure Response of Photoluminescence in Cesium Lead Iodide Perovskite Nanocrystals. *J. Phys. Chem. C* **2018**, *122* (20), 11024–11030.

Beimborn, J. C.; Walther, L. R.; Wilson, K. D.; Weber, J. M. Size-Dependent Pressure-Response of the Photoluminescence of CsPbBr3 Nanocrystals. *J. Phys. Chem. Lett.* **2020**, *11* (5), 1975–1980.

Beimborn, J. C.; Zagorec-Marks, W.; Weber, J. M. Spectroscopy of Resonant Intermediate States for Triplet–Triplet Annihilation Upconversion in Crystalline Rubrene: Radical Ions as Sensitizers. *J. Phys. Chem. Lett.* **2020**, *11* (17), 7212–7217.

Bekenstein, Y.; Koscher, B. A.; Eaton, S. W.; Yang, P.; Alivisatos, A. P. Highly Luminescent Colloidal Nanoplates of Perovskite Cesium Lead Halide and Their Oriented Assemblies. *J. Am. Chem. Soc.* **2015**, *137*, 16008.

Bender, J. A.; Raulerson, E. K.; Li, X.; Goldzak, T.; Xia, P.; Van Voorhis, T.; Tang, M. L.; Roberts, S. T. Surface States Mediate Triplet Energy Transfer in Nanocrystal–Acene Composite Systems. *J. Am. Chem. Soc.* **2018**, *140* (24), 7543–7553.

Bertolotti, F.; Protesescu, L.; Kovalenko, M. V; Yakunin, S.; Cervellino, A.; Billinge, S. J. L.; Terban, M. W.; Pedersen, J. S.; Masciocchi, N.; Guagliardi, A. Coherent Nanotwins and Dynamic Disorder in Cesium Lead Halide Perovskite Nanocrystals. *ACS Nano* **2017**, *11*, 3819.

Borriello, I.; Cantele, G.; Ninno, D. Ab Initio Investigation of Hybrid Organic-Inorganic Perovskites Based on Tin Halides. *Ab initio Investig. Hybrid Org. Perovskites Based Tin* **2008**, *77*, 235214.

Brennan, M. C.; Herr, J. E.; Nguyen-Beck, T. S.; Zinna, J.; Draguta, S.; Rouvimov, S.; Parkhill, J.; Kuno, M. Origin of the Size-Dependent Stokes Shift in CsPbBr3 Perovskite Nanocrystals. *J. Am. Chem. Soc.* **2017**, *139*, 12201.

Brennan, M. C.; Kuno, M.; Rouvimov, S. Crystal Structure of Individual CsPbBr3 Perovskite Nanocubes. *Inorg. Chem.* **2019**, *58*, 1555.

Brus, L. E. Electron–Electron and Electron-Hole Interactions in Small Semiconductor Crystallites: The Size Dependence of the Lowest Excited Electronic State. *J. Chem. Phys.* **1984**, *80*, 4403.

Butkus, J.; Vashishtha, P.; Chen, K.; Gallaher, J. K.; Prasad, S. K. K.; Metin, D. Z.; Laufersky, G.; Gaston, N.; Halpert, J. E.; Hodgkiss, J. M. The Evolution of Quantum Confinement in CsPbBr3 Perovskite Nanocrystals. *Chem. Mater.* **2017**, *29*, 3644.

Cao, Y.; Qi, G.; Liu, C.; Wang, L.; Ma, Z.; Wang, K.; Du, F.; Xiao, G.; Zou, B. Pressure-Tailored Band Gap Engineering and Structure Evolution of Cubic Cesium Lead Iodide Perovskite Nanocrystals. *J. Phys. Chem. C* **2018**, *122*, 9332.

Capitani, F.; Marini, C.; Caramazza, S.; Postorino, P.; Garbarino, G.; Hanfland, M.; Pisanu, A.; Quadrelli, P.; Malavasi, L. High-Pressure Behavior of Methylammonium Lead Iodide (MAPbI3) Hybrid Perovskite. *J. Appl. Phys.* **2016**, *119*, 185901.

Chang, J.; Hercules, D. M.; Roe, D. K. The Role of the Triplet State in the Electrochemiluminescence of Rubrene. *Electrochim. Acta* **1968**, *13* (5), 1197–1207.

Chen, C.-C.; Herhold, A. B.; Johnson, C. S.; Alivisatos, A. P. Size Dependence of Structural Metastability in Semiconductor Nanocrystals. *Science (80-.).* **1997**, *276*, 398.

Chen, K.; Jin, W.; Zhang, Y.; Yang, T.; Reiss, P.; Zhong, Q.; Bach, U.; Li, Q.; Wang, Y.; Zhang, H.; Bao, Q.; Liu, Y. High Efficiency Mesoscopic Solar Cells Using CsPbI3 Perovskite Quantum Dots Enabled by Chemical Interface Engineering. *J. Am. Chem. Soc.* **2020**, *142* (8), 3775–3783.

Chen, S.; Weitemier, A. Z.; Zeng, X.; He, L.; Wang, X.; Tao, Y.; Huang, A. J. Y.; Hashimotodani, Y.; Kano, M.; Iwasaki, H.; Parajuli, L. K.; Okabe, S.; Teh, D. B. L.; All, A. H.; Tsutsui-Kimura, I.; Tanaka, K. F.; Liu, X.; McHugh, T. J. Near-Infrared Deep Brain Stimulation via Upconversion Nanoparticle–Mediated Optogenetics. *Science (80-.).* **2018**, *359* (6376), 679–684.

Chen, Y.; Lee, B.; Fu, D.; Podzorov, V. The Origin of a 650 Nm Photoluminescence Band in Rubrene. *Adv. Mater.* **2011**, *23* (45), 5370–5375.

Chen, Z.; Sun, C. Q.; Zhou, Y.; Ouyang, G. Size Dependence of the Pressure-Induced Phase Transition in Nanocrystals. *J. Phys. Chem. C* **2008**, *112*, 2423.

Chen, Z.; Hu, Y.; Wang, J.; Shen, Q.; Zhang, Y.; Ding, C.; Bai, Y.; Jiang, G.; Li, Z.; Gaponik, N. Boosting Photocatalytic CO2 Reduction on CsPbBr3 Perovskite Nanocrystals by Immobilizing Metal Complexes. *Chem. Mater.* **2020**, *32* (4), 1517–1525.

Cheng, Y. Y.; Fückel, B.; Khoury, T.; Clady, R. G. C. R.; Tayebjee, M. J. Y.; Ekins-Daukes, N. J.; Crossley, M. J.; Schmidt, T. W. Kinetic Analysis of Photochemical Upconversion by Triplet-Triplet Annihilation: Beyond Any Spin Statistical Limit. *J. Phys. Chem. Lett.* **2010**, *1* (12), 1795–1799.

Choi, H. H.; Cho, K.; Frisbie, C. D.; Sirringhaus, H.; Podzorov, V. Critical Assessment of Charge Mobility Extraction in FETs. *Nat. Mater.* **2018**, *17* (1), 2–7.

Cottingham, P.; Brutchey, R. L. On The Crystal Structure of Colloidally Prepared CsPbBr3 Quantum Dots. *Chem. Commun.* **2016**, *52*, 5246.

Cruz, C. D.; Choi, H. H.; Podzorov, V.; Chronister, E. L.; Bardeen, C. J. Photon Upconversion in Crystalline Rubrene: Resonant Enhancement by an Interband State. *J. Phys. Chem. C* **2018**, *122* (31), 17632–17642.

Cudazzo, P.; Gatti, M.; Rubio, A. Excitons in Molecular Crystals from First-Principles Many-Body Perturbation Theory: Picene versus Pentacene. *Phys. Rev. B* **2012**, *86* (19), 195307.

Damrauer, N. H.; Snyder, J. L. Symmetry-Directed Control of Electronic Coupling for Singlet Fission in Covalent Bis–Acene Dimers. *J. Phys. Chem. Lett.* **2015**, *6* (22), 4456–4462.

Davydov, A. S. *Theory of Molecular Excitons*; McGraw-Hill: New York, 1962.

Di Stasio, F.; Christodoulou, S.; Huo, N.; Konstantatos, G. Near-Unity Photoluminescence Quantum Yield in CsPbBr3 Nanocrystal Solid-State Films via Postsynthesis Treatment with Lead Bromide. *Chem. Mater.* **2017**, *29* (18), 7663–7667.

Dillon, R. J.; Piland, G. B.; Bardeen, C. J. Different Rates of Singlet Fission in Monoclinic versus Orthorhombic Crystal Forms of Diphenylhexatriene. *J. Am. Chem. Soc.* **2013**, *135* (46), 17278–17281.

Dong, Y.; Qiao, T.; Kim, D.; Parobek, D.; Rossi, D.; Son, D. H. Precise Control of Quantum Confinement in Cesium Lead Halide Perovskite Quantum Dots via Thermodynamic Equilibrium. *Nano Lett.* **2018**, *18*, 3716.

Dutta, A.; Dutta, S. K.; Das Adhikari, S.; Pradhan, N. Tuning the Size of CsPbBr3 Nanocrystals: All at One Constant Temperature. *ACS Energy Lett.* **2018**, *3*, 329.

Efros, A. L.; Rosen, M. The Electronic Structure of Semiconductor Nanocrystals. *Annu. Rev. Mater. Sci.* **2000**, *30* (1), 475–521.

Ellingson, R. J.; Beard, M. C.; Johnson, J. C.; Yu, P.; Micic, O. I.; Nozik, A. J.; Shabaev, A.; Efros, A. L. Highly Efficient Multiple Exciton Generation in Colloidal PbSe and PbS Quantum Dots. *Nano Lett.* **2005**, *5* (5), 865–871.

Fröhlich, D.; Heidrich, K.; Künzel, H.; Trendel, G.; Treusch, J. Cesium-Trihalogen-Plumbates a New Class of Ionic Semiconductors. *J. Lumin.* **1979**, *18*, 385.

Fu, M.; Tamarat, P.; Huang, H.; Even, J.; Rogach, A. L.; Lounis, B. Neutral and Charged Exciton Fine Structure in Single Lead Halide Perovskite Nanocrystals Revealed by Magneto-Optical Spectroscopy. *Nano Lett.* **2017**, *17*, 2895.

Fu, Y.; Zhu, H.; Chen, J.; Hautzinger, M. P.; Zhu, X. Y.; Jin, S. Metal Halide Perovskite Nanostructures for Optoelectronic Applications and the Study of Physical Properties. *Nat. Rev. Mater.* **2019**, *4*, 169.

Garcia-Fernandez, P.; Aramburu, J. A.; Barriuso, M. T.; Moreno, M. Key Role of Covalent Bonding in Octahedral Tilting in Perovskites. *J. Phys. Chem. Lett.* **2010**, *1*, 647.

Gertsen, A. S.; Koerstz, M.; Mikkelsen, K. V. Benchmarking Triplet-Triplet Annihilation Photon Upconversion Schemes. *Phys. Chem. Chem. Phys.* **2018**, *20* (17), 12182–12192.

Gesi, K.; Ozawa, K.; Hirotsu, S. Effect of Hydrostatic Pressure on the Structural Phase Transitions in CsPbCl3 and CsPbBr3. *J. Phys. Soc. Jpn.* **1975**, *38*, 463.

Geva, N.; Nienhaus, L.; Wu, M.; Bulović, V.; Baldo, M. A.; Van Voorhis, T.; Bawendi, M. G. A Heterogeneous Kinetics Model for Triplet Exciton Transfer in Solid-State Upconversion. *J. Phys. Chem. Lett.* **2019**, *10* (11), 3147–3152.

Ghosh, D.; Aziz, A.; Dawson, J. A.; Walker, A. B.; Islam, M. S. Putting the Squeeze on Lead Iodide Perovskites: Pressure-Induced Effects To Tune Their Structural and Optoelectronic Behavior. *Chem. Mater.* **2019**, *31*, 4063.

Goldschmidt, V. M. Die Gesetze Der Krystallochemie. *Naturwissenschaften* **1926**, *14* (21), 477–485.

Goldstein, A. N.; Echer, C. M.; Alivisatos, A. P. Melting in Semiconductor Nanocrystals. *Science (80-.).* **1992**, *256*, 1425.

Gray, V.; Dzebo, D.; Abrahamsson, M.; Albinsson, B.; Moth-Poulsen, K. Triplet-Triplet Annihilation Photon-Upconversion: Towards Solar Energy Applications. *Phys. Chem. Chem. Phys.* **2014**, *16* (22), 10345–10352.

Gray, V.; Moth-Poulsen, K.; Albinsson, B.; Abrahamsson, M. Towards Efficient Solid-State Triplet–Triplet Annihilation Based Photon Upconversion: Supramolecular, Macromolecular and Self-Assembled Systems. *Coord. Chem. Rev.* **2018**, *362*, 54–71.

Grumstrup, E. M.; Johnson, J. C.; Damrauer, N. H. Enhanced Triplet Formation in Polycrystalline Tetracene Films by Femtosecond Optical-Pulse Shaping. *Phys. Rev. Lett.* **2010**, *105* (25), 257403.

Grünwald, M.; Lutker, K.; Alivisatos, A. P.; Rabani, E.; Geissler, P. L. Metastability in Pressure-Induced Structural Transformations of CdSe/ZnS Core/Shell Nanocrystals. *Nano Lett.* **2013**, *13*, 1367.

Gui, P.; Chen, Z.; Li, B.; Yao, F.; Zheng, X.; Lin, Q.; Fang, G. High-Performance Photodetectors Based on Single All-Inorganic CsPbBr3 Perovskite Microwire. *ACS Photonics* **2018**, *5* (6), 2113–2119.

Hercules, D. M.; Lansbury, R. C.; Roe, D. K. Chemiluminescence from the Reduction of Rubrene Radical Cations. *J. Am. Chem. Soc.* **1966**, *88* (20), 4578–4583.

Herhold, A. B.; Tolbert, S. H.; Guzelian, A. A.; Alivisatos, A. P.; Pelizzetti, E. *Fine Particles Science and Technology: From Micro to Nanoparticles*; 1996.

Hirotsu, S.; Harada, J.; Iizumi, M.; Gesi, K. Structural Phase Transitions in CsPbBr3. *J. Phys. Soc. Jpn.* **1974**, *37*, 1393.

Holzapfel, W. B. Refinement of the Ruby Luminescence Pressure Scale. *J. Appl. Phys.* **2003**, *93*, 1813.

Huang, H.; Polavarapu, L.; Sichert, J. A.; Susha, A. S.; Urban, A. S.; Rogach, A. L. Colloidal Lead Halide Perovskite Nanocrystals: Synthesis, Optical Properties and Applications. *NPG Asia Mater.* **2016**, *8*, 1.

Irkhin, P.; Biaggio, I. Two-Photon Absorption Spectroscopy of Rubrene Single Crystals. *Phys. Rev. B - Condens. Matter Mater. Phys.* **2014**, *89* (20), 1–5.

Irkhin, P.; Biaggio, I. Direct Imaging of Anisotropic Exciton Diffusion and Triplet Diffusion Length in Rubrene Single Crystals. *Phys. Rev. Lett.* **2011**, *107* (1), 1–4.

Islangulov, R. R.; Kozlov, D. V.; Castellano, F. N. Low Power Upconversion Using MLCT Sensitizers. *Chem. Commun.* **2005**, *1* (30), 3776–3778.

Jaffe, A.; Lin, Y.; Beavers, C. M.; Voss, J.; Mao, W. L.; Karunadasa, H. I. High-Pressure Single-Crystal Structures of 3D Lead-Halide Hybrid Perovskites and Pressure Effects on Their Electronic and Optical Properties. *ACS Cent. Sci.* **2016**, *2*, 201.

Jena, A. K.; Kulkarni, A.; Miyasaka, T. Halide Perovskite Photovoltaics: Background, Status, and Future Prospects. *Chem. Rev.* **2019**, *119*, 3036.

Jurchescu, O. D.; Meetsma, A.; Palstra, T. T. M. Low-Temperature Structure of Rubrene Single Crystals Grown by Vapor Transport. *Acta Crystallogr. Sect. B* **2006**, *62* (2), 330–334.

Kincaid, J. M.; Stell, G.; Goldmark, E. Isostructural Phase Transitions Due to Core Collapse. II. A Three-Dimensional Model with a Solid–Solid Critical Point. *J. Chem. Phys.* **1976**, *65*, 2172.

Kirschner, M. S.; Diroll, B. T.; Guo, P.; Harvey, S. M.; Helweh, W.; Flanders, N. C.; Brumberg, A.; Watkins, N. E.; Leonard, A. A.; Evans, A. M.; Wasielewski, M. R.; Dichtel, W. R.; Zhang, X.; Chen, L. X.; Schaller, R. D. Photoinduced, Reversible Phase Transitions in All-Inorganic Perovskite Nanocrystals. *Nat. Commun.* **2019**, *10* (1), 504.

Kiseleva, N.; Nazari, P.; Dee, C.; Busko, D.; Richards, B. S.; Seitz, M.; Howard, I. A.; Turshatov, A. Lanthanide Sensitizers for Large Anti-Stokes Shift Near-Infrared-to-Visible Triplet–Triplet Annihilation Photon Upconversion. *J. Phys. Chem. Lett.* **2020**, *11* (7), 2477–2481.

Kondo, S.; Masaki, A.; Saito, T.; Asada, H. Fundamental Optical Absorption of CsPbI3 and Cs4PbI6. *Solid State Commun.* **2002**, *124*, 211.

Kong, Z.-C.; Liao, J.-F.; Dong, Y.-J.; Xu, Y.-F.; Chen, H.-Y.; Kuang, D.-B.; Su, C.-Y. Core@Shell CsPbBr3@Zeolitic Imidazolate Framework Nanocomposite for Efficient Photocatalytic CO2 Reduction. *ACS Energy Lett.* **2018**, *3* (11), 2656–2662.

Koscher, B. A.; Swabeck, J. K.; Bronstein, N. D.; Alivisatos, A. P. Essentially Trap-Free CsPbBr3 Colloidal Nanocrystals by Postsynthetic Thiocyanate Surface Treatment. *J. Am. Chem. Soc.* **2017**, *139*, 6566.

Lai, M.; Kong, Q.; Bischak, C. G.; Yu, Y.; Dou, L.; Eaton, S. W.; Ginsberg, N. S.; Yang, P. Structural, Optical, and Electrical Properties of Phase-Controlled Cesium Lead Iodide Nanowires. *Nano Res.* **2017**, *10*, 1107.

Lee, J.-H.; Bristowe, N. C.; Lee, J. H.; Lee, S.-H.; Bristowe, P. D.; Cheetham, A. K.; Jang, H. M. Resolving the Physical Origin of Octahedral Tilting in Halide Perovskites. *Chem. Mater.* **2016**, *28*, 4259.

Li, M.; Liu, T.; Wang, Y.; Yang, W.; Lü, X. Pressure Responses of Halide Perovskites With Various Compositions, Dimensionalities, and Morphologies. *Matter Radiat. Extrem.* **2020**, *5*, 18201.

Li, Q.; Li, S.; Wang, K.; Quan, Z.; Meng, Y.; Zou, B. High-Pressure Study of Perovskite-Like Organometal Halide: Band-Gap Narrowing and Structural Evolution of [NH3-(CH2)4-NH3]CuCl4. *J. Phys. Chem. Lett.* **2017**, *8*, 500.

Liu, H.; Yan, F.; Li, W.; Lee, C. S.; Chu, B.; Chen, Y.; Li, X.; Han, L.; Su, Z.; Zhu, J.; Kong, X.; Zhang, L.; Luo, Y. Up-Conversion Luminescence of Crystalline Rubrene without Any Sensitizers. *Org. Electron.* **2010**, *11* (5), 946–950.

Liu, L.; Zhao, R.; Xiao, C.; Zhang, F.; Pevere, F.; Shi, K.; Huang, H.; Zhong, H.; Sychugov, I. Size-Dependent Phase Transition in Perovskite Nanocrystals. *J. Phys. Chem. Lett.* **2019**, *10*, 5451.

Ly, J. T.; Lopez, S. A.; Lin, J. B.; Kim, J. J.; Lee, H.; Burnett, E. K.; Zhang, L.; Aspuru-Guzik, A.; Houk, K. N.; Briseno, A. L. Oxidation of Rubrene, and Implications for Device Stability. *J. Mater. Chem. C* **2018**, *6* (14), 3757–3761.

Ma, L.; Galstyan, G.; Zhang, K.; Kloc, C.; Sun, H.; Soci, C.; Michel-Beyerle, M. E.; Gurzadyan, G. G. Two-Photon-Induced Singlet Fission in Rubrene Single Crystal. *J. Chem. Phys.* **2013**, *138* (18), 3–9.

Ma, L.; Zhang, K.; Kloc, C.; Sun, H.; Michel-Beyerle, M. E.; Gurzadyan, G. G. Singlet Fission in Rubrene Single Crystal: Direct Observation by Femtosecond Pump–Probe Spectroscopy. *Phys. Chem. Chem. Phys.* **2012**, *14* (23), 8307–8312.

Ma, L.; Zhang, K.; Kloc, C.; Sun, H.; Soci, C.; Michel-Beyerle, M. E.; Gurzadyan, G. G. Fluorescence from Rubrene Single Crystals: Interplay of Singlet Fission and Energy Trapping. *Phys. Rev. B* **2013**, *87* (20), 201203.

Manifacier, J. C.; Gasiot, J.; Fillard, J. P. A Simple Method for the Determination of the Optical Constants n, k and the Thickness of a Weakly Absorbing Thin Film. *J. Phys. E.* **1976**, *9* (11), 1002–1004.

Manser, J. S.; Christians, J. A.; Kamat, P. V. Intriguing Optoelectronic Properties of Metal Halide Perovskites. *Chem. Rev.* **2016**, *116*, 12956.

Mastrogiovanni, D. D. T.; Mayer, J.; Wan, A. S.; Vishnyakov, A.; Neimark, A. V; Podzorov, V.; Feldman, L. C.; Garfunkel, E. Oxygen Incorporation in Rubrene Single Crystals. *Sci. Rep.* **2014**, *4* (1), 4753.

Matsuishi, K.; Ishihara, T.; Onari, S.; Chang, Y. H.; Park, C. H. Optical Properties and Structural Phase Transitions of Lead-Halide Based Inorganic–Organic 3D and 2D Perovskite Semiconductors Under High Pressure. *Phys. Status Solidi B* **2004**, *241*, 3328.

Meulenberg, R. W.; Strouse, G. F. Pressure-Induced Electronic Coupling in CdSe Semiconductor Quantum Dots. *Phys. Rev. B* **2002**, *66* (3), 35317.

Milstein, T. J.; Kroupa, D. M.; Gamelin, D. R. Picosecond Quantum Cutting Generates Photoluminescence Quantum Yields Over 100% in Ytterbium-Doped CsPbCl3 Nanocrystals. *Nano Lett.* **2018**, *18*, 3792.

Mitrofanov, O.; Kloc, C.; Siegrist, T.; Lang, D. V.; So, W. Y.; Ramirez, A. P. Role of Synthesis for Oxygen Defect Incorporation in Crystalline Rubrene. *Appl. Phys. Lett.* **2007**, *91* (21).

Miyata, K.; Kurashige, Y.; Watanabe, K.; Sugimoto, T.; Takahashi, S.; Tanaka, S.; Takeya, J.; Yanai, T.; Matsumoto, Y. Coherent Singlet Fission Activated by Symmetry Breaking. *Nat. Chem.* **2017**, *9* (10), 983–989.

MØLLER, C. H. R. K. N. Crystal Structure and Photoconductivity of Cæsium Plumbohalides. *Nature* **1958**, *182* (4647), 1436.

Nagaoka, Y.; Hills-Kimball, K.; Tan, R.; Li, R.; Wang, Z.; Chen, O. Nanocube Superlattices of Cesium Lead Bromide Perovskites and Pressure-Induced Phase Transformations at Atomic and Mesoscale Levels. *Adv. Mater.* **2017**, *29*, 1606666.

Nattestad, A.; Cheng, Y. Y.; MacQueen, R. W.; Schulze, T. F.; Thompson, F. W.; Mozer, A. J.; Fückel, B.; Khoury, T.; Crossley, M. J.; Lips, K.; Wallace, G. G.; Schmidt, T. W. Dye-Sensitized Solar Cell with Integrated Triplet–Triplet Annihilation Upconversion System. *J. Phys. Chem. Lett.* **2013**, *4* (12), 2073–2078.

Nenon, D. P.; Pressler, K.; Kang, J.; Koscher, B. A.; Olshansky, J. H.; Osowiecki, W. T.; Koc, M. A.; Wang, L.-W.; Alivisatos, A. P. Design Principles for Trap-Free CsPbX3 Nanocrystals: Enumerating and Eliminating Surface Halide Vacancies with Softer Lewis Bases. *J. Am. Chem. Soc.* **2018**, *140*, 17760.

Nienhaus, L.; Wu, M.; Geva, N.; Shepherd, J. J.; Wilson, M. W. B.; Bulović, V.; Van Voorhis, T.; Baldo, M. A.; Bawendi, M. G. Speed Limit for Triplet-Exciton Transfer in Solid-State PbS Nanocrystal-Sensitized Photon Upconversion. *ACS Nano* **2017**, *11* (8), 7848–7857.

Nirmal, M.; Brus, L. Luminescence Photophysics in Semiconductor Nanocrystals. *Acc. Chem. Res.* **1999**, *32* (5), 407–414.

Norris, D. J.; Bawendi, M. G. Measurement and Assignment of the Size-Dependent Optical Spectrum in CdSe Quantum Dots. *Phys. Rev. B Condens. Matter Mater. Phys.* **1996**, *53*, 16338.

Nozik, A. J. Multiple Exciton Generation in Semiconductor Quantum Dots. *Chem. Phys. Lett.* **2008**, *457* (1), 3–11.

Oehzelt, M.; Aichholzer, A.; Resel, R.; Heimel, G.; Venuti, E.; Della Valle, R. G. Crystal Structure of Oligoacenes Under High Pressure. *Phys. Rev. B Condens. Matter Mater. Phys.* **2006**, *74*, 104103.

Oksenberg, E.; Sanders, E.; Popovitz-Biro, R.; Houben, L.; Joselevich, E. Surface-Guided CsPbBr3 Perovskite Nanowires on Flat and Faceted Sapphire with Size-Dependent Photoluminescence and Fast Photoconductive Response. *Nano Lett.* **2018**, *18* (1), 424–433.

Otto, J. W.; Vassiliou, J. K.; Frommeyer, G. Nonhydrostatic Compression of Elastically Anisotropic Polycrystals. I. Hydrostatic Limits of 4:1 Methanol-Ethanol and Paraffin Oil. *Compression Elastically Anisotropic Polycrystals. I. Hydrostatic Limits 41 Methanol-Ethanol Paraffin Oil* **1998**, *57*, 3253.

Pan, A.; Ma, X.; Huang, S.; Wu, Y.; Jia, M.; Shi, Y.; Liu, Y.; Wangyang, P.; He, L.; Liu, Y. CsPbBr3 Perovskite Nanocrystal Grown on MXene Nanosheets for Enhanced Photoelectric Detection and Photocatalytic CO2 Reduction. *J. Phys. Chem. Lett.* **2019**, *10* (21), 6590–6597.

Pandey, A. K. Highly Efficient Spin-Conversion Effect Leading to Energy up-Converted Electroluminescence in Singlet Fission Photovoltaics. *Sci. Rep.* **2015**, *5*, 1–6.

Parker, C. A.; Bowen, E. J. Sensitized P-Type Delayed Fluorescence. *Proc. R. Soc. London. Ser. A. Math. Phys. Sci.* **1963**, *276* (1364), 125–135.

Prasanna, R.; Gold-Parker, A.; Leijtens, T.; Conings, B.; Babayigit, A.; Boyen, H.-G.; Toney, M. F.; McGehee, M. D. Band Gap Tuning via Lattice Contraction and Octahedral Tilting in Perovskite Materials for Photovoltaics. *J. Am. Chem. Soc.* **2017**, *139*, 11117.

Protesescu, L.; Yakunin, S.; Bodnarchuk, M. I.; Krieg, F.; Caputo, R.; Hendon, C. H.; Yang, R. X.; Walsh, A.; Kovalenko, M. V. Nanocrystals of Cesium Lead Halide Perovskites (CsPbX3, X = Cl, Br, and I): Novel Optoelectronic Materials Showing Bright Emission with Wide Color Gamut. *Nano Lett.* **2015**, *15*, 3692.

Puppin, M.; Polishchuk, S.; Colonna, N.; Crepaldi, A.; Dirin, D. N.; Nazarenko, O.; De Gennaro, R.; Gatti, G.; Roth, S.; Barillot, T.; Poletto, L.; Xian, R. P.; Rettig, L.; Wolf, M.; Ernstorfer, R.; Kovalenko, M. V.; Marzari, N.; Grioni, M.; Chergui, M. Evidence of Large Polarons in Photoemission Band Mapping of the Perovskite Semiconductor CsPbBr3. *Phys. Rev. Lett.* **2020**, *124* (20), 206402.

Pushkarev, A. P.; Korolev, V. I.; Markina, D. I.; Komissarenko, F. E.; Naujokaitis, A.; Drabavičius, A.; Pakštas, V.; Franckevičius, M.; Khubezhov, S. A.; Sannikov, D. A.; Zasedatelev, A. V; Lagoudakis, P. G.; Zakhidov, A. A.; Makarov, S. V. A Few-Minute Synthesis of CsPbBr3 Nanolasers with a High Quality Factor by Spraying at Ambient Conditions. *ACS Appl. Mater. Interfaces* **2019**, *11* (1), 1040–1048.

Ramade, J.; Andriambariarijaona, L. M.; Steinmetz, V.; Goubet, N.; Legrand, L.; Barisien, T.; Bernardot, F.; Testelin, C.; Lhuillier, E.; Bramati, A. Fine Structure of Excitons and Electron–Hole Exchange Energy in Polymorphic CsPbBr3 Single Nanocrystals. *Nanoscale* **2018**, *10*, 6393.

Ravetz, B. D.; Pun, A. B.; Churchill, E. M.; Congreve, D. N.; Rovis, T.; Campos, L. M. Photoredox Catalysis Using Infrared Light via Triplet Fusion Upconversion. *Nature* **2019**, *565* (7739), 343–346.

Rodová, M.; Brožek, J.; Knížek, K.; Nitsch, K. Phase Transitions in Ternary Caesium Lead Bromide. *J. Therm. Anal. Calorim.* **2003**, *71*, 667.

Rossetti, R.; Ellison, J. L.; Gibson, J. M.; Brus, L. E. Size Effects in the Excited Electronic States of Small Colloidal CdS Crystallites. *J. Chem. Phys.* **1984**, *80*, 4464.

Ryasnyanskiy, A.; Biaggio, I. Triplet Exciton Dynamics in Rubrene Single Crystals. *Phys. Rev. B* **2011**, *84* (19), 193203.

Saeki, A.; Seki, S.; Takenobu, T.; Iwasa, Y.; Tagawa, S. Mobility and Dynamics of Charge Carriers in Rubrene Single Crystals Studied by Flash-Photolysis Microwave Conductivity and Optical Spectroscopy. *Adv. Mater.* **2008**, *20* (5), 920–923.

Scheidt, R. A.; Atwell, C.; Kamat, P. V. Tracking Transformative Transitions: From CsPbBr3 Nanocrystals to Bulk Perovskite Films. *ACS Mater. Lett.* **2019**, *1*, 8.

Schmidt, T. W.; Castellano, F. N. Photochemical Upconversion: The Primacy of Kinetics. *J. Phys. Chem. Lett.* **2014**, *5* (22), 4062–4072.

Schulze, T. F.; Schmidt, T. W. Photochemical Upconversion: Present Status and Prospects for Its Application to Solar Energy Conversion. *Energy Environ. Sci.* **2015**, *8* (1), 103–125.

Shamsi, J.; Urban, A. S.; Imran, M.; De Trizio, L.; Manna, L. Metal Halide Perovskite Nanocrystals: Synthesis, Post-Synthesis Modifications, and Their Optical Properties. *Chem. Rev.* **2019**, *119*, 3296.

Shi, H.; Du, M.-H. Shallow Halogen Vacancies in Halide Optoelectronic Materials. *Phys. Rev. B* **2014**, *90* (17), 174103.

Singh-Rachford, T. N.; Castellano, F. N. Photon Upconversion Based on Sensitized Triplet-Triplet Annihilation. *Coord. Chem. Rev.* **2010**, *254* (21–22), 2560–2573.

Smith, M. B.; Michl, J. Singlet Fission. *Chem. Rev.* **2010**, *110* (11), 6891–6936.

Steigerwald, M. L.; Brus, L. E. Semiconductor Crystallites: A Class of Large Molecules. *Acc. Chem. Res.* **1990**, *23*, 183.

Stoumpos, C. C.; Kanatzidis, M. G. The Renaissance of Halide Perovskites and Their Evolution as Emerging Semiconductors. *Acc. Chem. Res.* **2015**, *48*, 2791.

Stoumpos, C. C.; Malliakas, C. D.; Peters, J. A.; Liu, Z.; Sebastian, M.; Im, J.; Chasapis, T. C.; Wibowo, A. C.; Chung, D. Y.; Freeman, A. J. Crystal Growth of the Perovskite Semiconductor CsPbBr3: A New Material for High-Energy Radiation Detection. *Cryst. Growth Des.* **2013**, *13*, 2722.

Strauch, D. *Semiconductors*; 1991.

Straus, D. B.; Guo, S.; Cava, R. J. Kinetically Stable Single Crystals of Perovskite-Phase CsPbI3. *J. Am. Chem. Soc.* **2019**, *141* (29), 11435–11439.

Sugimoto, S.; Fukunishi, Y.; Fukaya, Y.; Yamao, T.; Hotta, S. Refractive Index Dispersion and Anisotropic Group Refractive Indices of Rubrene Crystals. *Trans. Mater. Res. Soc. Japan* **2013**, *38* (2), 301–304.

Sutherland, B. R.; Sargent, E. H. Perovskite Photonic Sources. *Nat. Photonics* **2016**, *10*, 295.

Swarnkar, A.; Chulliyil, R.; Ravi, V. K.; Irfanullah, M.; Chowdhury, A.; Nag, A. Colloidal CsPbBr3 Perovskite Nanocrystals: Luminescence beyond Traditional Quantum Dots. *Angew. Chem., Int. Ed.* **2015**, *127*, 15644.

Swarnkar, A.; Marshall, A. R.; Sanehira, E. M.; Chernomordik, B. D.; Moore, D. T.; Christians, J. A.; Chakrabarti, T.; Luther, J. M. Quantum Dot-Induced Phase Stabilization of α-CsPbI3 Perovskite for High-Efficiency Photovoltaics. *Science (80-.).* **2016**, *354*, 92.

Szafrański, M.; Katrusiak, A. Photovoltaic Hybrid Perovskites Under Pressure. *J. Phys. Chem. Lett.* **2017**, *8*, 2496.

Talapin, D. V; Rogach, A. L.; Kornowski, A.; Haase, M.; Weller, H. Highly Luminescent Monodisperse CdSe and CdSe/ZnS Nanocrystals Synthesized in a Hexadecylamine−Trioctylphosphine Oxide−Trioctylphospine Mixture. *Nano Lett.* **2001**, *1* (4), 207–211.

Tayebjee, M. J. Y.; McCamey, D. R.; Schmidt, T. W. Beyond Shockley–Queisser: Molecular Approaches to High-Efficiency Photovoltaics. *J. Phys. Chem. Lett.* **2015**, *6* (12), 2367–2378.

Tekmen, M.; Müller, J. D. High-Pressure Cell for Fluorescence Fluctuation Spectroscopy. *Rev. Sci. Instrum.* **2004**, *75*, 5143.

Tolbert, S. H.; Alivisatos, A. P. The Wurtzite to Rock Salt Structural Transformation in CdSe Nanocrystals Under High Pressure. *J. Chem. Phys.* **1995**, *102*, 4642.

Tolbert, S. H.; Alivisatos, A. P. High-Pressure Structural Transformations in Semiconductor Nanocrystals. *Annu. Rev. Phys. Chem.* **1995**, *46*, 595.

Tolbert, S. H.; Alivisatos, A. P. Size Dependence of the Solid-Solid Phase Transition in CdSe Nanocrystals. *Z. Phys. D At., Mol. Clust.* **1993**, *26*, 56.

Tolbert, S. H.; Herhold, A. B.; Brus, L. E.; Alivisatos, A. P. Pressure-Induced Structural Transformations in Si Nanocrystals: Surface and Shape Effects. *Phys. Rev. Lett.* **1996**, *76*, 4384.

Tong, Y.; Bladt, E.; Aygüler, M. F.; Manzi, A.; Milowska, K. Z.; Hintermayr, V. A.; Docampo, P.; Bals, S.; Urban, A. S.; Polavarapu, L. Highly Luminescent Cesium Lead Halide Perovskite Nanocrystals with Tunable Composition and Thickness by Ultrasonication. *Angew. Chem., Int. Ed.* **2016**, *55*, 13887.

Udayabhaskararao, T.; Houben, L.; Cohen, H.; Menahem, M.; Pinkas, I.; Avram, L.; Wolf, T.; Teitelboim, A.; Leskes, M.; Yaffe, O. A Mechanistic Study of Phase Transformation in Perovskite Nanocrystals Driven by Ligand Passivation. *Chem. Mater.* **2017**, *30*, 84.

Wang, C.; Chesman, A. S. R.; Jasieniak, J. J. Stabilizing the Cubic Perovskite Phase of CsPbI3 Nanocrystals by Using an Alkyl Phosphinic Acid. *Chem. Commun.* **2016**, *53*, 232.

Wang, L.; Wang, K.; Xiao, G.; Zeng, Q.; Zou, B. Pressure-Induced Structural Evolution and Band Gap Shifts of Organometal Halide Perovskite-Based Methylammonium Lead Chloride. *J. Phys. Chem. Lett.* **2016**, *7*, 5273.

Wang, P.; Guan, J.; Galeschuk, D. T. K.; Yao, Y.; He, C. F.; Jiang, S.; Zhang, S.; Liu, Y.; Jin, M.; Jin, C. Pressure-Induced Polymorphic, Optical, and Electronic Transitions of Formamidinium Lead Iodide Perovskite. *J. Phys. Chem. Lett.* **2017**, *8*, 2119.

Wang, Y.; Herron, N. Nanometer-Sized Semiconductor Clusters: Materials Synthesis, Quantum Size Effects, and Photophysical Properties. *J. Phys. Chem.* **1991**, *95*, 525.

Wieghold, S.; Bieber, A. S.; VanOrman, Z. A.; Daley, L.; Leger, M.; Correa-Baena, J. P.; Nienhaus, L. Triplet Sensitization by Lead Halide Perovskite Thin Films for Efficient Solid-State Photon Upconversion at Subsolar Fluxes. *Matter* **2019**, *1* (3), 705–719.

Wieghold, S.; Bieber, A. S.; Vanorman, Z. A.; Nienhaus, L. Influence of Triplet Diffusion on Lead Halide Perovskite-Sensitized Solid-State Upconversion. *J. Phys. Chem. Lett.* **2019**, *10* (13), 3806–3811.

Wieghold, S.; Nienhaus, L. Precharging Photon Upconversion: Interfacial Interactions in Solution-Processed Perovskite Upconversion Devices. *J. Phys. Chem. Lett.* **2020**, *11* (3), 601–607.

Wu, X.; Tan, L. Z.; Shen, X.; Hu, T.; Miyata, K.; Trinh, M. T.; Li, R.; Coffee, R.; Liu, S.; Egger, D. A.; Makasyuk, I.; Zheng, Q.; Fry, A.; Robinson, J. S.; Smith, M. D.; Guzelturk, B.; Karunadasa, H. I.; Wang, X.; Zhu, X.; Kronik, L.; Rappe, A. M.; Lindenberg, A. M. Light-Induced Picosecond Rotational Disordering of the Inorganic Sublattice in Hybrid Perovskites. *Sci. Adv.* **2017**, *3* (7), e1602388.

Xia, P.; Raulerson, E. K.; Coleman, D.; Gerke, C. S.; Mangolini, L.; Tang, M. L.; Roberts, S. T. Achieving Spin-Triplet Exciton Transfer between Silicon and Molecular Acceptors for Photon Upconversion. *Nat. Chem.* **2020**, *12* (2), 137–144.

Xiao, G.; Cao, Y.; Qi, G.; Wang, L.; Liu, C.; Ma, Z.; Yang, X.; Sui, Y.; Zheng, W.; Zou, B. Pressure Effects on Structure and Optical Properties in Cesium Lead Bromide Perovskite Nanocrystals. *J. Am. Chem. Soc.* **2017**, *139*, 10087.

Xiao, J.; Yang, Y.; Xu, X.; Shi, J.; Zhu, L.; Lv, S.; Wu, H.; Luo, Y.; Li, D.; Meng, Q. Pressure-Assisted CH3NH3PbI3 Morphology Reconstruction to Improve the High Performance of Perovskite Solar Cells. *J. Mater. Chem. A* **2015**, *3*, 5289.

Xu, Y.-F.; Yang, M.-Z.; Chen, B.-X.; Wang, X.-D.; Chen, H.-Y.; Kuang, D.-B.; Su, C.-Y. A CsPbBr3 Perovskite Quantum Dot/Graphene Oxide Composite for Photocatalytic CO2 Reduction. *J. Am. Chem. Soc.* **2017**, *139* (16), 5660–5663.

Yaffe, O.; Guo, Y.; Tan, L. Z.; Egger, D. A.; Hull, T.; Stoumpos, C. C.; Zheng, F.; Heinz, T. F.; Kronik, L.; Kanatzidis, M. G. Local Polar Fluctuations in Lead Halide Perovskite Crystals. *Phys. Rev. Lett.* **2017**, *118*, 136001.

Yeh, L.-S. R.; Bard, A. J. Electrogenerated Chemiluminescence. Direct Heterogeneous Formation of the Triplet State by Reduction of Rubrene Radical Cation at an n-Type Zinc Oxide Electrode. *Chem. Phys. Lett.* **1976**, *44* (2), 339–343.

Yin, T.; Fang, Y.; Chong, W. K.; Ming, K. T.; Jiang, S.; Li, X.; Kuo, J.-L.; Fang, J.; Sum, T. C.; White, T. J. High-Pressure-Induced Comminution and Recrystallization of CH3NH3PbBr3 Nanocrystals as Large Thin Nanoplates. *Adv. Mater.* **2018**, *30*, 1705017.

Yoo, D.; Woo, J. Y.; Kim, Y.; Kim, S. W.; Wei, S.-H.; Jeong, S.; Kim, Y.-H. Origin of the Stability and Transition from Anionic to Cationic Surface Ligand Passivation of All-Inorganic Cesium Lead Halide Perovskite Nanocrystals. *J. Phys. Chem. Lett.* **2020**, *11*, 652.

Yuan, G.; Qin, S.; Wu, X.; Ding, H.; Lu, A. Pressure-Induced Phase Transformation of CsPbI3 by X-Ray Diffraction and Raman Spectroscopy. *Phase Transitions* **2018**, *91*, 38.

Zeng, X.; Zhang, D.; Duan, L.; Wang, L.; Dong, G.; Qiu, Y. Morphology and Fluorescence Spectra of Rubrene Single Crystals Grown by Physical Vapor Transport. *Appl. Surf. Sci.* **2007**, *253* (14), 6047–6051.

Zhang, L.; Zeng, Q.; Wang, K. Pressure-Induced Structural and Optical Properties of Inorganic Halide Perovskite CsPbBr3. *J. Phys. Chem. Lett.* **2017**, *8*, 3752.

Zhao, Q.; Hazarika, A.; Schelhas, L. T.; Liu, J.; Gaulding, E. A.; Li, G.; Zhang, M.; Toney, M. F.; Sercel, P. C.; Luther, J. M. Size-Dependent Lattice Structure and Confinement Properties in CsPbI3 Perovskite Nanocrystals: Negative Surface Energy for Stabilization. *ACS Energy Lett.* **2020**, *5*, 238.

Appendix

Kinetic Model MATLAB Code:

```
%% RubreneKinetics
%  This script simulates the model for rubrene upconversion using radical
%  ions as sensitizers. Values for constants are below, change them in the
%  code under "Declaration of constants" section if need be.
%  Author: JCB
%  Date: 2020-07-20

%% Declaration of constants

%Time step (s)

dt = 1E-13; %0.1 ns time step

ttot = 2E-4; % total time for simulation in seconds

n = round(ttot/dt); % number of steps

t = zeros(n,1); % time array

% Populations

Neo = zeros(n,1); % trapped electons
Neo(1) = 1E19; % initial value of trapped electrons

Nho = zeros(n,1); % trapped holes
Nho(1) =  1E19;

Ne = zeros(n,1); % mobile electrons

Nh = zeros(n,1); % mobile holes

Nt = zeros(n,1); %triplet excitons

Ns = zeros(n,1); %singlet excitons

Npl = zeros(n,1); % total number of photons that have been emitted

%Excitation

Istart = input("Enter starting fluence: "); %photon fluence in photons/(cm^2*s)

num_iter = input("Enter number of data points: ");

P = zeros(num_iter,2); % Array for storing fluence and PL

xcte = 1E-16; % electron CT exciton formation cross section

xcth = 1E-16; % hole CT exciton formation cross sections
```

```
%Rate constants

kR = 1E-12; % CT exciton recombinatino rate constant

kL = 300000; % mobile hole or electron loss rate constant

kA = 1E-12; % TTA rate constant

ksf = 5E10; % singlet fission rate constant

kq = 1.67E4; % triplet quenching rate constant

kttq = 1E-14; %triplet-triplet quenching rate constant

kpl = 6.25E7; %PL rate constant

%% Kinetics
for j = 1:num_iter
    I = Istart*10^(j-1);
    P(j,1) = I;
    i = 2; % start at i=2 so that i-1 gives first row of vectors
    while i < n+1
        t(i) = t(i-1) + dt; % calculate the time at this step.

        % to simulate a 5ns pulse, use laser fluence above until the time is
        % greater than 5 ns and then set I = 0.
        if t(i) > 5E-9
            I = 0;
        end

        % Excitation (CT exciton formation)
        Neo(i) = Neo(i-1)+(-I*Neo(i-1)*xcte + kL*Neo(n-1))*dt;

        Nho(i) = Nho(i-1)+(-I*Nho(i-1)*xcte + kL*Nho(n-1))*dt;

        Ne(i) = Ne(i-1)+(I*Neo(i-1)*xcte - kR*Ne(i-1)*Nh(i-1) - kL*Ne(i-1))*dt;

        Nh(i) = Nh(i-1)+(I*Nho(i-1)*xcth - kR*Ne(i-1)*Nh(i-1) - kL*Nh(i-1))*dt;

        %Triplet population
        Nt(i) = Nt(i-1)+(kR*Ne(i-1)*Nh(i-1) - kA*Nt(i-1)^2 + 2*ksf*Ns(i-1) -
kq*Nt(i-1))*dt;

        %Singlet population
        Ns(i) = Ns(i-1)+(kA*Nt(i-1)^2-kpl*Ns(i-1) - ksf*Ns(i-1))*dt;

        %Photoluminescence
        Npl(i) = Npl(i-1)+(kpl*Ns(i-1))*dt;

        i = i+1;
    end
    P(j,2) = Npl(n);
end
scatter(P(:,1),P(:,2));
```